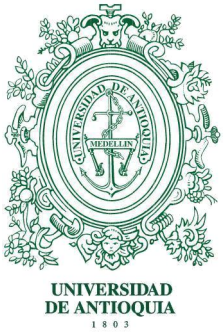

UNIVERSIDAD DE ANTIOQUIA
FACULTAD DE CIENCIAS EXACTAS Y NATURALES
INSTITUTO DE FÍSICA

THE LATE INTEGRATED SACHS-WOLFE EFFECT IN COSMOLOGICAL SIMULATIONS

David Ricardo Valencia Díaz
Facultad de Ciencias Exactas y Naturales
Instituto de Física

Advisor: Juan Carlos Muñoz Cuartas

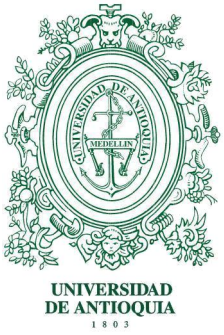

UNIVERSIDAD DE ANTIOQUIA
FACULTAD DE CIENCIAS EXACTAS Y NATURALES
INSTITUTO DE FÍSICA

THE LATE INTEGRATED SACHS-WOLFE EFFECT IN COSMOLOGICAL SIMULATIONS

David Ricardo Valencia Díaz
Facultad de Ciencias Exactas y Naturales
Instituto de Física
Advisor: Juan Carlos Muñoz Cuartas

Student Advisor

Medellín, 2014

To my family, my girlfriend, my friends and the science, to which I wish to make my little contribution

The late Integrated Sachs-Wolfe effect in cosmological simulations

Author: David Ricardo Valencia Díaz

Advisor: Juan Carlos Muñoz Cuartas

Printed in Medellín, Colombia

First edition, August 2014

Abstract

Nowadays, the accepted cosmological model is the so called Λ-Cold Dark Matter (ΛCDM), which has been proposed as a model that fits the observations while allows to explain them based on the basis of the therory of General Relativiy. In such model, the Universe is considered to be homogeneous, isotropic and to be composed by diverse components as the baryonic matter, dark matter, radiation and dark energy. The most abundant components are the dark matter and the dark energy, from which the dark energy is the current dominant component.

The Cosmic Microwave Background (CMB) is a microwave radiation field that permeates the Universe. In principle, this radiation should be homogeneous, but due to several physical processes, the CMB photons underwent perturbations that induced the formation of several anisotropies. The study of the CMB anisotropies may lead to evidence of the existence of the dark energy, which is associated with the current accelerated expansion of the Universe. In that context, one of those CMB anisotropies is the Integrated Sachs-Wolfe (ISW) effect. The ISW is an effect that the CMB photons experience when they pass through non-stationary overdense or underdense regions, changing their wavelength and energies. Such perturbation in the CMB is associated to the evolution in time of the gravitational potential wells of dark matter structures that form the Large Scale Structures (LSS) and host the galaxies.

The aim of this work is to study the late ISW effect in a cosmological simulation, in order to obtain the maps of the anisotropies due to a late ISW effect and study the relation of this temperature fluctuations with the evolution of the gravitational potential wells and the matter density they contain. This is a preliminar study of the ISW effect only in cosmological N-body simulations. The results of this work will allow us to perform a more detailed and

extensive study of this effect with both, cosmological simulations and data of galaxy redshift surveys in a future step of the project. What is expected, after a comparison between those exhaustive studies with synthetic and real data, is to detect the signal associated with Integrated Sachs-Wolfe effect, and with that, give a possible evidence of the presence of the dark energy.

The numerical and computational methods used to study the late Integrated Sachs-Wolfe effect in this work are based in the Fourier transform of different fields, as the density field, the gravitational potential field and its corresponding time derivative, and the interpolation and numerical integration of the time derivative of the gravitational potential $\dot{\Phi}(\mathbf{x})$. The results obtained in this work correspond to the late ISW effect in a simulation box of $400h^{-1}$Mpc. The methods used to calculate the different fields mentioned before and the maps obtained after the data processing are shown, as well as the maps of the late ISW anisotropy in the simulation box. An interpretation of the results is given and supported with an analysis of the structures of the simulation. Finally, the results are tested through three methods: comparison with linear regime, estimation of the temperature fluctuations along the integration axis and numerical convergence. From those test, it is possible to conclude that the ISW maps obtained with the exact solution and with the linear approximantion show a very good coherence and the linear approximation shows a good behavior in its regime. The numerical convergence test shows that independently of the number of integration steps and of the resolution used, our results present a good convergence. When we compare the temperature fluctuations along the integration axis, our results also shows a good correspondence and behavior with both, the linear approximation values and the different integration steps. Even, when comparing the behavior of the temperature fluctuations along the integration axis with the results obtained in the works of other authors, we obtain similar results. All those tests show a very good processing of the data and that our results are coherent.

Acknowledgments

After a long time trying to discover and learn the methods of the science and knowing that it is only the beginning of this path, I want to thank to my parents, Carmen Díaz Osorio and José Valencia Gallego, because by their effort and support I could finish this stage of my life and started to walk this path. Also, many thanks to my sister Clara Isabel Valencia Díaz and to my girlfriend María Alejandra Urrego Cañas, by their loving support and patience and the little but valuable contributions which they help me to finish this work. It is mainly to them, my family, to whom I dedicate this work.

I also desire to thank to all my teachers who throughout my career share their knowledge and advices that allow me to arrive at this point. All of them leave something valuable for me to understand how this path must be walked, and how it mustn't. Especially, I wish to highlight the work of my advisor, Juan Carlos Muños Cuartas, who allow me to work with him, giving me the idea to work on this particular topic and sharing with me all his experience and knowledge to succeed in this project. Many thanks to him by his patience, kindness and support and by the motivation he gave me. I wish to thank to my peers Sebastian Bustamante by his help in some topics about programming and his advices and to César León Uribe, because although in few meetings, he helps us to understand something more about the effect studied in this work. I also wish to thanks to the teacher Jordi-Lluís Figueras at the Uppsala University, by his help, time and kind answers to my questions about the use of the FFTW library.

Finally, many thanks to my peers and friends at the Physics Institute by their support along all this work and all this career, for sharing with me your experiences all this time.

Sincerely,

David Ricardo Valencia Díaz

August, 2014

Contents

List of Figures

"So that when I look up at the night sky and I know that yes, we are part of this Universe, we are in this Universe, but perhaps more important than both of those facts is that the Universe is in us. When I reflect on that fact [...] I feel big, because my atoms came from those stars."

Neil deGrasse Tyson

CHAPTER

1

Theoretical Framework

Cosmology is the study of the origin and evolution of the Universe. It allows us to understand how is the dynamics of the Universe and the ways it would evolve in the different realizations we can create theoretically, given some parameters and assumptions. But according to the observations, the most accepted model is the ΛCDM model, in which the Universe is an expanding entity, which is homogeneous and isotropic and have a flat geometry. In this model, the Universe is composed by baryonic matter, which is the ordinary matter that composes planets, stars and even live; the radiation, which is the main component used in astronomy and astrophysics to study and understand the Universe; the dark matter and the dark energy. Those last components are almost completely unknown for us, but we can explain its role in the evolution of the Universe.

Dark matter only interacts with baryonic matter by the gravitational force; as it doesn't interact in a electromagnetic way, we can not observe it, but some observations as the rotation curves of galaxies tells us that it should be some massive component that allows the galaxies and galaxy clusters to exist and maintain its form.

Dark energy is the most unknown component of all, but observationally, we can infer that the cosmological constant, which is related to this dark energy, dominates the Universe and produces a negative pressure, balancing the gravitational push of matter and allowing the Universe to expand at an accelerated rate.

In this first chapter, we are going to study the background of cosmology and some complex problems as the formation of structures and the study of the Cosmic Microwave

Background (CMB). Both problems allow us to understand the origin and evolution of the Universe.

1.1 Cosmological Context

1.1.1 Cosmological Principle and Hubble's Law

The cosmological principle states that the Universe is isotropic and homogeneous. The homogeneity means a translational symmetry, or that the Universe has an uniform composition, while the isotropy is related to a rotational symmetry, it has the same properties in all directions.

This principle also states that the Universe is in an accelerated expansion, which is governed by the Hubble's law. This law allow us to find the recessional velocity of an object in the sky respect to the Earth. Taking the Earth at the origin, according to the Hubble's law, the recessional velocities respect to the Earth of two galaxies A and B with positions $\mathbf{r}_A$ and $\mathbf{r}_B$, respectively, will be:

$$\mathbf{v_A} = H_0\mathbf{r_A} \tag{1.1}$$

$$\mathbf{v_B} = H_0\mathbf{r_B} \tag{1.2}$$

Where H_0 is known as the Hubble's constant, $\mathbf{v_A}$ and $\mathbf{v_B}$ are the velocities of the galaxies A and B, respectively. The recessional velocity of galaxy B as seen by an observer in galaxy A is:

$$\mathbf{v_A} - \mathbf{v_B} = H_0\mathbf{r_A} - H_0\mathbf{r_B} = H_0(\mathbf{r_A} - \mathbf{r_B}) \tag{1.3}$$

The observer in A sees all of the other galaxies in the Universe moving away with recessional velocities described by the same Hubble's law as on Earth. Actually, H_0 is a function of time, $H = H(t)$, which at the present time t_0 has the value $H(t_0) = H_0$ [5].

1.1.2 Robertson-Walker Metric

Now, assuming that Einstein's general relativity holds in this isotropic, homogeneous Universe, the dynamics of the space-time is described by the Einstein's field equations [2]:

$$R_{\mu\nu} - \frac{1}{2}g_{\mu\nu} + \Lambda g_{\mu\nu} = \kappa T_{\mu\nu} \tag{1.4}$$

Where:

- $R_{\mu\nu}$ is the Riemann curvature tensor and R is its respective curvature scalar.
- $g_{\mu\nu}$ is the metric of the homogeneous and isotropic Universe.
- $T_{\mu\nu}$ is the stress-energy-momentum tensor.
- κ is the Einstein's gravitational constant: $\kappa = 8\pi G/c^4$.

In an homogeneous and isotropic Universe, although the curvature of space may change with time, the curvature has the same value everywhere at a given time since the Big-Bang [5]. A metric that can describe this kind of Universe is the Robertson-Walker (RW) metric, given by:

$$\begin{aligned}(\mathrm{d}s)^2 &= g_{\mu\nu}\mathrm{d}x^\mu \mathrm{d}x^\nu \\ &= -c^2(\mathrm{d}t)^2 + a^2(t)\left\{\frac{(\mathrm{d}x)^2}{1-kx^2} + x^2\left[(\mathrm{d}\theta)^2 + \sin^2(\theta)(\mathrm{d}\phi)^2\right]\right\}\end{aligned} \tag{1.5}$$

This metric determines the space-time interval between 2 events in the isotropic, homogeneous Universe. Here:

- x is the comoving coordinate that does not change with the scale of the Universe and are coordinates respect to a frame that moves with the expansion of the Universe.
- $a(t)$ is the scale factor of the Universe that characterizes the relative size of the Universe.
- k is the space-time curvature.

At the present time t_0, the value of the scale factor can be chosen to be $a(t_0) = 1$. The time t is a universal time that measures the time that has elapsed since the Big-Bang. It is not an absolute time, but merely reflects a choice of how clocks of distant observers are to be synchronized [5].

For an expanding Universe, the value of the scale factor can tell us if we are looking at the future $(a > 1)$ or the at past $(a < 1)$. As the comoving coordinates do not change with

the Universe scale, it appears a physical coordinate r which is the observed coordinate, and is related to the comoving coordinate x by means of [2]:

$$r = a(t)x \tag{1.6}$$

Physical coordinates r change with the expansion of the Universe, characterized by the scale factor $a(t)$. The expansion of the Universe can be seen with an example as in Figure 1.1. From this figure, the Universe can be seen as an expanding balloon, while the galaxies in the Universe are drawn in the surface of the balloon. The position of each galaxy is the same when the Universe expands, but each galaxy separates from the others with an accelerated rate. Seeing in comoving coordinates, it does not matter the expansion, because the distance between each galaxy is the same.

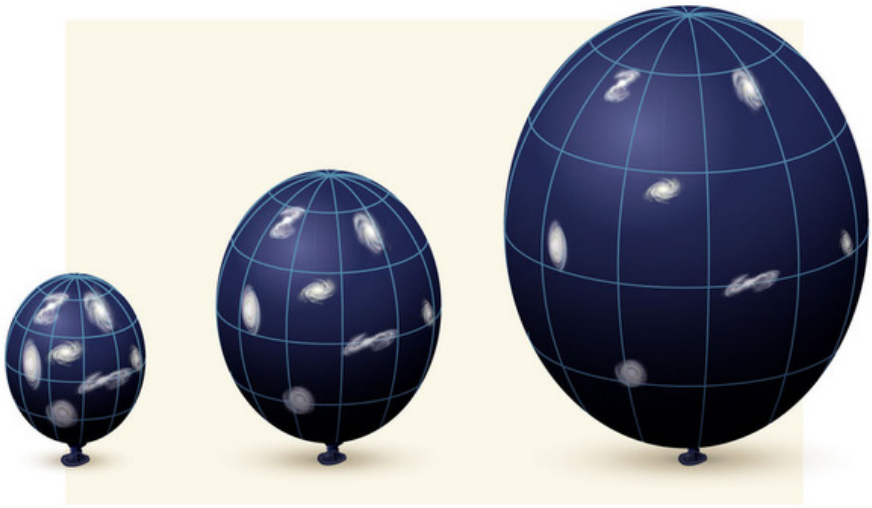

Figure 1.1: Sketch of the expansion of the Universe. This expansion can be seen as the galaxies are drawn in the surface of an expanding balloon. The position of the galaxies will be the same, independent of the Universe's expansion, but the distance between them will be larger as the Universe expands. Taken from `http://scienceblogs.com/startswithabang/`.

We can also take into account the behavior of the scale factor $a(t)$ according to the curvature k. In the RW metric Equation 1.5, the curvature of the Universe allows to model the Universe as an open Universe ($k < 0$) a flat Universe ($k = 0$) and a close Universe ($k > 0$). An open Universe will expand forever, while a close

Universe will have a collapse at the end of its evolution. The scale factor charaterizes the expansion of the Universe, we can see this behavior in Figure 1.2. actually, observations show us an opposite effect than the shown in Figure 1.2, the Universe is expanding at an accelerated rate, but it is because the dynamics of the Universe is given by the interaction of the components inside it, and not by its geometry, as we will see later.

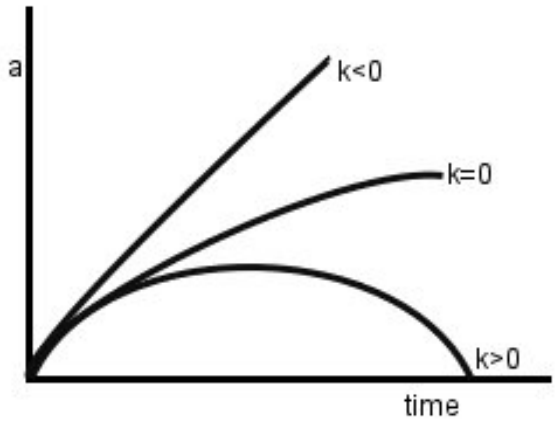

Figure 1.2: Evolution of the scale factor as a function of time for universes with different curvatures. This figure shows the evolution of the scale factor for different geometries: An open Universe ($k < 0$) will expand forever, while a close Universe will begin to expand, an after some time will collapse. In the case of a flat Universe ($k = 0$), the Universe will expand forever, but the expansion rate will decrease and the expansion will be slow. Taken from `http://physicsmadeeasy.wordpress.com/physics-made-easy/cosmology-ii/`.

1.1.3 Friedmann Equations

When solving the Einstein's field equations for an isotropic, homogeneous Universe, i.e., described by the RW metric, we obtain the Friedmann equations; those ordinary differential equations lead to a description of the dynamical evolution for a non-static Universe, characterized by the temporal change of the scale factor $a(t)$, as follows:

$$\left(\frac{\dot{a}}{a}\right)^2 = \frac{8\pi G\rho}{3} - \frac{kc^2}{a^2} + \frac{\Lambda c^2}{3} \tag{1.7}$$

$$\frac{\ddot{a}}{a} = -\frac{4\pi G}{3}\left(\rho + \frac{3P}{c^2} + \frac{\Lambda c^2}{3}\right) \tag{1.8}$$

The Equation 1.7 is obtained from the temporal (time-line or 00) component of the Einstein's field equations, meanwhile Equation 1.8 is obtained from Equation 1.7 together with the trace of the Einstein's field equations (Equation 1.4) (see, for example `http://en.wikipedia.org/wiki/Friedmann_equations`).

Here $\dot{a} = \mathrm{d}a/\mathrm{d}t$, and Λ is the cosmological constant. A non-zero cosmological constant implies that space would be curved even in an empty Universe that is devoid of matter. Also, the term ρc^2 is the total mass-energy density, which is the superposition of the density of matter and radiation: $\rho = \rho_m + \rho_r$. A general expression for the density can be obtained when supposing a mass M enclosed in a spherical volume V of radius r in physical coordinates; that means $V \propto r^3 \propto a^3 x^3$. Then, the density in this spherical volume is given by:

$$\rho = \frac{3M}{4\pi r^3} = \frac{3M}{4\pi x^3 a^3} \tag{1.9}$$

A relation between the density measured in physical coordinates ρ and the density measured in comoving coordinates ρ_{comoving} is given by:

$$\frac{\rho}{\rho_{\text{comoving}}} = \frac{\rho}{\rho_0} = a^{-3} \tag{1.10}$$

Which is a relation that holds even between the density in physical coordinates ρ and the density measured at the present time ρ_0 [5]. As a particular case, assuming that $\Lambda = 0$, and that the Universe is filled with matter but not with radiation, Equation 1.10 holds in this dust-filled Universe.

In comoving coordinates, density does not change because the volume of space that contents a unit of mass do not vary in time, while in physical coordinates density decreases because the mass inside a volume of space is the same, but the volume becomes larger with time [2].

1.2 Dynamical Models of the Universe

The different dynamical models of the Universe allow us to understand the behavior of the Universe given by the interaction of the different components of the Universe. We can study simple models of only one component (as "dust" models, non-relativistic and relativistic models) or more complex models with more than one component in which it

is more evident that the dynamical behavior of the Universe depends on the interaction between the densities of those components.

1.2.1 Fluid Equation

By the firts law of thermodynamics, supposing the Universe as a closed system and its total energy density is the sum of the energy densities of the whole components of the Universe, one can find a fluid equation that relates the change of the density in time (or with the scale factor) with the pressure and density of the Universe. As there is a 1-to-1 relation between time t and scale factor a, the fluid equation could be writen in the following ways:

$$a\frac{\mathrm{d}\rho}{\mathrm{d}a} + 3\left(\rho + \frac{P}{c^2}\right) = 0 \tag{1.11}$$

$$\frac{\mathrm{d}\rho}{\mathrm{d}t} + \frac{3\dot{a}}{a}\left(\rho + \frac{P}{c^2}\right) = 0 \tag{1.12}$$

In those equations, ρ is the total density of the Universe, P is the pressure due to the components and c is the speed of light. We can use these equations to describe particular models of the Universe, as in the next subsection.

1.2.2 Case 1. Non-Relativistic Fluid (Dust Model)

In this case, the velocity dispersion is too low and the pressure due to the movement of the particles can be neglected. It is the same to assume that the kinetic energy of the particles is lower than their rest energy: $P << \rho c^2$. In this model, only particles (no radiation) are taken into account. Assuming massive, non-charged particles and without pressure, the fluid equation becomes:

$$\frac{\mathrm{d}\rho}{\mathrm{d}a} + \frac{3\rho}{a} = 0 \tag{1.13}$$

With:

$$\rho = \frac{\mathcal{E}}{c^2} = \frac{nmc^2}{c^2}; \;\; n \equiv \text{Particle number density} \tag{1.14}$$

From Equation 1.13 and Equation 1.14 one can obtain the following equation:

$$n = n_0 a^{-3} \;\Rightarrow\; \rho = \rho_0 a^{-3} \tag{1.15}$$

Which is the earlier Equation 1.10 that relates the matter density at any time with the present value of the density. Then, the equation of state for non-relativistic particles is $P = 0$.

1.2.3 Case 2. Non-relativistic "Hot" Fluid

Now, we consider an ideal gas with internal energy proportional to its temperature. Starting from the equation of state for an ideal gas and the equipartition of energy:

$$P = nk_B T \tag{1.16}$$

$$\mathcal{E}_{Total} = nmc^2 + \frac{3}{2} nk_B T \tag{1.17}$$

We obtain a relation between temperature and the scale factor, as follows:

$$T = T_0 a^{-2} \tag{1.18}$$

This equation tell us that as the volume increases, but the energy remains constant, then the energy density and the temperature decreases with time.

1.2.4 Case 3. Relativistic Fluid

With the help of the equation of state for a relativistic fluid and the fluid equation in terms of the total energy density:

$$P = \frac{1}{3}\mathcal{E}_{Total} \;\Rightarrow\; \frac{\mathrm{d}\mathcal{E}_{Total}}{\mathrm{d}a} + \frac{4\mathcal{E}_{Total}}{a} = 0 \tag{1.19}$$

The total energy density is proportional to: $\mathcal{E}_{Total} \propto a^{-4}$. Taking into account that the total energy density is the sum of the energy densities of all the particles in the Universe:

$$\mathcal{E}_{Total} = \sum_n nh\nu \propto a^{-4} \tag{1.20}$$

Using Equation 1.15, we find that $\nu = \nu_0 a^{-1}$. This relation means that the observed photon (with frequency ν_0) is not the same as the emitted one (with frequency ν). This photon will be shifted to a lower frequency. With this in mind, we can define the scale factor as a function of a new parameter called redshift z, that is related to this shift in the frequency of the photons:

$$z = \frac{\nu - \nu_0}{\nu_0} = \frac{\nu}{\nu_0} - 1 \;\Rightarrow\; z = a^{-1} - 1$$

$$a = \frac{1}{z+1} \tag{1.21}$$

As an example, if we see an object with redshift $z = 3$, this means that light we observe from this object right now was emitted when the Universe had $1/4$ of its present size.

The redshift is this change in the frequency of the photons, from a higher emitted frequency ν, to a lower observed frequency ν_0. This means that the photon will lose energy in its travel from the source to the observer. We can also talk about a blueshift, that means that the emitted frequency ν of the photon will be lower than the observed one ν_0, meaning that the photon gained energy in its journey. Both kind of shifts in the frequency are related to the Doppler effect, thus as we feel that the frequency of the siren of an ambulance increases if the ambulance is coming to us from far, and then, when the ambulance is going away from us its frequency decreases, we can talk about a Doppler effect in the frequency of the electromagnetic waves, which are the two kind of shifts we have talked before, redshift and blueshift.

The lost of energy measured when a photon undergoes a redshift is due to the expansion of the Universe, and can be detected when a photon originated in a far source which is moving away from the observer, by both reasons, the recessional velocity of the source and by the expansion of the Universe, the wavelength of this photons will become larger

(and the frequency will decrease) than the wavelenght of the photon when it was emitted by the source. As we have said before, the frequency of the emitted photon is higher than the frequency of the observed one.

If the photon undergoes a blueshift, this means that the source which emitted it is moving toward the observer, and by this forward velocity, the wavelenght of the photon will diminish (and its frequency will become higher) respect to the wavelenght of the emitted photon. Then, the frequency of the emitted photon is lower than the frequency of the observed one.

Figure 1.3 and Figure 1.4 show an sketch of what redshift and blueshift are, and how an spectrum of a moving source will be seen in both cases.

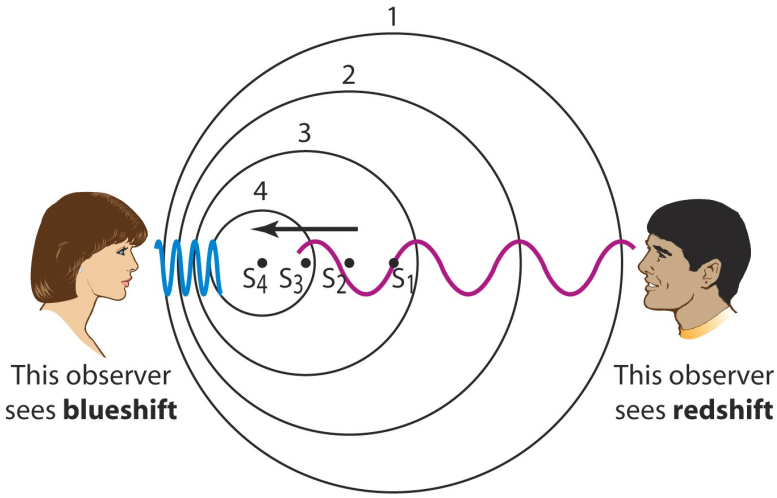

Figure 1.3: Redshift and blueshift seen by two different observers. If the source is moving away from the observer, this observer is going to see a redshifted photon, while the observer which sees the source going toward it will see a blueshifted photon. Taken from `http://alienspacesciencenews.wordpress.com/`

1.2.5 General Equation of State

All the equations of state we have seen in the last sections could be summarized in only one equation, as follows:

$$P = c^2 \omega_i \rho_i \tag{1.22}$$

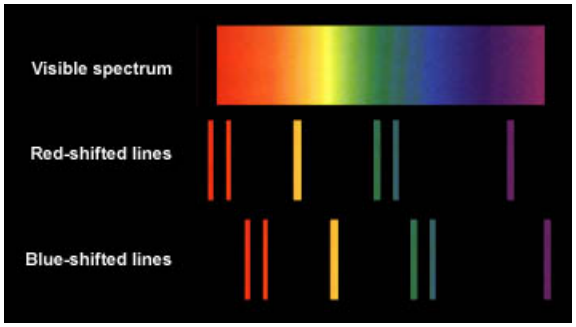

Figure 1.4: An example of a spectrum of an object undergoing redshift or blueshift. The lines of the spectrum will move to the red range of the electromagnetic spectrum if the photons are redshifted, on the contrary the lines will move to the blue range. Taken from `http://www.astrocappella.com/background/doppler_background.shtml`.

Where ω_i is a parameter associated with each one of the components of the Universe. Some values for different components of the Universe are:

- $\omega_i = \omega_m = 0$: Non-collisional dust.
- $\omega_i = \omega_r = 1/3$: Relativistic particles and radiation.
- $\omega_i = \omega_\Lambda = -1$: Vacuum energy associated with Dark Energy.
- Other values of ω_i are associated with different models of the Dark Energy.

The equation of state is the only way to modify the components in the Universe.

1.2.6 Case 4. Models with more than One Component

Remembering that Equation 1.15 describes the conservation of mass within an expanding shell, but for a pressureless dust Universe, if we desire to take into account more than one component of the Universe, we can generalize Equation 1.15 incorporating pressure-producing components. For a dust Universe, the density is given by Equation 1.14, while for relativistic particles such as neutrinos and photons, ρ is the equivalent mass density. Imagine a Universe filled with fluid (dust, photons, and so on) of uniform density ρ, pressure P and temperature T. Choosing an arbitrary point for the origin and with r the radius of a comoving spherical surface centered on the origin. With the first law of thermodynamics $\mathrm{d}U = \mathrm{d}Q - \mathrm{d}W$ applied to the fluid in the expanding shell and assuming that the entire Universe is at the same temperature, so there can be no heat flow and the

expansion of the Universe is adiabatic, then any change in the internal energy of the Universe must be produced by the work done by the fuild [5]:

$$\frac{\mathrm{d}U}{\mathrm{d}t} = -\frac{\mathrm{d}W}{\mathrm{d}t} = -P\frac{\mathrm{d}V}{\mathrm{d}t};\ \ V = \frac{4\pi r^3}{3} \tag{1.23}$$

Then:

$$\frac{\mathrm{d}U}{\mathrm{d}t} = -\frac{4\pi}{3}P\frac{\mathrm{d}r^3}{\mathrm{d}t} \tag{1.24}$$

Defining the internal energy per unit volume u as $u = 3U/(4\pi r^3)$ and writing u in terms of the equivalent mass density $u = \rho/c^2$, we obtain:

$$\frac{\mathrm{d}(r^3\rho)}{\mathrm{d}t} = -\frac{P}{c^2}\frac{\mathrm{d}r^3}{\mathrm{d}t} \tag{1.25}$$

But since the physical coordinates are related to the comoving ones by means of Equation 1.6, we find the fluid equation (Equation 1.12). To solve this differential equation, we use the general equation of state (Equation 1.22). After substitution of Equation 1.22 in Equation 1.12, we find a Bernoulli differential equation of the form:

$$\frac{\mathrm{d}(a^3\rho)}{\mathrm{d}t} = -\omega\rho\frac{\mathrm{d}a^3}{\mathrm{d}t} \tag{1.26}$$

With solution [5]:

$$a^{3(1+\omega)}\rho = \rho_0 = \text{constant} \tag{1.27}$$

Where ρ_0 is the present value of mass density, or equivalent mass density. For a pressureless dust $\omega_m = 0$ and we find Equation 1.15 again. Equation 1.27 shows us how with the expansion of the Universe, each one of the densities of the different components of the Universe change in a different way according to the parameter ω_i, which means that the behavior of each one of the components will be different along the expansion and evolution of the Universe.

1.3 Cosmological Parameters

Cosmological parameters allow to study the relations between the densities of the components of the Universe and its change with the evolution and expansion of the Universe, i. e., the dynamical evolution of the Universe related to the interaction of the different components inside it.

1. **Hubble's Constant:** In the Hubble's law, it is the constant that relates the recessional velocity of an object with its position:

$$v = rH \tag{1.28}$$

If r is the physical coordinate of the object ($r = ax$), then $v = \mathrm{d}r/\mathrm{d}t$, and we can obtain an expression for the Hubble's constant as a function of the scale factor from the Friedmann equations:

$$\frac{\dot{a}}{a} = H(t) \tag{1.29}$$

Equation 1.29 give us the rate of change in time of a per unit of the scale factor of the Universe. This last equations tells that, actually, H is not constant, but it is an important parameter to characterize the Universe expansion rate. Using the solutions to the Friedmann equation and changing from time t to redshit z, we can write:

$$H(z) = H_0 E(z) \tag{1.30}$$

$$H_0 = 100h \text{ km s}^{-1} \text{ Mpc}^{-1} \tag{1.31}$$

Where h is known as the *Hubble's parameter* and has an approximate value of $h \approx 0.70$. We will soon see an explicit expression for $E(z)$.

2. **Critical Density ρ_c:** The first Friedmann equation (Equation 1.7) can be rewritten in terms of the Hubble parameter as follows:

$$\left(\frac{\dot{a}}{a}\right)^2 = H^2(t) = \frac{8\pi G\rho}{3} - \frac{kc^2}{a^2} + \frac{\Lambda c^2}{3} \tag{1.32}$$

When assuming a Universe without cosmological constant $\Lambda = 0$, and that this Universe is flat $k = 0$, the density obtained with such conditions is called Universe's critical density, and it is the density that the Universe must have to be flat. The critical density has the following expression:

$$\rho_c(t) = \frac{3H^2(t)}{8\pi G} \tag{1.33}$$

Remembering Equation 1.30, the critical density can be rewritten as:

$$\rho_c(z) = \rho_{c,0}E^2(z) \tag{1.34}$$

$$\rho_{c,0} = \frac{3H_0^2}{8\pi G} \tag{1.35}$$

3. **Density Parameters Ω_i:** The density parameters are the ratios between the density of each component of the Universe and the critical density. The total density parameter is the sum of all the density parameters:

$$\Omega_{total} = \Omega_0 = \sum_i \Omega_i = \Omega_m + \Omega_r + \Omega_\Lambda + \Omega_k \tag{1.36}$$

Where Ω_i represents each of the components of the Universe, each one having the following expression:

$$\begin{aligned} \Omega_m &= \frac{\rho_m}{\rho_c} \\ \Omega_r &= \frac{\rho_r}{\rho_c} \\ \Omega_\Lambda &= \frac{\rho_v}{\rho_c} \\ \Omega_k &= \frac{\rho_k}{\rho_c} \end{aligned} \tag{1.37}$$

In a flat Universe, the curvature density parameter is $\Omega_k = 0$ and the total density parameter, both at any time as in the present, must be $\Omega_{total} = \Omega_0 = 1$.

From the Friedmann equations at present time and taking into account that we can transform from time t to scale factor a and to redshift z, we can find an expression for the function $E(z)$, related to the Hubble constant $H(z)$ in Equation 1.30, in terms of the redshift and the density parameters at present time (represented as $\Omega_{i,0}$):

$$E(z) = \sqrt{\Omega_{\Lambda,0} + (1 - \Omega_0)(1+z)^2 + \Omega_{m,0}(1+z)^3 + \Omega_{r,0}(1+z)^4} \tag{1.38}$$

With this outcome, we can rewrite the density parameters in terms of $E(z)$, as follows:

$$\begin{aligned} \Omega_m &= \frac{\Omega_{m,0}(1+z)^3}{E^2(z)} \\ \Omega_r &= \frac{\Omega_{r,0}(1+z)^4}{E^2(z)} \\ \Omega_\Lambda &= \frac{\Omega_{\Lambda,0}}{E^2(z)} \end{aligned} \tag{1.39}$$

4. **Cosmological Constant Λ:**

   The cosmological constant Λ was used by Einstein to obtain a static Universe from the Friedmann equation (Equation 1.32), in such a way that the gravitational collapse would be balanced by the repulsive force due to this constant. Nowadays, we assume that this constant is associated with the Dark Energy. The cosmological constant allow us to disconnect the geometry of the Universe (described by the curvature k) from its dynamics, which is governed by the interaction of the densities of the components in the Universe.

   The relation between the cosmological constant Λ and the vacuum density ρ_v is given by:

$$\Lambda = 8\pi G \rho_v \tag{1.40}$$

As the vacuum density ρ_v remains constant as the Universe expands, more Dark Energy must continually appear to fill the increasing volume [5].

Remembering the general equation of state (Equation 1.22) and with the respective value for $\omega_i = \omega_v = -1$, we obtain a relation between the cosmological constant and its respective density parameter:

$$\Omega_\Lambda = \frac{\Lambda}{3H^2(t)} = \frac{8\pi G\rho_v}{3H^2(t)} \tag{1.41}$$

1.3.1 Universe's Eras

As we have seen, in a cosmological model which takes into account different components, the dynamics of the Universe will be given by the interaction of all these components. Nowadays, the most accepted model is known as the ΛCDM model, which refers to a Universe dominated by the cosmological constant Λ, and then by the Dark Energy, and by the Cold Dark Matter (CDM). Dark Energy, as we have seen, is associated with the cosmological constant, and produces a negative pressure that expands the Universe. Observations show us that it is the major constituent of the Universe. The Cold Dark Matter is the second major constituent, and is an hypothetical kind of matter that we can not observe, because it does not interact electromagnetically. The only interaction of the Cold Dark Matter is the gravitational interaction with the ordinary (or baryonic) matter. The other components of the Universe in the ΛCDM model are the baryonic matter and the radiation. By baryonic matter we understand all matter made by baryons, all the ordinary matter that we can observe and forms the stars, planets and even life. Baryonic matter is only a little piece of the components of the Universe. Radiation refers to all relativistic particles, such as photons and neutrinos and comprehend the lesser part of the components. Observations from some probes and satellites allows to know the relative proportions of the components of the Universe, as in Figure 1.5.

Depending on the stage of the evolution of the Universe, some components dominates over the other components, which allows to define the dynamics of the Universe. We can study the different moments were one of the component dominates over the others, and call this moment an era.

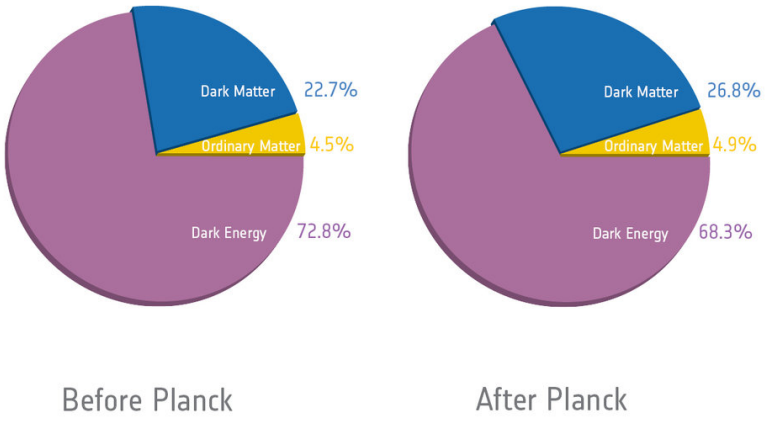

Figure 1.5: Observed proportions of the components of the Universe, in agreement with the assumptions of the ΛCDM cosmological model. Taken from `http://www.esa.int/For_Media/Photos/Highlights/Planck`.

Equation 1.27 shows that particles belonging to different categories are diluted differently by the expansion of the Universe; at earlier epochs when the Universe was much hotter, even massive particles were relativistic [5].

Radiation-dominated Era: As we have mentioned, in a Universe with more than one component the density of the different componentes is given by Equation 1.27. This equation means that along the evolution and expansion of the Universe, different components dominates over the other, because its density becomes larger in some stages of time, and it is when we can separate the stages of the Universe in different eras.

Radiation-dominated era refers this stage in the evolution of the Universe where the dynamics of the Universe were set by radiation, which refers generally to the constituents of the Universe which move relativistically, principally photons and neutrinos. This era last for maybe 50000 years.

The equilibrium redshift z_{eq} is defined as the redshift such that radiation and matter had the same density $\Omega_r = \Omega_m$. We can find an expression for the scale factor a when the radiation dominated ($z >> z_{\text{eq}}$) [2]:

$$a(t) = \left(\frac{32\pi\rho_{r,0}}{3}\right)^{\frac{1}{4}} t^{1/2} \tag{1.42}$$

Where z_{eq} is given by [18]:

$$1 + z_{\text{eq}} \simeq 2.3 \times 10^4 h^2 \Omega_m \tag{1.43}$$

Recalling $\omega_r = 1/3$ for relativistic particles, then Equation 1.27 becomes:

$$a^4(t)\rho_r = \rho_{r,0} \tag{1.44}$$

Which shows how the equivalent mass density of relativistic particles varies with the scale factor $a(t)$. Comparing Equation 1.44 with Equation 1.15, we can see that ρ_r increases faster than ρ_m as the scale factor becomes smaller [5].

In the early Universe ($a \to 0$), there must have been an early era when all relativistic particles dominated and governed the expansion of the Universe. The transition from the radiation era to the matter era ocurred when the scale factor satisfied $\rho_r = \rho_m$, or equivalently $\Omega_r = \Omega_m$, then [5]:

$$\begin{aligned} \frac{a_{r,m}^4 \rho_r}{a_{r,m}^3 \rho_m} &= \frac{\rho_{r,0}}{\rho_{m,0}} \\ a_{r,m} &= \frac{\Omega_{r,0}}{\Omega_{m,0}} \end{aligned} \tag{1.45}$$

Matter-dominated Era: The matter-dominated era was the epoch in the evolution of the Universe after the radiation-dominated era. In this stage, the energy density of matter exceeds the energy density of radiation in the Universe, and then, non-relativistic particles became the dominant constituents within the Universe, both dark matter and baryonic matter. According to the ΛCDM model, the cold dark matter dominates the Universe at this stage. This permits the gravitational collapse to make the very slightly more dense regions caused by quantum mechanical irregularities during cosmic inflation become denser, ultimately leading to the formation of the structures we see in the Universe. Although there are strong theories for how the baryonic matter formed, the ΛCDM model does not provide any mechanism for the formation of the cold dark matter (see `http://www.whillyard.com/science-pages/`

matter-epoch.html). Matter-dominated era begins for a redshift $z << z_{\text{eq}}$, where z_{eq} is given by Equation 1.43.

It was thought that matter domination has continued to nowadays, but recent evidence shows that the rate of expansion of the Universe started to increase some 6 to 7 thousand million years ago, leading to the conclusion that the dark energy may have reverse the matter domination and we are in an era of dark energy domination (see http://www.whillyard.com/science-pages/matter-epoch.html).

For a matter-dominated Universe, also called Einstein - de Sitter Universe, the scale factor has the following expression [2]:

$$a(t) = \left(\frac{3}{2}H_0 t\right)^{\frac{2}{3}} \tag{1.46}$$

In this case, the scale factor $a(t)$ has a more rapidly evolution than in the radiation-dominated era.

Λ-dominated Era: For high redshift z, radiation (Ω_r) domains the dynamics of the Universe. At present time, the dynamics is dominated by the cosmological constant (Ω_Λ), and the value of the components of the Universe is approximately:

$$\Omega_{r,0} \sim 10^{-5}; \quad \Omega_{m,0} \sim 0.3; \quad \Omega_{\Lambda,0} \sim 0.7 \tag{1.47}$$

Then, at present time, we can approximate $\Omega_0 = \Omega_{m,0} + \Omega_{\Lambda,0} = 1$, which is the so called De Sitter Universe. In this Universe, the scale factor depends on time as follows [2]:

$$a(t) = \left(\frac{\Omega_{m,0}}{\Omega_{\Lambda,0}}\right)^{\frac{1}{3}} \left[\sinh\left(\frac{3}{2}\Omega_{\Lambda,0}^{1/2} H_0 t\right)\right] \tag{1.48}$$

Which can be expressed as an exponential growth, if we suppose that $\Omega_m = 0$, in this De Sitter Universe:

$$a(t) = a_0 e^{H_0(t-t_0)} \tag{1.49}$$

This exponential growth of the scale factor can be interpreted as an accelerated rate of the expansion of the Universe. In this stage of the evolution of the Universe, the matter density of the Universe is so diluted that it begins losing its capacity to restrain the expansion of the Universe, which hence accelerates. Empty voids of space grow ever larger between local clusters of gravitationally-concentrated matter.

We can find the value of the scale factor in the moment where the transition between the matter-dominated era and the Λ-dominated era, that means, when the respective densities were equal $\rho_m = \rho_v$ or $\Omega_m = \Omega_\Lambda$. The transition value of a is given by:

$$a_{m,\Lambda} = \left(\frac{\Omega_{m,0}}{\Omega_{\Lambda,0}}\right)^{1/3} \tag{1.50}$$

1.4 Formation of Structures

1.4.1 General Framework

The ΛCDM model assumes that structure we observe in the Universe today grows from density perturbations in a hierarchical form, that is, the first structures to form where the small ones, and then, through coalescence of this small structures, the big ones are formed, as Dark Matter haloes where galaxies and galaxy clusters are established [17]. We can define the density contrast of the matter, or in particular of the dark matter, as

$$\Delta(x) = \frac{\rho(x) - \overline{\rho}}{\overline{\rho}} \tag{1.51}$$

Where $\rho(x)$ is the matter density of the Universe at a certan position x, $\overline{\rho}$ is the mean density of matter in all the Universe and $\Delta(x)$ is the called density contrast which measures the fluctuation of the matter density in a point x respect to the mean density of matter. The current density contrast associated with a galaxy will be $\Delta_G \sim 10^6$, for a cluster of galaxies will be $\Delta_C \sim 10^3$ and for a supercluster of galaxies $\Delta_{SC} \sim 10$. Now, the growth of structure will be linear until $\Delta \sim 1$, then as $\rho \sim a^{-3}$, one can see that the redshift at which galaxies start to form is nearly $z \sim 100$, for a cluster $z \sim 10$ and for superclusters $z \sim 1$, in agreement with the assumption of the hierarchical formation [17].

The large scale structures (LSS) emerge from overdensities in the Dark Matter density field, generated by primordial density field fluctuations, allowing the formation of gravitational potential wells or haloes. In those haloes, baryonic matter starts to

cool and collapse. Once the collapse of baryonic matter starts, Jeans unstable hydrogen clouds begin to collapse independently, allowing the formation of the first stars and protogalaxies, which evolved from collisions and coalesence, in a hierarchichal formation [17]. The collapse of baryonic matter starts after decoupling time, when the Universe's temperature has decreased enough such that Compton Effect is no frequent, leaving the radiation free from its interaction with matter. As Dark Matter can not be observed directly, those overdensities may be inferred from the local number density of galaxies on the dark matter haloes [16].

1.4.2 Equation of Evolution of the Density Contrast and Theoretical Model of Linear Fluctuations

Now, we are going to write an equation for the evolution of the density contrast in the expanding Universe. Starting with the equation of conservation of mass (equation of continuity), the equation of motion for an element of a fluid (Euler's equation) and the equation for the gravitational potential in the presence of a mass density distribution ρ (Poisson's equation):

$$\frac{\mathrm{d}\rho(\mathbf{x},t)}{\mathrm{d}t} + \nabla \cdot (\rho(\mathbf{x},t)\mathbf{v}) = 0 \tag{1.52}$$

$$\frac{\mathrm{d}\mathbf{v}}{\mathrm{d}t} + (\mathbf{v}\cdot\nabla)\mathbf{v} = -\frac{\nabla P}{\rho} - \nabla\Phi \tag{1.53}$$

$$\nabla^2\Phi = 4\pi G\rho \tag{1.54}$$

Where Equation 1.52 is the continuity equation, in which ρ represents the density in a certain point $\mathbf{x}$, and $\mathbf{v}$ is the peculiar velocity of the density distribution at this point. Equation 1.53 is the Euler's equation for the motion of an element of a fluid; here P is the pressure and Φ is the gravitational potential. Finally, Equation 1.54 is the Poisson's equation, where G is the gravitational constant.

Performing perturbations on those equations, we can obtain the following expressions:

$$\frac{\mathrm{d}\Delta}{\mathrm{d}t} = -\nabla\cdot\delta\mathbf{v} \tag{1.55}$$

$$\frac{\mathrm{d}\delta\mathbf{v}}{\mathrm{d}t} + (\delta\mathbf{v}\cdot\nabla)\mathbf{v_0} = -\frac{\nabla\delta P}{\rho_0} - \nabla\delta\Phi \tag{1.56}$$

$$\nabla^2\delta\Phi = 4\pi G\delta\rho \tag{1.57}$$

Where Equation 1.55 is the perturbed continuity equation in which Δ is the density contrast from Equation 1.51 and $\delta\mathbf{v}$ is the perturbed peculiar velocity. Equation 1.56 is the perturbed Euler equation, in which $\mathbf{v}_0$ is the unperturbed peculiar velocity and ρ_0 the unperturbed density, and Equation 1.57 is the perturbed Poisson's equation. Those equations lead to the general one:

$$\frac{\mathrm{d}^2\Delta}{\mathrm{d}t^2} + 2\left(\frac{\dot{a}}{a}\right)\frac{\mathrm{d}\Delta}{\mathrm{d}t} - 4\pi G\rho_0\Delta = 0 \tag{1.58}$$

Which is the equation of evolution of the density contrast. It is important to say that the time derivative is a convective derivative, that means:

$$\frac{\mathrm{d}}{\mathrm{d}t} = \frac{\partial}{\partial t} + \mathbf{v}\cdot\nabla \tag{1.59}$$

Solutions for Equation 1.58 can be obtained in the form:

$$\Delta(a) = \frac{5\Omega_0}{2}\left(\frac{1}{a}\frac{\mathrm{d}a}{\mathrm{d}t}\right)\int_0^a \frac{\mathrm{d}a'}{(\mathrm{d}a'/\mathrm{d}t)^3} \tag{1.60}$$

or in terms of Hypergeometric functions or just writing it as:

$$\Delta(\mathbf{x},t) = A(\mathbf{x})D_1(t) + B(\mathbf{x})D_2(t) \tag{1.61}$$

where A and B are to be found. $D_1(t)$ and $D_2(t)$ are called the growing and decaying modes, or growth and decaying amplitudes, respectively.

For a critical or Einstein - de Sitter Universe (i.e. $\Omega_{tot} = \Omega_m = 1$), these solutions can be reduced to:

$$\Delta \propto D_1 \propto t^{2/3} \propto a \tag{1.62}$$

$$\Delta \propto D_2 \propto t^{-1} \propto a^{-3/2} \tag{1.63}$$

The decaying mode is usually discarded in theoretical studies; for longer periods of evolution its amplitude becomes negligible compared with that of the growing mode if we do not have very specific initial conditions.

In this model, although Δ is growing in thime, the physical overdensity $\delta\rho = \rho - \overline{\rho} = \overline{\rho}\Delta$ actually gets smaller: $\delta\rho \sim a^{-2} \sim t^{-4/3}$. In the linear regime, the infall of matter into objects is slower than the expansion of the Universe. The formation of structures is due to the fact that at some limiting value of Δ the process becomes nonlinear and causes a really fast growth of density [15].

A general and almost analitical solution of Equation 1.58 can be found by making a variable change from time t to redshift z as follows [15]:

$$\frac{\mathrm{d}z}{\mathrm{d}t} = -H_0(1+z)E(z) \tag{1.64}$$

Then, the density contrast equation transforms to:

$$\Delta'' + \left(\frac{E'}{E} - \frac{1}{x}\right)\Delta' - \frac{3}{2}\Omega_m \frac{x}{E^2}\Delta = 0 \tag{1.65}$$

With $x = 1 + z$ as a redshift-type variable and the primes denote differentiation with respect to x. Defining a new function $\beta(x)$, the density contrast can be rewritten in terms of this functions:

$$\Delta = E\beta \tag{1.66}$$

With E given by Equation 1.38. Substituting this last definition in Equation 1.58, we get:

$$E\beta'' + \left(3E' - \frac{E}{x}\right)\beta' + \left(E'' + \frac{E'^2}{E} - \frac{E'}{x} - \frac{3}{2}\Omega_m \frac{x}{E}\right)\beta = 0 \tag{1.67}$$

The coefficient for β is zero for any $E^2(x)$ that is a cubic polynomial in x, and this class also includes the E^2 for the canonical $(\Omega_m, \Omega_\Lambda)$ models [15]. Thus, we can write:

$$E\beta'' + \left(3E' - \frac{E}{x}\right)\beta' = 0 \tag{1.68}$$

Which gives

$$\beta' = A\frac{x}{E^3} \tag{1.69}$$

With A constant. The general solution of Equation 1.58 can be written as:

$$\Delta(z) = AD_1(z) + BD_2(z) \tag{1.70}$$

Where the partial solutions $D_1(z)$ and $D_2(z)$ are the growing and decaying modes mentioned in Equation 1.61, respectively. The growing and decaying modes has the following expressions

$$D_1(z) = E(z)\int_z^\infty \frac{(1+z')}{E^3(z')}\,\mathrm{d}z' \tag{1.71}$$

$$D_2(z) = E(z) \tag{1.72}$$

With $E(z)$ given by Equation 1.38. The integral for the growth amplitude can be taken analitically for all $\Omega_\Lambda = 0$ models, but for models with cosmological constant different of zero, solutions have to be found numerically [14].

As we will work only with the growing mode, or near-growth factor D_1, we will call it simply D. Another expression for the growing mode in terms of the scale factor a is given by [13]:

$$D(a) = \frac{5}{2}\left(\frac{\Omega_{m,0}}{\Omega_{\Lambda,0}}\right)^{1/3}\frac{\sqrt{1+y^3}}{y^{3/2}}\int_0^y \frac{y'^{3/2}}{[1+y'^3]^{3/2}}\,\mathrm{d}y' \tag{1.73}$$

$$y \equiv a\left(\frac{\Omega_{\Lambda,0}}{\Omega_{m,0}}\right)^{1/3} \tag{1.74}$$

We can also relate the density contrast with the linear-growth factor by mean of:

$$\Delta(a) = \frac{D(a)}{D(1)} \tag{1.75}$$

For $\Omega_m > 0.1$, the linear-growth factor $D(a)$ can be accurately approximated by:

$$D(a) = \frac{(5/2)a\Omega_m}{\Omega_m^{4/7} - \Omega_\Lambda + (1 + \Omega_m/2)(1 + \Omega_\Lambda/70)} \tag{1.76}$$

With the matter density parameter Ω_m and cosmological constant density parameter Ω_Λ related with the scale factor as follows:

$$\Omega_m(a) = \frac{\Omega_{m,0}}{(1 + y^3)} \tag{1.77}$$

$$\Omega_\Lambda(a) = 1 - \Omega_m(a) \tag{1.78}$$

1.5 Sachs-Wolfe Effect

1.5.1 Cosmic Microwave Background

In 1946, George Gamow was pondering the cosmic abundances of elements. Realizing that the newborn, dense Universe must have been hot enough for a burst of nuclear reactions to occur, he proposed that a sequence of reactions in the very early Universe could explain the measured cosmic abundance curve. Gamow altogether with the work of Alpher and Herman, showed that the Big Bang could explain some features, as the abundance of helium, that other models considering an steady Universe could not explain.

Supossing the early Universe to be hot and dense, so that the mean free path of photons would have been short enough to maintain the thermodynamic equilibrium, the radiation field would have a black-body spectrum. In 1948, Alpher and Herman published their description of how this black-body radiation would have cooled as the Universe expanded, predicting that the Universe should now be filled with the black-body radiation at a temperature of 5 K.

In 1964 two radio astronomers, Arno Penzias and Robert Wilson, were working at Bell Laboratories in Holmdel, New Jersey, with a huge horn reflector antenna that had been used to communicate with the Telstar satellite. They found a persistent hiss in the signal that came from all directions and realize that a 3 K black-body radiation could be producing this interference. The astronomers detected the black-body radiation that fills the Universe, with a peak wavelength of $\lambda_{\text{max}} = 1.06$ mm in the microwave

region of the electromagnetic spectrum, nowadays known as the Cosmic Microwave Background (CMB). In 1991, the COBE satellite measured a temperature of 2.725 K, while nowadays we know the temperature of the black-body spectrum of the CMB is about 2.72548 ± 0.00057 K.

1.5.2 The Origin of the CMB and the Surface of Last Scattering

The copious electrons (e^-) in the hot environment of the very early Universe obstructed the photons (γ) of the CMB, allowing them to travel only relatively short distances before being scattered. The scattering of photons by free electrons kept the electrons in thermal equilibrium, meaning they had the same temperature. As the cross section for photon-proton ($\gamma - p^+$) scattering is smaller than the Thomson cross section for electrons, this interaction can be neglected; but as there is Coulomb interaction between electrons and protons, the protons kept in thermal equilibrum with the electrons and photons.

The expansion of the Universe diluted the number density of free electrons, and the average time between scatterings of a photon by an electron gradually approached the characteristic timescale of universal expansion:

$$\tau_{\text{exp}}(t) \equiv \left(\frac{1}{a(r)} \frac{\mathrm{d}a(t)}{\mathrm{d}t} \right)^{-1} = \frac{1}{H(t)} \tag{1.79}$$

As the time of decoupling approached, photons became disengaged from electrons. If the electrons had remained free, decoupling time would have occurred when the Universe was about 20 millions years old; however, when the Universe was about 1 million years old, the opacity of the Universe was altered and it became transparent. The independent evolution of radiation and matter began when the temperature cooled sufficiently to allow the free electrons to combine with nuclei of hydrogen and helium in a process known as recombination. This process drop the opacity, freeing the photons to roam unhindered throughout this newly transparent Universe. The photons of the CMB that we observe today were last scattered during the time of recombination.

We can define the surface of last scattering as a spherical surface, centered on Earth, from which the CMB photons just now arriving at Earth were last scattered before beginning their unimpeded journey to us. The surface of last scattering is the farthest redshift we can possibly observe at this moment in time. Because of recombination did

not happen all at one, the surface of last scattering actually has a thickness Δz.

Although at the first moments of the Universe the CMB looks to be almost uniform, there exist some perturbations to this uniformity, called CMB anisotropies. Those anisotropies are due to different interactions between the CMB photons and particles or fields, such as the gravitational potential wells, and other anisotropies are due to the movement of the Solar System through the galaxy and even the relative movement of the galaxy in the local cluster. Some of the temperature anisotropies are called primordial anisotropies which are the result of the density perturbations in the early Universe which seeded the formation of galaxies and clusters. Those primordial anisotropies were formed by the scattering of CMB photons before the surface of last-scattering. Other anisotropies are named secondary CMB anisotropies, which occur when the photons were scattered after the surface of last-scattering. The shape of the blackbody spectrum can be altered through inverse Compton scattering by the thermal Sunyaev-Zel'dovich effect. The effective temperature of the blackbody can be shifted locally by a Doppler shift from the peculiar velocity of the scattering medium as well as by passage through the changing gravitational potential caused by the collapse of nonlinear structure or the onset of curvature or cosmological constant domination [9].

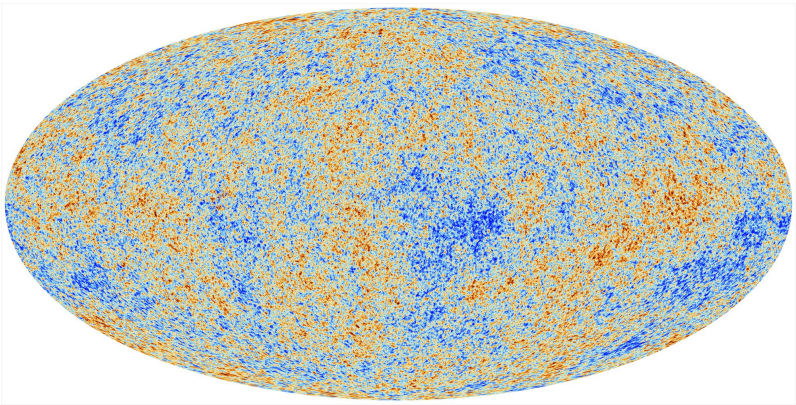

Figure 1.6: Cosmic Microwave Background map from the Planck satellite. This map is of the entire celestial sphere in an equal-area Mollwiede projection. In this map we can see the anisotropies of the CMB. Taken from `http://www.esa.int/Our_Activities/Space_Science/Planck/Planck_and_the_cosmic_microwave_background`

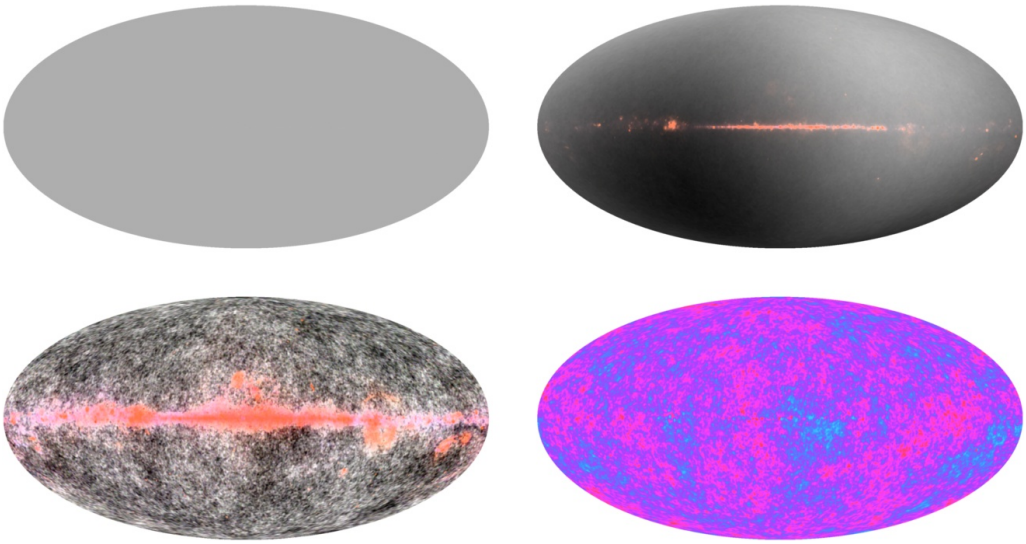

Figure 1.7: The anisotropy of the CMB consists of the small temperature fluctuation in the blackbody radiation left over from the Big Bang. The average temperature of the CMB radiation is 2.72548 K and without any contrast enhancement, the CMB looks like the upper left figure. The dipole anisotropy due to the Doppler shift in the movement of the Solar System can be seen in the in the upper right figure. In this upper right figure we can also see the emission from the Milky Way which dominates the red color in the picture. If the average temperature and the dipole pattern are removed, the intrinsic fluctuations in the CMB can be seen faintly away from the Milky Way in the lower left figure. Combining the multiple frequencies in a way that eliminates the Milky Way, we can see the CMB map in the lower right figure with a 30 000X contrast enhancement. Taken from `http://www.astro.ucla.edu/~wright/CMB-DT.html`.

1.5.3 The Dipole Anisotropy of the CMB

All observers at rest respect to the Hubble flow have no peculiar velocity, and see the same spectrum for the CMB with the same intensity at all directions, i. e., an isotropic CMB. In particular, two observers in different galaxies that are being carried apart by the Hubble flow see the same black-body spectrum. However, there is a Doppler shift of the CMB caused by an observer's peculiar velocity through space, relative to the Hubble flow. Using the Wien's law, a shift in wavelength can be expressed as a change in the temperature of the black-body radiation; for example, a slight blueshift (smaller λ_{max}) would correspond to a slightly higher temperature; while a redshift (larger λ_{max}) would correspond to a slightly lower temperature.

Let's suppose an observer at rest relative to the Hubble flow, who determines that the CMB has a temperature T_{rest}. The temperature measured by and observer with peculiar

velocity v relative to the Hubble flow is:

$$T_{\text{moving}} = \frac{T_{\text{rest}}\sqrt{1 - v^2/c^2}}{1 - (v/c)\cos\theta} \tag{1.80}$$

Being θ the angle between the direction of observation and the direction of motion. Both observers see a black-body spectrum, but the moving observer measures a slightly hotter temperature in the forward direction ($\theta = 0$) and a slightly cooler temperature in the opposite direction. In the case that the peculiar velocity is $v << c$, we can use the fact that $1 - v^2/c^2 \approx 1$ and the geometric serie to find a new expression for Equation 1.80:

$$T_{\text{moving}} = T_{\text{rest}}\left(1 + \frac{1}{c}\cos\theta\right) \tag{1.81}$$

The second term on the right-hand side is called the dipole anisotropy, and has been detected and measured by probes as the COBE and the WMAP. After the dipole anisotropy has been substracted from the CMB, the remaining radiation is highly isotropic, having nearly equal intensity in all directions. The CMB does have hotter and cooler areas, appearing as a patchwork of small regions, about 1° degree of less in diameter, where the temperature departs from the average value T_0 by about one part in 10^5.

1.5.4 The Sunyaev-Zel'dovich Effect (Anisotropy)

It should be emphasized that an observer being carried along with the Hubble flow, i.e., with no peculiar velocity, does not measures a Doppler shift on the CMB. An observer in a distant galaxy receding from us at an appreciable fraction of the speed of light sees the same CMB spectrum that we do. Evidence of this is produced when low-energy photons of the CMB pass through the hot ($\sim 10^8$ K) ionized intracluster gas in a rich cluster of galaxies. A small fraction of the photons (typically 10^{-3} to 10^{-2}) are scattered to higher energies by the high-energy electrones in the gas. This inverse Compton scattering increases the frequency of a scattered photon by an average amount $\Delta\nu$ of:

$$\frac{\overline{\Delta\nu}}{\nu} = \frac{4k_B T_e}{m_e c^2} \tag{1.82}$$

Where k_B is the Boltzmann constant, T_e is the temperature of the electron gas, m_e is the mass of one electron and c is the speed of light. The resulting distortion of the

CMB spectrum is called the thermal Sunyaev Zel'dovich effect. This is sketched in Figure 1.8. Although the spectrum no longer has the precise shape of a blackbody spectrum, its translation to higher frequencies may be used to define an effective decrease ΔT in the temperature of the CMB T_0 of approximately

$$\frac{\Delta T}{T_0} \simeq -2\frac{k_B T_e}{m_e c^2}\tau \tag{1.83}$$

Where τ is the optical depth of the intracluster gas along the line of sight. Typical values of $\Delta T/T_0$ are a few times 10^{-4}. Observations of the Sunyaev-Zel'dovich effect for many clusters of galaxies confirm that it is independent of the cluster's redshift, as expected if the CMB spectrum observed at a cluster is not affected by the cluster's recessional velocity [5].

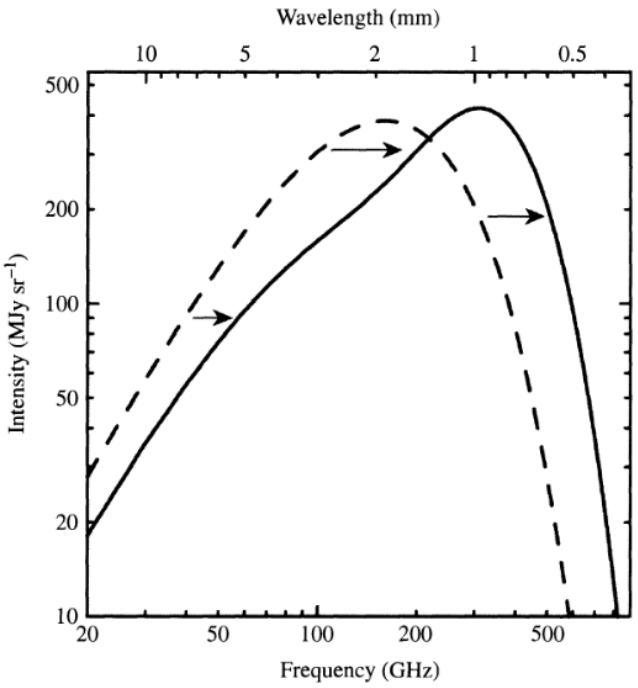

Figure 1.8: The undistorted CMB spectrum (dashed line) and the spectrum distorted by the Sunayev-Zel'dovich effect (solid line). In a rich cluster of galaxies, CMB photons may be scattered to higher frequencies by colliding with the electrons in the hot intracluster gas. For frequencies less than the peak frequency, more photons are scattered out of a frequency interval than into it, so the intensity at that frequency decreases. Similarly, for frequencies greater than the peak frequency, fewer photons are scattered out of a frequency interval than into it, so the intensity at that frequency increases. The net result is a shift of the CMB spectrum to higher frequencies. Taken from [5].

1.5.5 The Integrated Sachs-Wolfe Effect (Anisotropy)

There are two kinds of Sachs-Wolfe effect. The Non-integrated Sachs-Wolfe effect or Ordinary Sachs-Wolfe effect caused by gravitational redshift occurring at the surface of last scattering, to intrinsic temperature inhomogeneities on this last scattering surface and to the inhomogeneities of the metric. The effect is not constant across the sky due to differences in the matter density at the time of last scattering. The Integrated Sachs-Wolfe (ISW) effect occurs between the surface of last scattering and the Earth, and is caused by gravitational redshift, but is not a part of the primordial CMB anisotropies. While most CMB anisotropies are generated at very early times, further fluctuations can be induced gravitationally at late times as photons pass through evolving gravitational potential wells. If dark matter dominates, the gravitational potential wells do not vary with time, but the presence of dark energy or spatial curvature will cause the potentials to evolve at late times, producing new temperature fluctuations, or secondary anisotropies, at low redshift (primarily at $z < 2$), as the photons pass through regions of overdensities or underdensities. Directly observing these new CMB temperature anisotropies is challeging, primarily because their amplitudes are a fraction of the anisotropies arising from higher redshifts.

The theoretical background of the SW effect dates back to 1966, when R. K. Sachs and A. M. Wolfe found solutions to the linear perturbations of the Einstein's field equations, in order to obtain fluctuations of the density field [21].

In a Λ-CDM Universe, dominance of the cosmological constant Λ causes that the scale factor a grows at a faster rate than the linear growth of density perturbations Δ. Consequently, the cosmological constant has the direct dynamical effect of causing gravitational potential perturbations to decay as $\delta\Phi \propto -\Delta/a$. The ISW effect is caused by the change in the energy of CMB photons as they traverse these linearly evolving potentials. When CMB photons pass through an overdense region, it will gain more energy falling into the potential well than the energy it will lose when climbing out of the evolved shallower potential well. The potential well will become shallower due to the expansion of the Universe. Therefore, overdense regions correspond to hot regions in a linear ISW map. Conversely, when a CMB photon pass through an underdense region, the potential fluctuation is positive and the photon loses more energy while climbing the potential hill than the energy it will gain when from its descent. Then, underdense regions appear cold in a linear ISW map [4].

The change of the energy of the CMB photons can be associated with a change in the temperature, that means that the temperature fluctuations are related to the evolution of the gravitational potential. The temperature fluctuation along a direction $\hat{\mathbf{n}}$ can be written as an integral of the time derivative of the gravitational potential, $\dot{\Phi}$, from the last scattering surface to the present [4]:

$$\Delta T(\hat{\mathbf{n}}) = \frac{2}{c^2}\overline{T}_0 \int_{t_L}^{t_0} \dot{\Phi}(t, \hat{\mathbf{n}})\, \mathrm{d}t \tag{1.84}$$

Where t is the cosmic time, t_L the age of the Universe at the last scattering surface, t_0 the present age of the Universe, $\dot{\Phi}$ the time derivative of the gravitational potential, $\overline{T_0}$ the mean CMB temperature and c the speed of light. This is equivalent to the integral over radial comoving distance x_r [4]:

$$\Delta T(\hat{\mathbf{n}}) = \frac{2}{c^3}\overline{T}_0 \int_{0}^{x_{r,L}} \dot{\Phi}(x_r, \hat{\mathbf{n}})\, \mathrm{d}x_r \tag{1.85}$$

Where $x_{r,L}$ is the comoving distance to the last scattering surface.

The expression for the time derivative of the gravitational potential may be obtained by means of the the Poisson equation of gas dynamics for a fluid in a gravitational field in comoving coordinates, mentioned in Equation 1.57. Solving this equation by means of Fourier methods, we can find the gravitational potential:

$$\Phi(\mathbf{k}, t) = -4\pi G a^2 \overline{\rho}(t) \frac{\Delta(\mathbf{k}, t)}{k^2} \tag{1.86}$$

When taking the time derivative of Equation 1.86, an expression for the time derivative of the gravitational potential $\dot{\Phi}$, in the Fourier space can be found, as follows:

$$\dot{\Phi}(\mathbf{k}, t) = -\frac{3}{2}\frac{H_0^2}{k^2}\Omega_{m,0}\left[\frac{H(t)}{a(t)}\Delta(\mathbf{k}, t) + \frac{\dot{\Delta}(\mathbf{k}, t)}{a(t)}\right] \tag{1.87}$$

From Equation 1.87, we can see a dependence on the matter density parameter Ω_m, on the Hubble's function $H(t)$, in the contrast density Δ and even in the evolution on time of the contrast density $\dot{\Delta}$, which means that the evolution of the gravitational potential well depends on how the fluctuations of the matter density evolves in time. Figure 1.9 shows a brief sketch of the energy change that the photons of the CMB undergo due to the Sachs-Wolfe effect.

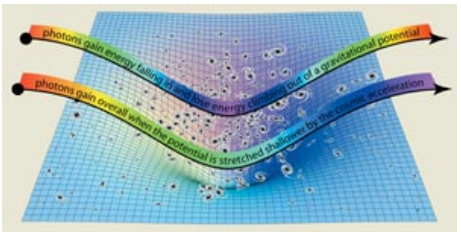

Figure 1.9: Scheme of the Sachs-Wolfe effect. When the photons pass through a gravitational potential, they will gain energy when falling off the potential and will lose energy when climb it. The difference in the energy they gain or lose depends on the expansion rate of the Universe. Taken from `http://cmbcorrelations.pbworks.com/w/page/4563978/The%20late-time%20integrated%20Sachs%20Wolfe%20effect`

1.5.6 Cosmic Harmonics and Accoustic Oscillations

When the Universe was roughly 10^5 yrs old, it became filled with sound waves that traveled through the primordial plasma composed by photons and baryonic matter.

As the density of a region was enhanced by a compression, it was heated by a small amount $\delta T/T \approx 10^{-5}$, until radiation pressure reverse the motion. Similarly, as the density was diminished by an expansion, it cooled. The small amplitude of the sound waves means that a passing wave will cause the photon-baryon fluid to execute simple harmonic motion. This motion continued until the time of decoupling, when electrons (e^-s) combined with the protons (p^+s) and heavier nuclei formed in Big Bang nucleosynthesis.

The photons of the CMB carried with the signature of these accoustic oscillations. Some areas of the CMB appear slightly hotter, others slightly cooler. The frequency of the photons is also affected by the Sachs-Wolfe Effect, as the photons lose energy when they climb out of the gravitational potential wells of the density fluctuations. We will return to this issue later.

The overall pattern of CMB temperature variations on the celestial sphere can be expressed as the sum of spherical harmonic functions $Y_m^l(\theta, \phi)$. The temperature fluctutation in the direction of the angular position (θ, ϕ) is:

$$\frac{\Delta T(\theta, \phi)}{T} = \sum_{l=1}^{\infty} \sum_{m=-l}^{l} a_{lm} Y_{lm}(\theta, \phi);\ a_{lm} \in \mathbb{C} \tag{1.88}$$

The value of a_{lm} can be determined by observing the CMB and making measurements of $\delta T/T$ in all directions. The term $l = 1$ is the dipole anisotropy through space relative to the Hubble flow. Now, defining the correlation function $C(\theta)$ as:

$$C(\theta) =< \Delta T(\mathbf{n_1})\Delta T(\mathbf{n_2}) > |_{\mathbf{n_1}\cdot\mathbf{n_2}=\cos\theta} \tag{1.89}$$

$$= \frac{1}{4\pi}\sum_l (2l+1)C_l P_l(\cos\theta) \tag{1.90}$$

Where C_l is defined as an ensemble average with spherical symmetry, or as an angular average over the $2l + 1$ values of m, in order to avoid the effect of an arbitrary choice of $\phi = 0$:

$$C_l =< |a_{lm}|^2 >\simeq \frac{1}{2l+1}\sum_m |a_{lm}|^2 \tag{1.91}$$

At small l, the values of the two expressions of Equation 1.91 differ appreciably due to cosmic variance. With the help of the orthogonality of the Legendre polynomials, we have a relation between C_l and the correlation function $C(\theta)$:

$$C_l = 2\pi\int_0^\pi C(\theta)P_l(\cos\theta)\sin\theta \mathrm{d}\theta \tag{1.92}$$

The values of C_l contain much information about the physical conditions and constituents of the early Universe. From Equation 1.91, we can define the angular power spectrum to be $l(l + 1)C_l/2\pi$. Every term in the summation is ≥ 0, so both positive and negative temperature fluctuations contribute to the angular power spectrum withouth cancelling each other. We will see more about the angular power spectrum in the following section.

1.5.7 The Angular Power Spectrum of the CMB

From Equation 1.88, we can define the expansion coefficients a_{lm} as:

$$a_{lm} = \int \Delta T\, Y^*_{lm}(\theta,\phi)\,\mathrm{d}\Omega \tag{1.93}$$

We can take an ensemble average:

$$< a_{lm}\, a^*_{l'm'} >= \iint \mathrm{d}\Omega_1\, \mathrm{d}\Omega_2\, Y^*_{lm}(\mathbf{n_1})\, Y_{l'm'}(\mathbf{n_2}) < \Delta T(\mathbf{n_1})\, \Delta T(\mathbf{n_2}) > \tag{1.94}$$

Assuming spherical symmetry, the autocorrelation function $< \Delta T(\mathbf{n_1})\, \Delta T(\mathbf{n_2}) >$ can only depend on θ_{12}, where $\cos\theta_{12} = \mathbf{n_1} \cdot \mathbf{n_2}$. Expanding the autocorrelation function in Legendre polynomials P_n:

$$< \Delta T(\mathbf{n_1})\, \Delta T(\mathbf{n_2}) >= \sum_n k_n\, P_n(\cos\theta_{12}) \tag{1.95}$$

Where k_n are constant expansion coefficients, and with the addition theorem of spherical harmonics:

$$\sum_j Y_{nj}(\mathbf{n_1})\, Y^*_{nj}(\mathbf{n_2}) = \frac{2n+1}{4\pi}\, P_n(\cos\theta_{12}) \tag{1.96}$$

Using Equation 1.95 and Equation 1.96 in Equation 1.94, renaming $C_n = 4\pi k_n/(2n+1)$ and applying some properties of the spherical harmonics, we can obtain the equality in Equation 1.91. Hence:

$$C_l = \int \mathrm{d}\Omega_1 \int \mathrm{d}\Omega_2\, Y^*_{lm}(\mathbf{n_1})\, Y_{lm}(\mathbf{n_2})\ < \Delta T(\mathbf{n_1})\, \Delta T(\mathbf{n_2}) > \tag{1.97}$$

Summing Equation 1.97 over m, produces a factor of $2l+1$ on the left, while on the right using Equation 1.96:

$$\sum_{m=-l}^{l} C_l = (2l+1)C_l = \frac{2l+1}{4\pi} \int \mathrm{d}\Omega_1 \int \mathrm{d}\Omega_2\, P_l(\cos\theta)\ < \Delta T(\mathbf{n_1})\, \Delta T(\mathbf{n_2}) > \tag{1.98}$$

From Figure 1.10, the integration over Ω_2 in Equation 1.98 is performed first using spherical coordinates in the $x'y'z'$-frame at fixed $\mathbf{n_1}$. In this fram the coordinates of $\mathbf{n_2}$ are θ_{12} and ϕ_{12}. Because the integrand is axially symmetric around the z'-axis, we have:

$$\int \mathrm{d}\Omega_2 = 2\pi \sin\theta_{12} \mathrm{d}\theta_{12} \tag{1.99}$$

Spherical symmetry renders the remaining integrand independent of $\mathbf{n_1}$, so that $\int \mathrm{d}\Omega_1$ produces just a factor of 4π. Then:

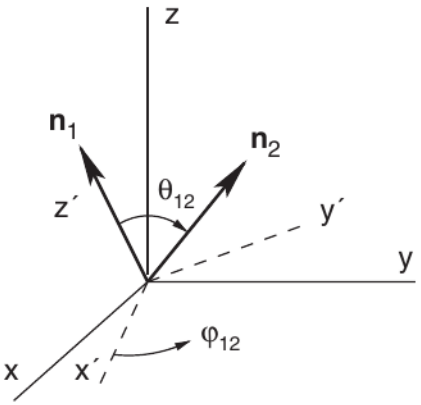

Figure 1.10: The integration over Ω_2 in Equation 1.98 is performed first, using spherical coordinates in the $x'y'z'$-frame at fixed $\mathbf{n}_1$. In this frame the coordinates of $\mathbf{n}_2$ are $\theta_{12},\ \varphi_{12}$. Because the integrand is axially symmetric aroun the z'-axis we have the expression of Equation 1.99, and the result is Equation 1.100. Spherical symmetry renders the remaining integrand independent of $\mathbf{n}_1$, so that $\int \mathrm{d}\Omega_1$ produces just a factor 4π. Image taken from [11].

$$C_l = \frac{1}{4\pi}\int \mathrm{d}\Omega_1 \int_0^\pi 2\pi\ \sin\theta_{12}\,\mathrm{d}\theta_{12}\ <\Delta T(\mathbf{n_1})\ \Delta T(\mathbf{n_2})>|_{\mathbf{n_1}\cdot\mathbf{n_2}=\cos\theta_{12}} \tag{1.100}$$

$$C_l = \frac{4\pi}{2}\int_0^\pi C(\theta)\ P_l(\cos\theta)\ \sin\theta\,\mathrm{d}\theta \tag{1.101}$$

Where we have changed $\theta_{12} \to \theta$ and applied Equation 1.89. This last equation is Equation 1.92. Now, expanding $C(\theta)$ in Legendre polynomials:

$$C(\theta) = \sum_n A_n\ P_n(\cos\theta) \tag{1.102}$$

Inserting this last equation in Equation 1.101, and using:

$$\int_{-1}^{1} P_n(x)\ P_m(x)\,\mathrm{d}x = \frac{2}{2n+1}\delta_{nm} \tag{1.103}$$

We obtain:

$$C_l = 2\pi\int_0^\pi A_n\ P_n(\cos\theta)\ P_l(\cos\theta)\ \sin\theta\,\mathrm{d}\theta \tag{1.104}$$

$$\Rightarrow A_l = \frac{(2l+1)\ C_l}{4\pi} \tag{1.105}$$

Finally, replacing A_n in the expansion in Legendre polynomials for $C(\theta)$ and changing $n \to l$:

$$C(\theta) = \sum_l \frac{(2l+1)\, C_l}{4\pi} \, P_l(\cos\theta) \tag{1.106}$$

Which is Equation 1.90. Remembering the concept of the angular power spectrum given by

$$l(l+1)C_l/2\pi \tag{1.107}$$

from Equation 1.91. This power spectrum is shown in Figure 1.11. In this power spectrum, we speak of an angular frequency called the multipole moment l. The reciprocal of l corresponds to the angular scale. For example, $l = 10$ corresponds to roughly 10 degrees on the sky, and $l = 100$ corresponds to roughly 1 degree on the sky (see `http://background.uchicago.edu/~whu/intermediate/map5.html`).

The angular power spectrum of the anisotropy of the CMB contains information about th formation of the Universe and its current contents. This angular power spectrum is a plot of how much the temperature varies from point to point on the sky (the y-axis variable) $vs.$ the angular frequency l (see `http://www.astro.ucla.edu/~wright/CMB-DT.html`).

The power spectrum shows a flat plain for small values of l, a fundamental peak around $l \simeq 200$, which corresponds to an angular size of about 1^{o} on the sky, and a few harmonics peaks whose heights decline as l approaches 1000; those peaks are called accoustic peaks. A detailed analysis shows that the location of the first peak is sensitive to the value of Ω_0, given by $l \simeq 200/\sqrt{\Omega_0}$. This angular power spectrum can be seen in Figure 1.11 where it is shown the best fit of the ΛCDM model, and in Figure 1.12, where we can see the relation between the different anisotropies and the angular power spectrum.

1.6 Cosmological Simulations of Formation of Structures

This section is a brief summary of the the information found in [12] and [6].

In the hierarchical picture of structure formation, small objects collapse first and then merge to form larger and larger structures in a complex manner. This formation process is evident in the intricate structure of galaxy clusters, whose properties depend on how

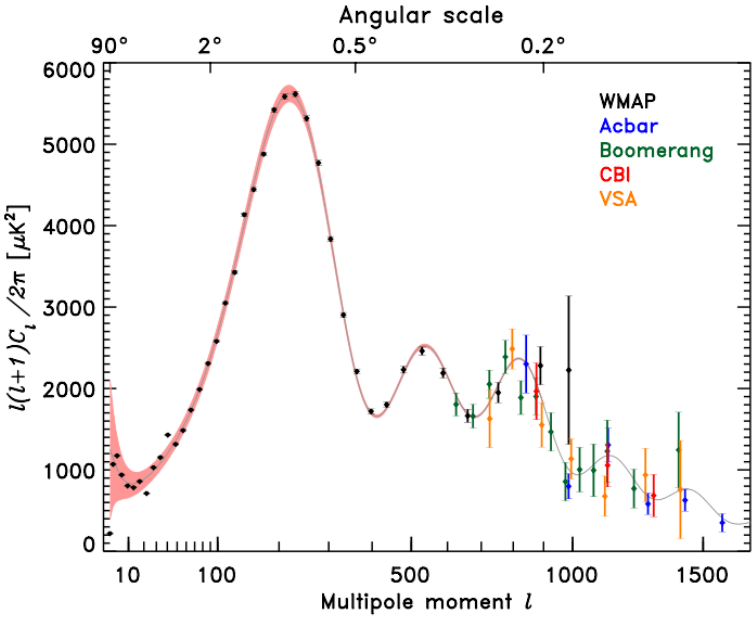

Figure 1.11: The angular power spectrum of the temperature fluctuations in the CMB. The solid line is the best-fit ΛCDM model.

the thousands of smaller objects that the cluster accretes are destroyed or survive within the cluster gravitational potential. These merging events are source of processes such as shocks, turbulence and acceleration of relativistic particles in the intracluster medium. In order to model these processes realistically, we need to resort to numerical simulations which are capable of resolving and following correctly the highly non-linear dynamics. Numerical simulation in cosmology have a long history, numerous important aplications and play a very significant role. It all started in the 60s (Aarseth 1963) and 70s (Peebles 1970; Press & Schechter 1974) with simple N-body problems solved using N-body codes with a few hundred particles. Later the Particle-Particle (PP) code, or direct summation of all two-body forces, was polished and brought to the state-of-art (Aarseth 1985). From this moment, problems such a more realistic density profile and the generation of initial condition with given amplitude and spectrum of fluctuations were solved with the help of different approximations to the structure-formation models and the implementation of a variety of new numerical methods and codes which allows to find more resolution in the forces calculation and particle's positions. Some methods are described in the following sections.

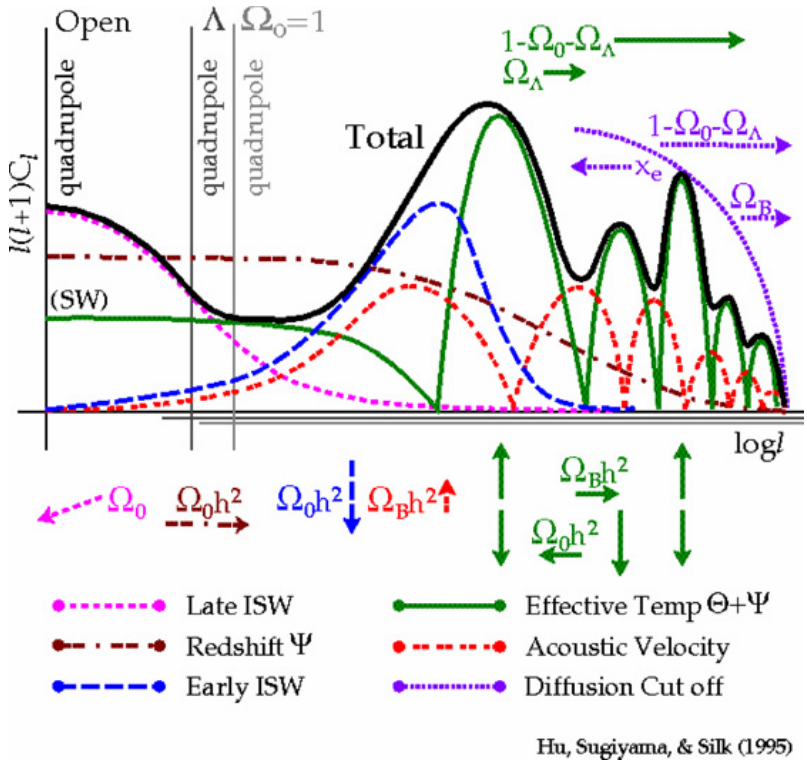

Figure 1.12: Anisotropies in the angular power spectrum of the CMB. We can see the contributions of the Non-integrated SW effect, or Early SW effect, which is produced in the surface of last scattering and the contribution of the ISW effect, or Late SW effect, which is the effect we are studying in this work. The Late SW effect contributes only for small multipole moment l which means that it can be detected only in large scales.

1.6.1 N-body Simulations and Equations of Evolution of Fluctuations in Expanding Universe

Usually the problem of the formation and dynamics of cosmological objects is formulated as N-body problem: for N point-like objects with given initial positions and velocities find their positions and velocities at any later moment. Over most of the cosmic time of interest for structure formation, the Universe is dominated by dark matter. The most favourable model turned out to be the so-called Cold Dark Matter (CDM) model. The CDM can be described as a collisionless, non-relativistic fluid of particles of mass m, comoving coordinate position $\mathbf{x}$ and momentum $\mathbf{p}$. In general, if we neglect the baryonic component, the system is described by the distribution functions $f_i(\mathbf{x}, \mathbf{p}, t)$; for a simple CDM model we have only one component. The phase-space distribution function of the dark-matter fluid (CDM) can be described by the collisionless Boltzmann equation (CBE or Vlasov equation) coupled to the Poisson equation:

$$\frac{\partial f}{\partial t} + \frac{\mathbf{p}}{ma^2}\nabla f - m\nabla\Phi\frac{\partial f}{\partial \mathbf{p}} = 0; \text{ where } \mathbf{p} = ma^2\dot{\mathbf{x}} \tag{1.108}$$

$$\nabla^2\Phi(\mathbf{x}, t) = 4\pi G a^2[\rho(\mathbf{x}, t) - \overline{\rho}(t)] \tag{1.109}$$

Here the proper mass density can be inferred by integrating the distribution function over the momenta $\mathbf{p}$.

$$\rho(\mathbf{x}, t) = \int f(\mathbf{x}, \mathbf{p}, t)\,\mathrm{d}^3p \tag{1.110}$$

This set of equations represents a high-dimensional problem. The solution of the CBE equation can be written in terms of equations of characteristics, which *look* like equations of particle motion:

$$\frac{\mathrm{d}\mathbf{p}}{\mathrm{d}t} = -m\nabla\Phi \tag{1.111}$$

$$\frac{\mathrm{d}\mathbf{x}}{\mathrm{d}t} = \frac{\mathbf{p}}{ma^2} \tag{1.112}$$

These equations can be written in other expression when using the proper peculiar velocity $\mathbf{v} = a\dot{\mathbf{x}}$:

$$\frac{\mathrm{d}\mathbf{v}}{\mathrm{d}t} + \mathbf{v}\frac{\dot{a}}{a} = -\frac{\nabla\Phi}{a} \tag{1.113}$$

Where the time derivative of the scale factor $\dot{a}$, can be obtained from the Friedmann equation as follows:

$$\dot{a} = H_0\sqrt{1 + \Omega_{m,0}(a^{-1} - 1) + \Omega_\Lambda(a^2 - 1)} \tag{1.114}$$

One of the most famous N-body simulation is the Millennium simulation performed by the Virgo Consortium in 2005. With the help of the Max Planck Society's Supercomputing Centre in Garching, Germany, they trace the evolution of the matter distribution in a cubic region of the Universe over 2 thousand million light-years on a side of

2160^3 particles, where each particle represents approximately a thousand million solar masses of dark matter. They have been able to recreate the evolutionary histories both for 20 million or so galaxies which populate this volume and for the supermassive black holes which occasionally power quasars at their hearts. By comparing such simulated data to large observational surveys, they can clarify the physical processes underlying the buildup of real galaxies an black holes (see `http://www.mpa-garching.mpg.de/galform/virgo/millennium/`). A picture with some results is shown in Figure 1.13.

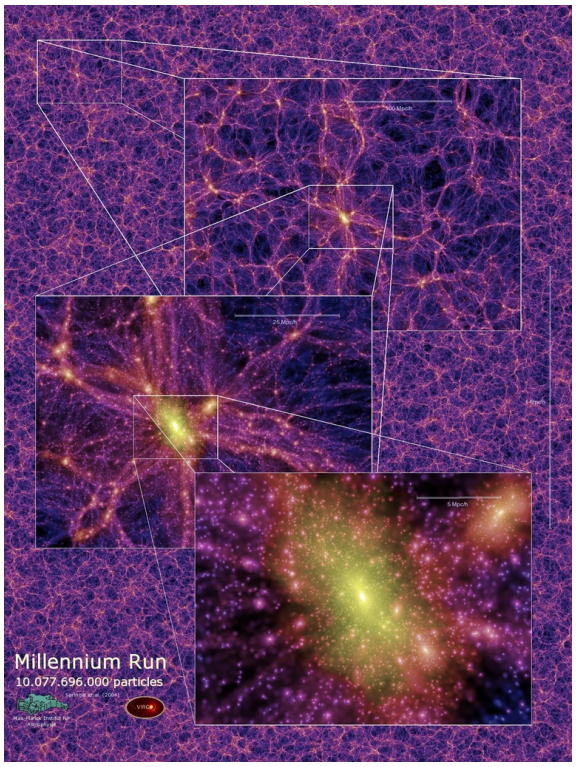

Figure 1.13: Results from the Millenium Project, 2005. The results of this simulation show us filaments and other structures also detected in the observations. Taken from `http://www.mpa-garching.mpg.de/galform/virgo/millennium/`.

1.6.2 Codes and Methods

There are many different numerical techniques to follow the evolution of a system of many particles. Most of the methods for cosmological applicaitons take some ideas from three techniques: Particle Mesh (PM) code, direc summation of Particle-Partilce code, and the TREE code. All methods have their advantages and disadvantages.

Direct Sum: The most direct way to solve the N-body problem is to sum directly the contributions of all the individual particles to the gravitational potential $\Phi(\mathbf{r})$:

$$\Phi(\mathbf{r}) = -G \sum_j \frac{m_j}{(|\mathbf{r} - \mathbf{r}_j|^2 + \epsilon^2)^{1/2}} \tag{1.115}$$

Where G is the gravitational constant, m_j is the mass of j-ith particle, $\mathbf{r}_j$ its respective position and ϵ is a gravitational softening. In principle, this sum would represent the exact (Newtonian) potential which generates the particle's acceleration. In a collisionless models close encounters between individual particles are irrelevant to the physical problem under considerations, but in such N-body simulations, close encounter could occur, giving some numerical inconsistencies, then the gravitational force between two particles must be smoothed by introducing the gravitational softening ϵ. This softening reduces the spurious two-body relaxation which occurs when the number of particles in the simulation is not large enough to represent correctly a collisionless fluid. This situation however is unavoidable, because the number of dark matter particles in real systems is orders of magnitude larger than the number that can be handled in a numerical simulation. Typically, ϵ is chosen to be $1/20 - 1/50$ of the mean inter-particle separation within the simulation. In general, this direct-sum approach is considered to be the most accurate technique, and is used for problems where superior precision is needed. However this method has the disadvantage of being already quite CPU intensive for even a moderate number of particles , because the computing time is $\propto N^2$, where N is the total number of particles.

PM Code: This method uses a mesh to produce density and potential. As the result, its resolution is limited by the size of the mesh. There are two advantages of the method: (1) it is fast, because it has the smallest number of operations per particle per time step of all the other methods, (2) it typically uses very large number of particles.

The PM method treats the force as a field by computing it on a mesh. Differential operators, such as the Laplacian, are replaced by finite difference approximations Potentials and forces at particle positions are obtained by interpolation on the array of mesh-defined values. Typically, such an algorithm is performed in three steps. First, the density on the mesh point is computed by assigning densities to the mesh from the particle positions. Second, the density field is transformed to Fourier space, where the Poisson equation is solved. Alternatively, the potential can be determied by solving Poisson's equation iteratively with relaxation methods. In a third step the forces for the individual particles are obtained by interpolating the derivatives of the potential of the particle positions. Typically, the amount of mesh cells N_g used is lower respect to the number of particles in the simulation, so that when structures form, one can have large

numbers of particles within individual mesh cells, which immediately illustrates the shortcoming of this method: its limited resolution. On the other hand, the calculation of the Fourier transform via a Fast Fourier Tranform (FFT) is extremely fast, as it only needs of order $N_g \log(N_g)$ operations, which is the advantage of this method.

There are many schemes to assign the mass density of the mesh. The simplest method is the "Nearest-Grid-Point" (NGP). Here, each particle is assigned to the closest mesh point, and the density at each mesh point is the total mass assigned to the point divided by the cell volume. One of its drawbacks is that it gives forces that are discontinuous. The "Cloud-in-a-Cell" (CIC) scheme is a better approximation to the force: it distributes every particle over the nearest 8 grid cells, and then weigths them by the overlapping volume, which is obtained by assuming the particle to have a cubic shape of the same volume as the mesh cells. The CIC method gives continuous forces, but discontinuous first derivatives of the forces. A more accurate scheme is the "Triangular-Shaped-Cloud" (TSC) method. This scheme has an assignment interpolation function that is piecewise quadratic.
The advantage of such PM methods is the speed, because the number of operations scales with $N + N_g \log(N_g)$, where N is the number of particles and N_g the number of mesh points. However, the disadvantage is that the dynamical range is limited by N_g, which is usually limited by the available memory. An sketch of a PM code can be seen in Figure 1.14.

P^{3}M Code: This method has two parts: A PM part which takes care of large-scale forces, and PP part, which adds small-scale particle-particle contribution. Because of strong clustering at late stages of evolution, PP part becomes prohibitively expensive once large objects start to form in large numbers. One of the major problems for these codes is the correct splitting of the force into a short-range and long-range part. The PM method is only able to produce reliable inter particle forces down to a minimum of at least two grid cells. For smaller separations the force can no longer be represented on the grid and therefore it is necessary to introduce a cut-off radius r_e (larger than two grid cells), where for $r < r_e$ the force should smoothly go to zero. The parameter r_e defines the chaining-mesh and for distances smaller than this cut-off radius a contribution from the direct PP summation needs to be added to the total force acting on each particle. This PP force should smoothly go to zero for very small distances in order to avoid unphysical particle-particle scattering. This cutoff of the PP force determines the overall force resolution of a P^3M code. An sketch of this P^{3}M method is shown in Figure 1.15 .

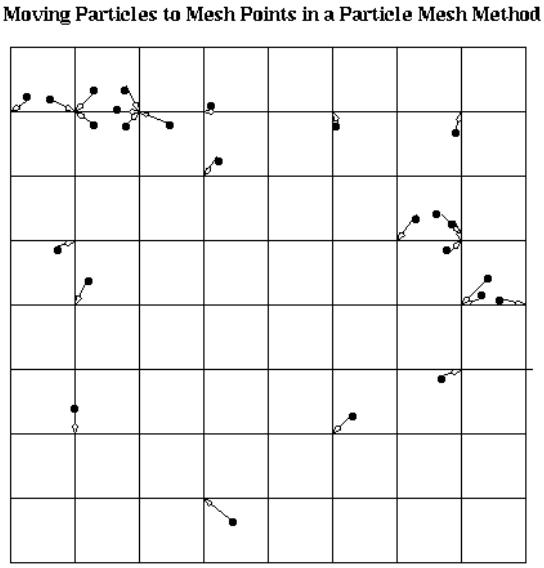

Figure 1.14: Particle-Mesh method. This method superimposes a regular grid over the set of particles, and creates an approximation of the original problem by moving particles to the nearest grid points. Taken from `http://www.cs.berkeley.edu/~demmel/cs267/lecture16/lecture16.html`.

TREE Code: It is the most flexible code in the sense of the choice of boundary contidions. It is also more expensive than PM: it takes 10-50 times more operations. The method of the tree algorithm consist in solving the N-body problem with a hierarchical multipole expansion. This method groups distant particles into larger cells, allowing their gravity to be accounted for by means of a single or many multipole force terms. Instead of requiring $N-1$ partial force evaluations per particle, as needed in a direct-summtion approach, the gravitational force on a single particle can be computed with substantially fewer operations, because distant groups are treated as "macro" particles in the sum. In this manner the sum usually reduces to $N \log(N)$ operations.This scaling is only true for homogeneous particle distributions. An schematic illustrations of a tree code is shown in Figure 1.16.

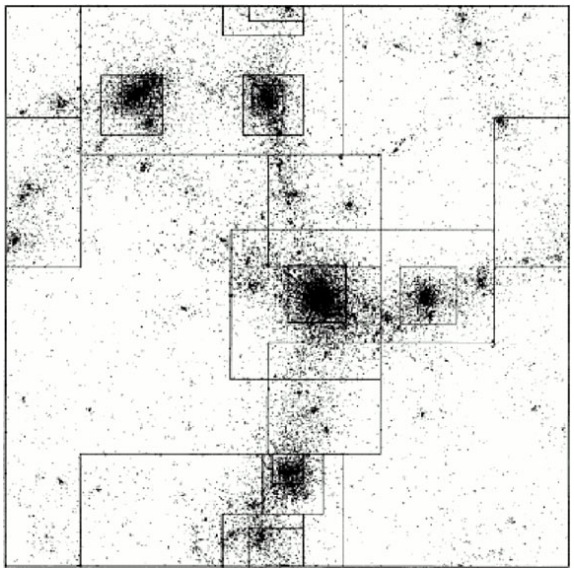

Figure 1.15: Distribution of grid refinements placed with a particular kind of P^3M method. Taken from `http://www.cs.berkeley.edu/~demmel/cs267/lecture16/lecture16.html`.

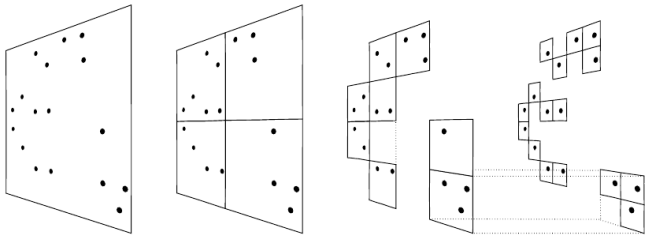

Figure 1.16: Schematic illustration of a kind of Tree code, called Barnes and Hut approximation. The particles are first enclosed in a square (root node). This square is then iteratively subdivided into four squares of half the size, until exactly one particle is left in each final square (leaves of the tree). In the resulting tree structure, each square can be the progenitor of up to four siblings. Taken from [6].

" Where are we? Who are we? We find that we live on an insignificant planet of a hum-drum star lost in a galaxy tucked away in some forgotten corner of a Universe in which there are far more galaxies than people."

Carl Sagan.

CHAPTER

2

Construction of the Maps of Density Fluctuation, Gravitational Potential and Time Derivative of the Gravitational Potential

In this chapter, we are going to describe the methods used for the construction of the density maps, the potential maps and the time derivative of the potential maps. In order to obtain such maps, we used the Fourier techniques and the Fast Fourier Transform using the FFTW[1] library to deal with discrete data. More developed theory of the Fourier Transforms and discrete Fourier Transforms can be found in [19], which is our guide textbook for this chapter.

[1] http://www.fftw.org/

2.1 Fourier Transform

2.1.1 Analytical Development

A physical process can be described in the time domain t, by the values of some quantity h as a function of t, e.g. $h(t)$, or else in the frequency domain f, where the process is specified by giving its amplitude H. In general H is a complex number that also indicates the phase and is expressed as a function of frequency f, that is $H(f)$ with $-\infty < f < \infty$. For many purposes it is useful to think of $h(t)$ and $H(f)$ as being two different representatios of the same function. One goes back and forth between two representations by means of the Fourier Transform (FT) equations:

$$H(f) = \int_{-\infty}^{\infty} h(t)\, e^{-2\pi \mathrm{i} f t}\, \mathrm{d}t \tag{2.1}$$

$$h(t) = \int_{-\infty}^{\infty} H(f)\, e^{2\pi \mathrm{i} f t}\, \mathrm{d}f \tag{2.2}$$

If the time is measured in seconds $[t] = \mathrm{s}$, then the frequency is measured in cycles per second or Hertz, $[f] = \mathrm{Hz}$. It must be remarked that the definition in the sign convention in the exponential of both equations is not important meanwhile it would be maintained in all the transforms. In particular, in our computational implementation with the FFTW library for the programming language C the convention for the direct transform is the same shown in Equation 2.1 and the inverse transform is the same as in Equation 2.2. For instance, in other textbooks like [19] the convention is $e^{2\pi \mathrm{i} f t}$ for the direct transform and $e^{-2\pi \mathrm{i} f t}$ for the inverse.

We can use the relation between angular frequency ω and the frequency f: $\omega = 2\pi f \Rightarrow H(\omega) = [H(f)]_{f=\omega/(2\pi)}$. Equation 2.1 and Equation 2.2 become:

$$H(\omega) = \frac{1}{\sqrt{2\pi}} \int_{-\infty}^{\infty} h(t)\, e^{-\mathrm{i}\omega t}\, \mathrm{d}t \tag{2.3}$$

$$h(t) = \frac{1}{\sqrt{2\pi}} \int_{-\infty}^{\infty} H(\omega)\, e^{\mathrm{i}\omega t}\, \mathrm{d}\omega \tag{2.4}$$

The normalization convention also depends on the application, and the important issue is to be maintained along all the transform processes. In later sections we will discuss in detail all the conventions used in our implementation with the FFTW library.

From Equation 2.1, it is evident at once that Fourier transformation is a linear operation:

- The transform of the sum of two functions $h(t)$ and $g(t)$ is equal to the sum of the transforms:

$$\frac{1}{\sqrt{2\pi}}\int_{-\infty}^{\infty}(h(t)+g(t))\ e^{-\mathrm{i}\omega t}\,\mathrm{d}t = \frac{1}{\sqrt{2\pi}}\int_{-\infty}^{\infty}h(t)\,e^{-\mathrm{i}\omega t}\,\mathrm{d}t + \frac{1}{\sqrt{2\pi}}\int_{-\infty}^{\infty}g(t)\,e^{-\mathrm{i}\omega t}\,\mathrm{d}t \tag{2.5}$$

- The transform of a constant C times a functions $h(t)$ is the same constant times the transform of the function:

$$\frac{1}{\sqrt{2\pi}}\int_{-\infty}^{\infty}C\,h(t)\,e^{-\mathrm{i}\omega t}\,\mathrm{d}t = \frac{C}{\sqrt{2\pi}}\int_{-\infty}^{\infty}h(t)\,e^{-\mathrm{i}\omega t}\,\mathrm{d}t \tag{2.6}$$

Table 2.1 gives correspondences between symmetries in the two domains.

If	Then
$h(t)$ is real	$H(-f) = [H(f)]^* = H^*(f)$
$h(t)$ is imaginary	$H(-f) = -H^*(f)$
$h(t)$ is even	$H(-f) = H(f)$ ($H(f)$ is even)
$h(t)$ is odd	$H(-f) = -H(f)$ ($H(f)$ is odd)
$h(t)$ is real and even	$H(f)$ is real and even
$h(t)$ is real and odd	$H(f)$ is imaginary and odd
$h(t)$ is imaginary and even	$H(f)$ is imaginary and even
$h(t)$ is imaginary and odd	$H(f)$ is real and odd

Table 2.1: Symmetries of the Fourier transform

Other important propeties of the Fourier tranform can be found in more detail in [19], [1] and [22].

With two functions $h(t)$ and $g(t)$, and their corresponding Fourier transforms $H(f)$ and $G(f)$, we can form two combinations of special interest: the *convolution* and the *correlation*.

2.1.1.0.1 Convolution:

The *convolution* of the two functions, denoted $g * h$ is defined by:

$$g * h \equiv \int_{-\infty}^{\infty} g(\tau)h(t-\tau)\,\mathrm{d}\tau \tag{2.7}$$

$g * h$ is a function in the time domain, and $g * h = h * g$. We define the Convolution Theorem, which allow us to find the product of $F(f)$ $G(f)$ with the transform of the convolution $g * h$:

$$\begin{aligned}\frac{1}{\sqrt{2\pi}}\int_{-\infty}^{\infty}(g(t) * h(t))\ e^{-\mathrm{i}\omega t}\,\mathrm{d}t &= \frac{1}{\sqrt{2\pi}}\int_{-\infty}^{\infty} g(t)\ e^{-\mathrm{i}\omega t}\,\mathrm{d}t \times \frac{1}{\sqrt{2\pi}}\int_{-\infty}^{\infty} h(t)\ e^{-\mathrm{i}\omega t}\,\mathrm{d}t \\ &= H(f)G(f)\end{aligned} \tag{2.8}$$

2.1.1.0.2 Correlation and Autocorrelation:

We can also define the *correlation* of two functions as:

$$\mathrm{Corr}(g,h) \equiv \int_{-\infty}^{\infty} g(\tau+t)h(\tau)\mathrm{d}\tau \tag{2.9}$$

And the Correlation Theorem as:

$$\frac{1}{\sqrt{2\pi}}\int_{-\infty}^{\infty}\mathrm{Corr}(g,h)\ e^{-\mathrm{i}\omega t}\,\mathrm{d}t = G(f)H(-f) \tag{2.10}$$

The correlation of a function $h(t)$ with itself is called *autocorrelation*. The Wiener-Khinchin theorems allow us to relate the autocorrelation of a function with the squared modulus of its Fourier transform:

$$\int_{-\infty}^{\infty}\mathrm{Corr}(h,h)\ e^{-\mathrm{i}\omega t}\,\mathrm{d}t = |H(f)|^2 \tag{2.11}$$

The convolution, correlation and autocorrelation are sketched in Figure 2.1. From this figure, one can see that a correlation determines the degree of similarity between two signals. If the signals are identical, then the correlation coefficient is 1; if they are totally different, the correlation coefficient is 0, and if they are identical except that the phase is

shifted by exactly 180º (i.e. mirrored), then the correlation coefficient is -1. When two independent signals are compared, the procedure is known as cross-correlation, and when the same signal is compared to phase shifted copies of itself, the procedure is known as autocorrelation (see `http://coral.lili.uni-bielefeld.de/Classes/Summer96/Acoustic/acoustic2/`).

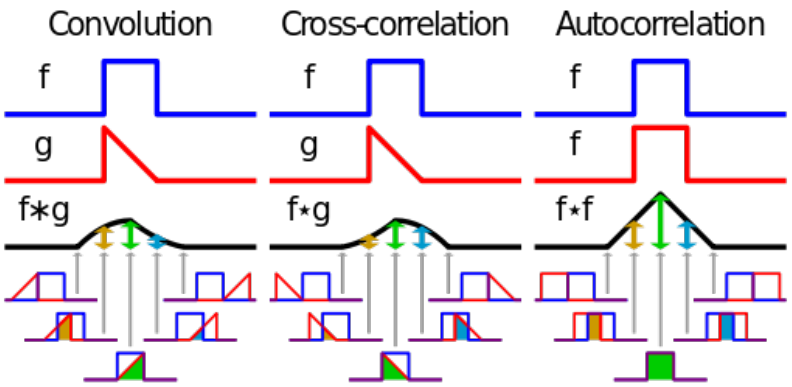

Figure 2.1: Sketchs of convolution (on the right), correlation or cross-correlation (at the center) and autocorrelation (on the left). Taken from `http://en.wikipedia.org/wiki/Convolution`.

We can define the *total power* of a signal which is the same quantity whether we compute it in the time domain or in the frequency domain. This result is known as the Parseval's Theorem.

$$\text{Total Power} = \int_{-\infty}^{\infty} |h(t)|^2 \, \mathrm{d}t = \int_{-\infty}^{\infty} |H(f)|^2 \, \mathrm{d}f \tag{2.12}$$

To know "how much power" is contained in the frequency interval between f and $f + \mathrm{d}f$, one does not usually distinguish between positive and negative frequency f, but rather regards f as varying from 0 ("zero frequency" or D.C.) to $+\infty$. Then, we define the one-sided power spectral density (PSD) of the function h as:

$$P_h(f) = |H(f)|^2 + |H(-f)|^2; \; 0 \leq f < +\infty \tag{2.13}$$

If $h(t)$ is a real function, the PSD becomes $P_h(f) = 2|H(f)|^2$. The total power is the integral of $P_h(f)$ from $f = 0$ to $f = +\infty$. The PSD can also be defined without the factor 2 and it is called two-sided power spectral density. We will continue using the one-sided PSD.

If the funtcion $h(t)$ goes endlessly from $-\infty < t < +\infty$, then both, the total power and

power spectral density will be, in general, infinite.

2.1.1.1 One-Sided Power Spectran Density per Unit Time

The one-sided PSD is computed by taking a long but finite stretch of the function $h(t)$, computing its PSD (that is, the PSD of a functions that equals $h(t)$ in the finite stretch but is zero everywhere else), and then dividing the resulting PSD by the length of the stretch used. In this case, Parseval's theorem states that the integral of the one-sided PSD-per-unit-time over positive frequency is equal to the mean square amplitude of the signal $h(t)$.

The PSD-per-unit-time converges to finite values at all frequencies except those where $h(t)$ has a discrete sine-wave (or cosine-wave) component of finite amplitude. At those frequencies it becomes a Dirac's delta-function, but whose area converges to be the mean square amplitude of the discrete sine (cosine) component at that frequency.

2.1.2 Fourier Transform of Discretely Sampled Data

In computational work, especially with experimental data, we are almost never given a continuous functions $h(t)$ to work with, but are given, rather, a list of measurements of $h(t_i)$ for a discrete set t_i's. The function $h(t)$ can be sampled at evenly spaced intervals in time. If Δ denotes the time interval between consecutive samples, so that the sequence of sampled values is:

$$h_n = h(n\Delta);\ n = ..., -3, -2, -1, 0, 1, 2, 3, ... \tag{2.14}$$

The reciprocal of the time interval is called the sampling rate. If Δ is measured in seconds ($[\Delta] = \text{s}$), then the sampling rate is the number of samples recorded per second.

2.1.2.1 Sampling Theorem and Aliasing

For any sampling interval Δ there is a critical frequency called Nyquist critical frequency, given by:

$$f_c = \frac{1}{2\Delta} \tag{2.15}$$

The Nyquist frequency is the highest frequency that can be coded at a given sampling rate in order to be able to reconstruct the signal. For example, critical sampling of a sine wave is two sample points per cycle, one at the positive peak and the other at the negative trough. It's frequent to choose to measure time in units of the sampling interval Δ. In this cases the Nyquist critical frequency is constant: $f_c = 1/2$. The Nyquist frequency is important for two related reasons, which we will discribe:

1. **Sampling Theorem:** If a continuous function $h(t)$, sampled at an interval Δ, happens to be bandwith limited to frequencies smaller in magnitude than f_c, i.e., if $H(f) = 0 \; \forall \; |f| \geq f_c$, then the function $h(t)$ is completely determined by its samples h_n:

$$h(t) = \Delta \sum_{n=-\infty}^{+\infty} h_n \frac{\sin\left[2\pi f_c(t - n\Delta)\right]}{\pi(t - n\Delta)} \tag{2.16}$$

   It is important to remark that the "information content" of a bandwith limited function is infinitely smaller than that of a general continuous function.

2. When one is sampling a continuous function that is not bandwith limited to less than the Nyquist critical frequency, it turns out that all of the power spectra density (PSD) that lies outside the frequency range $-f_c < f < f_c$ is spuriously moved into that range. This phenomenon is called aliasing. Any frequency component outside the frequency range $(-f_c, f_c)$ is aliased (falsely translated) into that range by the very act of discrete sampling. But the way to overcome aliasing is to: (i) know the natural bandwith limit of the signal or else enforce a known limit by analog filtering of the continuous signal, and then (ii) sample at a rate sufficiently rapid to give at least two points per cycle of the highest frequency present.

2.1.2.2 **Discrete Fourier Transform (DFT)**

We are going to estimate the Fourier transform of a function from a finite number of its sampled points. Let's suppose that we have N consecutive sampled values:

$$h_k = h(t_k); \; t_k = k\Delta; \; k = 0, 1, 2, ..., N - 1 \tag{2.17}$$

Where Δ is the sampling interval and we are going to suppose that N is even. If $h(t)$ is non-zero only in a finite interval of time, then that whole interval of time is supposed

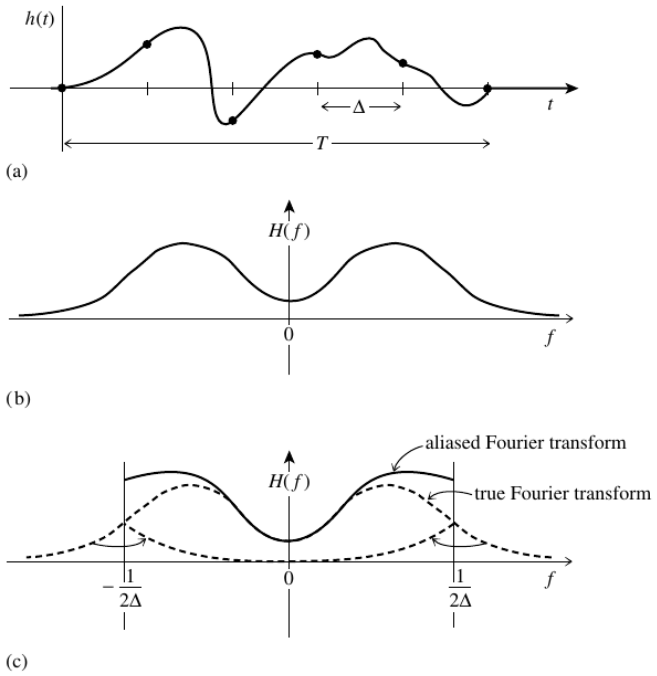

Figure 2.2: The continuous function shown in (a) is a nonzero only for a finite interval of time T. It follows that its Fourier transform, whose modulus is shown schematically in (b), is not bandwidth limited but has a finite amplitude for all frequencies. If the original function is sampled with a sampling interval Δ, as in (a), then the Fourier transform (c) is defined only between plus and minus the Nyquist critical frequency. Power outside that range is folded over or "aliased" into the range. The effect can be eliminated only by low-pass filtering the original function before sampling. Figure taken from [19].

to be contained in the range of N points given. If the function $h(t)$ goes on forever, then the sampled points are supposed to be at least "typical" of what $h(t)$ looks like at all over times.

With N inputs, we will be able to produce no more than N independent numbers of output. So, instead of trying to estimate the Fourier transform $H(f)$ at all values of f in the range $-f_c$ to f_c, let us seek estimates only at the discrete values.

$$f_n = \frac{n}{N\Delta};\ n = -\frac{N}{2}, ..., \frac{N}{2} \tag{2.18}$$

Extreme values of n correspond to the lower and upper limits of the Nyquist critical frequency range. In Equation 2.18 there are $N + 1$ values of n, but the extreme values of n are equal, reducing the count to N. Now, we have to approximate the integral in Equation 2.1 by a discrete sum:

$$
\begin{aligned}
H(f_n) &= \frac{1}{\sqrt{2\pi}} \int_{-\infty}^{+\infty} h(t)\, e^{-2\pi \mathrm{i} f_n t}\, \mathrm{d}t \approx \frac{1}{\sqrt{N}} \sum_{k=0}^{N-1} h_k\, e^{-2\pi \mathrm{i} f_n t} \Delta \\
&\approx \frac{\Delta}{\sqrt{N}} \sum_{k=0}^{N-1} h_k\, e^{-2\pi \mathrm{i} n k \Delta/(N\Delta)} \\
&\approx \frac{\Delta}{\sqrt{N}} \sum_{k=0}^{N-1} h_k\, e^{-2\pi \mathrm{i} n k/N}
\end{aligned} \tag{2.19}
$$

Where we have used both equations, Equation 2.17 and Equation 2.18. Equation 2.19 is called the Discrete Fourier Tranform (DFT) of the N points h_k. Denoting:

$$
H_n = \frac{1}{\sqrt{N}} \sum_{k=0}^{N-1} h_k\, e^{-2\pi \mathrm{i} n k/N} \tag{2.20}
$$

The DFT map N complex numbers h_k's into N complex numbers H_n's. The relation in Equation 2.19 between DFT of a set of numbers and their continuous Fourier transform when they are viewed as samples of a continuous functions sampled at an interval Δ can be rewritten as:

$$
H(f_n) \approx \Delta H_n \tag{2.21}
$$

With f_n given by Equation 2.18. We have taken the view that the index n in Equation 2.20 varies from $-N/2$ to $N/2$, as in Equation 2.18. However, Equation 2.20 is periodic in n, with period N. Therefore, we make use of the property $H_{-n} = H_n;\ n = 1, 2, ...$ One generally let the n in H_n vary from 0 to $N-1$, i.e., one complete period. Then, n and k (in h_k) vary exactly over the same range, so the mapping of the N numbers into N numbers is manifest. When this convention is followed, the zero frequency corresponds to $n = 0$; positive frequencies $0 < f < f_c$ correspond to values $1 \leq n \leq (N/2) - 1$, while negative frequencies $-f_c < f < 0$ correspond to $(N/2) + 1 \leq n \leq N - 1$. The value $n = N/2$ correspond to both $f = f_c$ and $f = -f_c$.

Discrete Fourier transform has symmetry properties almost exactly the same as the continuous Fourier transform. For example all the simetries in Table 2.1 hold if we read h_k for $h(t)$, H_n for $H(f)$, and H_{N-n} for $H(-f)$. Likewise, "even" and "odd" in time refer to whether the values h_k at k and $N - k$ are identical or the negative or each other. Table 2.2 show how are those simetries for the discrete case.

If	Then
h_k is real	$H_{N-n} = H_n^*$
h_k is imaginary	$H_{N-n} = -H_n^*$
$h_k = h_{N-k}$	$H_{N-n} = H_n$
$h_k = -h_{N-k}$ is odd	$H_{N-n} = -H_n$
h_k is real and $h_k = h_{N-k}$	H_n is real and $H_{N-n} = H_n$
h_k is real and $h_k = -h_{N-k}$	H_n is imaginary and $H_{N-n} = -H_n$
h_k is imaginary and $h_k = h_{N-k}$	H_n is imaginary and $H_{N-n} = H_n$
h_k is imaginary and $h_k = -h_{N-k}$	H_n is real and $H_{N-n} = -H_n$

Table 2.2: Symmetries of the Discrete Fourier transform

The formula for the discrete inverse Fourier transform, which recovers the set of h_k's exactly from H_n's is:

$$h_k = \frac{1}{\sqrt{N}} \sum_{n=0}^{N-1} H_n \, e^{2\pi i k n/N} \tag{2.22}$$

While the discrete form of the Parseval's theorems reads:

$$\sum_{k=0}^{N-1} |h_k|^2 = \sum_{n=0}^{N-1} |H_n|^2 \tag{2.23}$$

A routine for calculating DFT can also calculate the inverse transforms with a slight modification in the sign of the exponential.

2.2 Fast Fourier Transform (FFT) with FFTW C-Library

2.2.1 General Background

A Fast Fourier Transform (FFT) is a routine that computes a discrete Fourier transform (DFT). The computational cost of computing the N data points in the Fourier space via Equation 2.19 is $O(N^2)$, but the computational cost of a FFT is, in the best cases, of order $O(N \log_2 N)$ operations, and in the worst cases, the same as the previous one. Respect to computational time, a FFT works better when the number of data points N is a power of 2 and it works badly when N is a prime or it has as divisor big primes. In our computational work, we have used the version 3.3.3 of FFTW, or the *Fastes*

Fourier Transform in the West. FFTW is a comprehensive collection of fast C routines for computing the DFT and various special cases thereof.

FFTW does not use a fixed algorithm for computing the transform, but instead it adapts the DFT algorithm to details of the underlying hardware in order to maximize performance. Hence, the computation of the transform is split into two phases. First, FFTW's planner "learns" the fastest way to compute the transform in the machine. The planner produces a data structure called a *plan* that contains this information. Subsequently, the plan is executed to transform the array of input data as dictated by the plan. The plan can be reused as many times as needed. In typical high-performance applications, many transforms of the same size are computed and, consequently, a relatively expensive initialization of this sort is acceptable. On the other hand, if one need a single transform of a given size, the one-time cost of the planner becomes significant. For this case, FFTW provides fast planners based on heuristics or on previously computed plans [8].

2.2.1.1 What FFTW Computes

Here we present what FFTW computes and the conventions for the normalization and the sign of the complex exponent used by the FFTW library [8], [7].

2.2.1.1.1 The 1D Discrete Fourier Transform:

The forward DFT of a 1 dimensional (1D) complex input array h_k of size N computes an output array H_n, where:

$$H_n = \sum_{k=0}^{N-1} h_k e^{-2\pi \mathrm{i} kn/N} \tag{2.24}$$

It is denoted `FFTW_FORWARD` in the FFTW routine. The inverse DFT, denoted as `FFTW_BACKWARD`, of the input array h_k computes:

$$H_n = \sum_{k=0}^{N-1} h_k e^{2\pi \mathrm{i} kn/N} \tag{2.25}$$

FFTW computes an unnormalized transform, in that there is no coefficient in front of the summation in the DFT. In other words, applying the forward and then the backward

transform will multiply the input by N. From above, an `FFTW_FORWARD` transform corresponds to a sign of (-1) in the exponent of the DFT and `FFTW_BACKWARD` transform corresponds to a sign of $(+1)$. For ease, we only describe the relations for complex inputs, because it is the kind of inputs used in our implementation. For a detailed description for other methods of FFT, such as DFT of real input data, please see [8].

2.2.1.1.2 Multi-dimensional Transforms:

The multi-dimensional transforms of FFTW, in general, compute simple the separable product of the given 1D transform along each dimension of the array. Since each of these transforms is unnormalized, computing the forward followed by a backward/inverse multi-dimensional transform will result in the original input array scaled by the product of the normalization factors of each dimension, e.g. the product of the dimension sizes for a multi-dimensional DFT, which is our case.

Let's consider the following exact mathematical definition of our multi-dimensional DFT. Let h be a d-dimensional complex array whose elements are $h[k_1, k_2, ..., k_d]$ where $0 \leq k_s \leq N_s$ for all $s \in \{1, 2, ..., d\}$. Let also $\omega_s = e^{2\pi \mathrm{i}/N_s}$ for all $s \in \{1, 2, ..., d\}$. The forward transform computes a complex array H, whose structure is the same as that of h, defined by:

$$H[n_1, n_2, ..., n_d] = \sum_{k_1=0}^{N_1-1} \sum_{k_2=0}^{N_2-1} \cdots \sum_{k_d=0}^{N_d-1} h[k_1, k_2, ..., k_d] \omega_1^{-k_1 n_1} \omega_2^{-k_2 n_2} \cdots \omega_d^{-k_d n_d} \tag{2.26}$$

The backward transform computes

$$H[n_1, n_2, ..., n_d] = \sum_{k_1=0}^{N_1-1} \sum_{k_2=0}^{N_2-1} \cdots \sum_{k_d=0}^{N_d-1} h[k_1, k_2, ..., k_d] \omega_1^{k_1 n_1} \omega_2^{k_2 n_2} \cdots \omega_d^{k_d n_d} \tag{2.27}$$

Computing the forward transform followed by the backward transform will multiply the arrays by $\prod_{s=1}^{d} N_s$.

As in our work we need only 3D transforms, the forward or direct transform will be given by:

$$H[n_i, n_j, n_k] = \sum_{i=0}^{N_g-1} \sum_{j=0}^{N_g-1} \sum_{k=0}^{N_g-1} h[i,j,k] \omega_i^{-in_i} \omega_i^{-jn_j} \omega_k^{-kn_k} \tag{2.28}$$

Where $i,\ j,\ k$ represent the $x,\ y$ and z-axis, respectively, and $0 \leq i, j, k \leq N_g$, with N_g representing the number of data points in each axis, which in our case, is the same for all directions; $n_i,\ n_j,\ n_k$ represent the reciprocal points of $i,\ j,\ k$, and varying as $0 \leq n_i, n_j, n_k \leq N_g$. As N_g is the same for all directions, the factors $\omega_i,\ \omega_j,\ \omega_k$ are the same and equal to $e^{2\pi \mathrm{i}/N_g}$. Then, we will have one value of H for a triad (n_i, n_j, n_k). Finally, the backward or inverse transform will be given by:

$$H[n_i, n_j, n_k] = \sum_{i=0}^{N_g-1} \sum_{j=0}^{N_g-1} \sum_{k=0}^{N_g-1} h[i,j,k] \omega_i^{in_i} \omega_i^{jn_j} \omega_k^{kn_k} \tag{2.29}$$

2.3 Fourier Analysis of the Density Field

In this section we are going to describe the analitical processes to obtain the density field, the potential and its time derivative in a general way. Also we are going to explain the numerical and computational methods used to calculate these quantities for our data and a brief explanation about the use of the FFTW library.

2.3.1 Nearest Grid-Point Algorithm

The Nearest Grid Point (NGP) algorithm was briefly described in subsection 1.6.2 in the PM code. Here, we will describe the NGP algorithm in our work.

As seen in subsection 1.6.2, the NGP algorithm is one of the schemes to assign the mass of a simulation mesh. We have used the results of a N-body simulation with the GADGET code[1]. This simulation gives as result a serie of snapshots for different redshift z, with the proper positions and peculiar velocities of the particles in a cubic box of $400h^{-1}$ Mpc size ,i.e., a volume of $400^3 h^{-3}$ Mpc^3, and a total number of particles equal to 512^3. Each particle has a mass of 3.41454×10^{10} M$_\odot$. In this simulation, periodic boundary conditions were used. Those and other characteristics of the simulation are given in Table 2.3.

[1]The results of this simulation were provided by my advisor Juan Carlos Muñoz Cuartas.

Quantity	Value
Box size L	$400h^{-1}$ Mpc
$\Omega_{m,0}$	0.258
$\Omega_{\Lambda,0}$	0.742
Hubble's parameter h	0.72
Hubble's constant at present time H_0	$100h\ \frac{1}{\text{s}}$
Total number of particles	512^3
Mass unit	$1 \times 10^{10} h^{-1}$ $\text{M}_\odot$
Particle mass	$3.41454 \times$ Mass unit
Mean matter density $\overline{\rho}$	$7.160809 \times 10^{10} h^{-2}$ $\text{M}_\odot\text{Mpc}^{-3}$
Lenght unit	$1h^{-1}$ Mpc
Gravitational constant G in the internal units	43.0071

Table 2.3: Information of the N-body simulation used.

To read the results from the N-body simulation, it is necessary to read from a binary format which GADGET uses to save the data files. As those files have an approximate size of 4 - 5 GB, it is necesary to use the MPI library in order to read the data with more than one CPU and make a more efficient use of the computing time[1]. Once the positions and velocities of each particle was read from the GADGET file, we recalculate the size of the cubic box and create a grid with the same number of cells per axis. The number of cells per axis N_g depends on the desired resolution; we have used tree different values for N_g: 64, 128 and 256. A better resolution $N_g = 512$ was desired, but the computational power and time needed is too high, and a resolution of $N_g = 256$ is enough to visualize the SW effect; better resolution would allow to visualize higher-order anisotropies such as the Rees-Sciama effect. This last effect is not of our interest, but we have used some methods and relations obtained by [4] and [20] whom have studied the Rees-Sciama effect, to find important physical quantities as the gravitational potential and its time derivative.

First, a grid must be constructed. We assign a certain position (x, y, z) to each cell, that will be the central point of the cell, i.e., if a cell is placed between $(x_{\text{min}}, y_{\text{min}}, z_{\text{min}})$ and $(x_{\text{max}}, y_{\text{max}}, z_{\text{max}})$, the cell point which charaterizes this cell will

[1]Even reading those files in 30 CPU's, the results that we need can be obtained over a week later. As we will show, we used three different resolutions. The with the lowest resolution, the computing time is about one day, the next high resolution takes over 3 days to be read and the best resolution takes approximately one week or more. Then, reading such files with only one CPU could take even months.

be $(x_{\text{cm}} = (x_{\text{min}} + x_{\text{max}})/2, y_{\text{cm}} = (y_{\text{min}} + y_{\text{max}})/2, z_{\text{cm}} = (z_{\text{min}} + z_{\text{max}})/2)$, and $x_{\text{max}} = x_{\text{min}} + \Delta x$, being Δx the cell size and x_{cm} the position in the x-axis of the center of the cell and so on. All this values are stored for a future use.

Once the grid is constructed and the grid points located, we proceed to fill the grid with the particles and assign them to each cell. To see how it works, let's see an example: we read the position in each direction of a certain particle: x_p, y_p, z_p; then, we first take the component x_p and see if this value is between the stored positions x_{min} and x_{max} of a certain cell. We do the same for the y and z components in this order. If the particle is inside the cell, then its mass is assigned to the cell and stored in memory. The velocities of the particles in each direction are also assigned to the cell in order compute the center of mass velocity of the cell. When another particle is inside the same cell, its mass is also assigned to this cell, and the total mass of the cell increases in this value, i.e., the mass of this last particle is added mathematically to the mass stored in this cell. The velocity of the center of mass is computed as the average velocity of all the particles in the cell, and in each direction.

When this step is ready for all the particles, the volume of each cell is calculated. This is made only one time, because all cells have the same sizes along each axis and then, the same volume. With this value of volume and with the total mass enclosed in each cell, it is easy to calculate the density of each cell and store this value, or even, calculate directly the density contrast $\Delta(\mathbf{r})$ in the respective cell and store this last value. It is important to emphazise that the particles have an ID to identify each one from the other ones. The order to assign the ID to each particle is the same order of reading from the GADGET file for each particle; this ID is stored for a future use. This is the NGP algorithm implemented in our study. Let's summarize this explanation in the flow chart given in Figure 2.3.

2.3.2 Grid Construction

Here, we are going to explain in a more detailed way the construction and filling of the grid in a computational point of view. It is clear that we are using the programming language C, and we will give our explanation based on it.

When we constructed the grid, we used three `for` cycles. The first `for` is for the z axis and is characterized by the index `k`. The second `for` is for the y axis and is

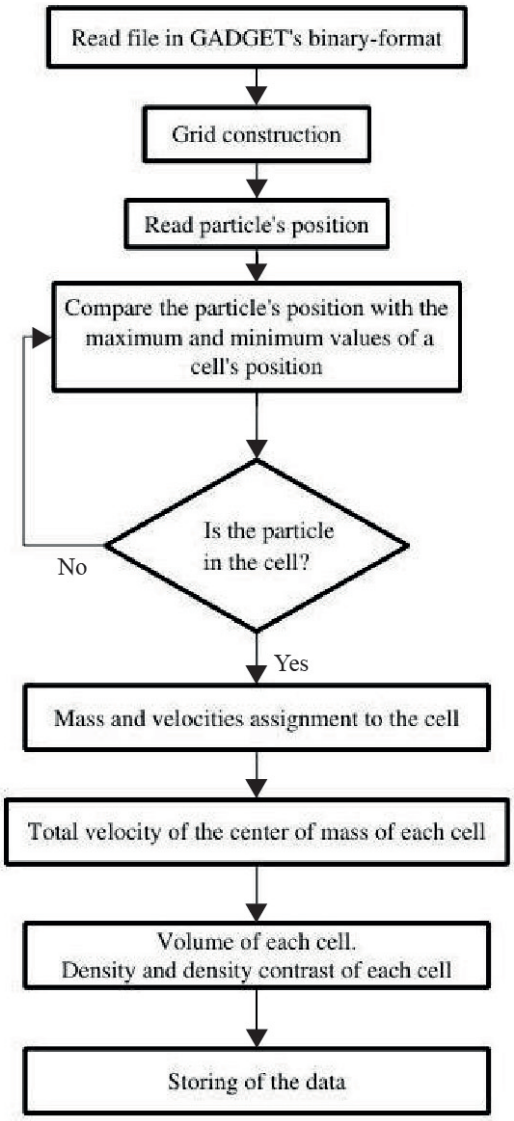

Figure 2.3: Flow chart sumarizing the creation and filling of the grid.

characterized by the index `j` and the last `for` cycle is for the x axis and is characterized by the index `i`. All indices of the `for` cycles go from zero to the number of cells N_g, that means $0 \leq$ `i, j, k` $< N_g$, for $N_g = 64, 128, 256$.
Now, we define a cell size which will be equal to the ratio between the size of one axis of the simulation box, $L = 400$ Mpch^{-1}, and the number of grid cells in one axis, N_g, i.e.:

$$\text{Cell Size} = \frac{L}{N_g} \tag{2.30}$$

This step can be understood as taking a plane for fixed z, then, a line for fixed y in

this plane, and in this line we place the points for all the x values; then, we do the same for the following value of y, and so on until the fixed plane z is constructed. We pass to the next value of z and do the same until all the grid with shape of a cubic box is created. Finally, an ID (henceforth GP_ID) is given to each cell in the order of construction. In this order, a simple relation can be found for the value of GP_ID. For simplicity in our codes, the GP_ID is called m.

$$\text{GP\_ID} = m = (kn_y + j)n_x + i \tag{2.31}$$

Where n_x, n_y are the number of cells in the x and y-axis, respectively, and both are equal to N_g, i.e., $n_x = n_y = N_g$. And i, j, k are the indices used in the `for` cycles previously described for the x, y and z axis, respectively. That means, the GP_ID is given by the order of construction of the grid and the respectively position of the cell.
Once the grid is constructed as explained, the grid is filled with the particles, as described in subsection 2.3.1. Figure 2.4 shows how this grid has been constructed. From this figure, it is possible to see a sketch of a plane for fixed value of $z = 0.0$ and in this plane, different values of y, which indicates different lines. Along each of these lines, we put the values of x which will define the maximum and minimum values (x_{min} and x_{max}, respectively) of each cell. With this two values we calculate the position of the center of the cell in the x-axis. In this diagram is easy to see how for the values of the indices $i = j = k = 0$ we obtain an ID $m = 0$ for the first cell. For $j = k = 0$ and $i = 1$ we obtain the ID $m = 1$ for the second cell and so on. When the iterations in the x-axis finish, we pass to the next value of $j = 1$ and perform the same steps. With this value of j the first cell in this line will have indices $i = k = 0$ and $j = 1$, and its ID will be $m = ((0)n_y + 1)n_x + 0 = n_x = N_g$. The second cell has indices $i = j = 1$ and $k = 0$, then its ID will be $m = N_g + 1$.

It is important to take into account that the order used in the FFTW library to construct a discrete grid is different from the order used by us, because we need to pass the data ordered with ID m to the default order of the FFTW, which we are going to show sooner. As seen previously, a numerical Fourier transform must be performed with discrete values, that's the reason why we need to construct another grid in which will be stored the information read before the construction of the grids from the GADGET file. This new grid should be constructed taking first a plane for fixed x, then we take a fixed y and put finally all the values of z in this line y. Then, we pass to another fixed value of y and do

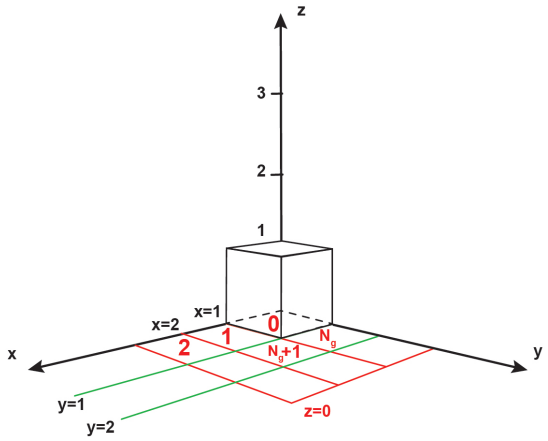

Figure 2.4: Sketch of the grid construction for the reading of particle's position from the GADGET file. The ID's of the cells are given by the relation $m = (kn_y + j)n_x + i$. This relation tell us that the most rapidly varying index is i (representing the $x - axis$), while the slowest varying index is k (which represents the z-axis).

the same until all the x plane is filled. Finally, passing to another x coordinate, we construct the new grid. This is performed with the help of `for` cycles, as the previously grid, but beginning with a `for` in the index `i`, representing the x-axis, later a `for` cycle in `j` representing the y-axis and finally a `for` in `k`, which represents the z-axis. This means that the most rapidly varying index is `k` and the slowest varying index is `i`. In this new grid, the ID of each cell changes. We find that the correct way to assign and ID, called p to the cells if the grid is constructed in this last way is the following:

$$p = (in_y + j)n_z + k \tag{2.32}$$

Where i, j, k represent the indices of the `for` cycles for the x, y and z-axis respectively and n_y, n_z are the number of cells in the y and z-axis, respectively. As before, $n_y = n_z = N_g$. Given this situation, we need to identify the two different ID's that characterizes the same cell in both grids when we perform a FFT. In both grids, a cell will have the same coordinates (i, j, k), but the ID's will be given by Equation 2.31 and Equation 2.32, then we perfom a transform between both ID's identification. Figure 2.5 shows the grid construction with the described method for the FFTW. In this figure is possible to see again the assignation of the ID of the cells. as follows: in a plane for fixed value of $x = 0$ it is possible to see in this plane, different values of y, which indicates different lines. Along each of these lines, one put the values of z which will define the

maximum and minimum values (z_{min} and z_{max}, respectively) of each cell. With this two values we calculate the position of the center of the cell in the z-axis. In this diagram is easy to see how for the values of the indices $i = j = k = 0$ we obtain an ID $p = 0$ for the first cell. For $i = j = 0$ and $k = 1$ we obtain the ID $p = 1$ for the second cell and so on. When the iterations in the z-axis finish, we pass to the next value of $j = 1$ and perform the same steps. With this value of j the first cell in this line will have indices $i = k = 0$ and $j = 1$, and its ID will be $p = ((0)n_y + 1)n_z + 0 = n_z = N_g$. The second cell has indices $j = k = 1$ and $i = 0$, then its ID will be $m = N_g + 1$.

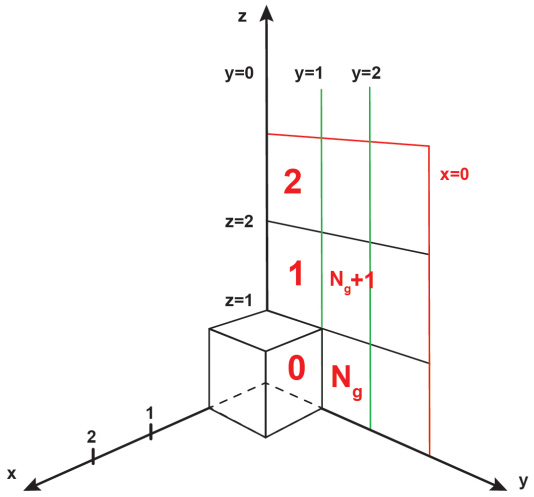

Figure 2.5: Sketch of the grid construction for the sorting of data input for the FFTW library. The ID's assignment follows the relation: $p = (in_y + j)n_z + k$. This relation tell us that the most rapidly varying index is k (representing the $z - axis$), while the slowest varying index is i (which represents the x-axis).

2.3.3 Density Fluctuation Fields $\Delta(\mathbf{r})$ and $\Delta(\mathbf{k})$

In order to obtain the fluctuation density field numerically, we need to compute the density contrast (Equation 1.51). Let's remember its definition:

$$\Delta(x) = \frac{\rho(x) - \overline{\rho}}{\overline{\rho}} \tag{2.33}$$

With the density contrast computed in the real space $\Delta(\mathbf{r})$, we performed a Fourier transform to find the density contrast in the Fourier space $\Delta(\mathbf{k})$, known also as the reciprocal space or the k-space. In order to estimate $\Delta(\mathbf{k})$ correctly, first it was calculated the Fourier transform of $\Delta(\mathbf{r})$, called $\Delta_g(\mathbf{k})$, and each resulting mode was corrected with the mass-assignment windows function. For the NGP algorithm which is the one used in our implementation, this corresponds to:

$$\Delta_d(\mathbf{k}) = \Delta_g(\mathbf{k})/W_{\text{NGP}}(\mathbf{k}) \tag{2.34}$$

Where:

$$W_{\text{NGP}} = \prod_{i=1,2,3} \left\{ \frac{\sin\left[\pi k_i/(2k_{\text{Ny}})\right]}{\left[\pi k_i/(2k_{\text{Ny}})\right]} \right\} \tag{2.35}$$

The subscript d and g denote discrete and grid quantities, and $k_{\text{Ny}} = \pi N_g/L$ is the Nyquist frequency, and N_g is the number of grid cells.

To obtain the density fluctuation field $\Delta(\mathbf{r})$ of each cell, we need to compute Equation 2.33 with the data after the NGP algorithm. The process to find the density contrast is the same for all snapshots, regardless the redshift z.

When the grid is finally constructed, we used the Nearest Grid-Point (NGP) method described in subsection 2.3.1 to calculate the mass enclosed in each cell, and with the volume of the cell, we calculate the density contained in the cells. With this last quantity computed, we can obtain the density contrast (Equation 2.33). The mean density of the Universe $\overline{\rho}$ is easily calculated and is the same regardless the value of N_g: $\overline{\rho} = Nm/V$, where N is the number of particles, m is the mass of each particle and V is the total volume of the simulation box.

With the density contrast assigned to each cell, and with the ID calculated from Equation 2.31 is easy to identify all the data from each cell: position, velocity of the center of mass and density contrast. We are ready to calculate the density contrast in the Fourier space: $\Delta_g(\mathbf{k})$. Recalling that the FFTW library has its own order given by Equation 2.32, we need to make a correct assignment of the density contrast to the new grid in order to calculate its Fourier transform.

The way to store all data from the grid points is through a data structure. A structure (or `struct` in C syntax), is a complex data type declaration that defines a physically grouped list of variables to be placed under one name in a block of memory, allowing the differente variables to be accessed via a single pointer, or the struct declared name which returns the same address (see `http://en.wikipedia.org/wiki/Struct_(C_programming_language)`).
With this in mind, we can make a pseudocode in order to understand the assignment of the density contrast to the input array of the FFTW.

First, we need to declare and create the arrays that correspond to the input and output of the FFT. Despite the density contrast $\Delta(\mathbf{r})$ is a real quantity, we used a complex to complex transform, that means, we supposed that both input and output arrays are composed by complex numbers. Obviously the imaginary part of the input array is set to be zero. We choose to make complex to complex transforms because the easiness in the interpretation and extraction of data from the output array. If the transforms are made for real input, the output array will have some symmetry properties which must be very well understood in order to extract the correct output element, a very complicated process for inexperienced people whom uses the FFTW library by first time. It should be also considered that the manual of the FFTW library is not very explicit and is not easy to understand and find some important properties needed in the computational area. That's a reason for us to be as explicit as possible in show, at least, how to make the complex to complex transform and compute properties of the reciprocal grid, such as the wavevector components. Back to what concern us, creation of the input and output arrays for the FFT in C is made as follows:

```
fftw_complex *in=NULL;
fftw_complex *in2=NULL;
fftw_complex *out=NULL;
```

The arrays declared here are of type `fftw_complex` which is by default an array of two elements of double precision: `double[2]` composed of a real (`in[i][0]`) and imaginary (`in[i][1]`) parts of a complex number. Here we define the input array `in[][]`, the output array `out[][]` and a final array `in2[][]` which will be the output of the inverse FFT (the input array of an inverse FFT is `out[][]`). This array `in2[][]` is used to compare with `in[][]` in order to verify that the FFT's have been

correctly performed.

The next step is to declare and create the `plan` used by FFTW. A plan is an object that contains all the data that FFTW needs to compute the FFT.

```
fftw_plan plan_r2k;
fftw_plan plan_k2r;
```

Where `plan_r2k` refers to a forward FFT, i.e., with a -1 sign in the exponential and `plan_k2r` refers to the inverse FFT, with a sign +1 in the exponential.
Once the arrays and the plans are declarated, we need to allocate memory for the arrays. For such step FFTW has its own way to allocate memory with the function `fftw_malloc`, which behaves like `malloc` of C, but is more recomended. Such allocation is made as follows:

```
in = (fftw_complex *) fftw_malloc( sizeof( fftw_complex )
                                   *nx*ny*nz );
out = (fftw_complex *) fftw_malloc( sizeof( fftw_complex )
                                    *nx*ny*nz );
```

Where `nx`, `ny`, `nz` must have been declarated before and equal to N_g. Now, with the memory allocated, we can begin to sort the density contrast array from the first grid order m, to the FFTW order p. Taking into account the order of the FFTW, we need to perform first a `for` cycle in `i` (representing the x-axis), second a `for` cycle in `j` (representing the y-axis) and finally a `for` cycle in `k` (representing the z-axis), as shown in the following pseudocode:

```
nx = ny = nz = Number of grid cells

for (i=0; i<nx; i++)
  {
    for (j=0; j<ny; j++)
      {
        for (k=0; k<nx; k++)
          {
            p = (i * ny + j) * nz + k;
```

```
            m = (k * ny + j) * nx + i;

            in[p][0] = Density_Contrast_of_cell_[m];
            in[p][1] = 0.0
          }
      }
  }
```

Now that the input array is in memory, we need to give to the plans declarated the respective inputs in order to perform the FFT. A plan needs as inputs the dimension (or dimensions if the FFT is of dimensions higher than 1), the input array which will be transformed, the ouput array in which the transformed data will be stored, the sign of the transform indicating if it will be a forward (-1) transform of backward (or inverse with sign +1) transform, and finally a flag. As an example, for one dimension:

```
fftw_plan fftw_plan_dft_1d(int n, fftw_complex *in,
                           fftw_complex *out, int sign,
                           unsigned flags);
```

Here the dimension is given by an integer `n`, the input array `in[][]` is declared as a `fftw_complex` number, as seen before and the same for the output array called `out[][]`. The integer `sign` depends if the transform is forward or backward. One can put this flag either -1 or `FFTW_FORWARD` for a forward transform or either +1 or `FFTW_BACKWARD` for a backward or inverse transform. Respect to the `unsigned flags`, this argument is usually either `FFTW_MEASURE` or `FFTW_ESTIMATE`. `FFTW_MEASURE` instructs FFTW to run and measure the execution time of several FFTs in order to find the best way to compute the transform of size `n`. `FFTW_ESTIMATE`, on the contraty, does not run any computation and just builds a reasonable plan that is probably sub-optimal. In our case, as our transforms are performed over a cubic grid, we need to compute a 3D complex-to-complex transform, which we define as follows:

```
planr2k = fftw_plan_dft_3d(nx, ny, nz, in, out,
                           FFTW_FORWARD,
                           FFTW_ESTIMATE);
```

The FFTW library has several routines to define a plan. It has a complex 1D DFT given by the plan `fftw_plan_dft_1d`, a 2D and 3D complex DFT given by `fftw_plan_dft_2d` and `fftw_plan_dft_3d` and a general dimensional complex DFT given by:

```
fftw_plan_dft(int rank, const int *n, fftw_complex *in,
              fftw_complex *out, int sign, unsigned flags);
```

The first entry `rank` refers to the number of dimensions or independent indices in the array; for example, in our case is 3, because we have a cubic box. The second entry `n` refers to an array with the same dimension of the input array, but each element in the array `n` has the number of elements (or cells) in each dimension. For example, we have to make a DFT for our data in 3 dimensions, each dimension having n_x, n_y and n_z elements. In this case we will suppose that the number of elements is equal $n_x = n_y = n_z = N_g = 64$, then the inputs will be:

```
int rank = 3;
double n[3];
n[0] = nx = 64;
n[1] = ny = 64;
n[2] = nz = 64;
```

For a real-to-complex and complex-to-real transforms, FFTW also has specific routines for 1D, 2D and 3D arrays and a general routine for any dimension. For more information concerning plans, please see [8], which, at least, is one of the most detailed sections in the manual of the library. With the plan created, we perform the FFT with the help of:

```
fftw_execute( plan_r2k );
```

With these steps, the DFT from the position space to the Fourier space is ready. If we want to visualize or store the correct output array, we need apply a normalization to the output array from the FFTW, that means, in our case:

```
norm = sqrt(nx * ny * nz);

for( p=0; p<(nx * ny * nz); p++ )
  {
    Real part in k space = out[p][0] / norm;
    Imaginary part in k space = out[p][1] / norm;
  }
```

The results of the DFT are stored in-order in the array `out[][]`, with the zero-frequency (DC) component in `out[0]` in the case of a 1D complex-to-complex DFT. In the case of a real-to-complex DFT, the data are stored in a different way which is more complicated to deal with it, because some symmetry properties must be taken into account in order to extract all the elements of the outputs to work with them. We recomend to better use a complex-to-complex transform with imaginary parts of the elements in the input array equal to zero and work with the respective output, as has been done by us in this work. In order to verify if the DFT was performed correctly, we apply an inverse Fourier transform to the output array `out[p][0]`, `out[p][1]` (without normalization). First, we allocate in memory the array `in2[][]` and perform another plan:

```
in2 = (fftw_complex*)malloc(sizeof(fftw_complex)*nx*ny*nz);

plan_k2r = fftw_plan_dft_3d( nx, ny, nz, out, in2,
                             FFTW_BACKWARD, FFTW_ESTIMATE);

fftw_execute(plan_k2r);
```

We can see that the input array of the inverse Fourier transfom performed with the plan `plan_k2r` is the output array `out[][]` from the first Fourier transform performed with `plan_r2k`, and the output array of `plank2r` should be the non-normalized input array. To visualize these new results and compare them with the initial input array `in[][]`, we need to apply a normalization to `in2[][]`. Remembering that the FFTW doesn't perform normalized FFT's, we need to divide the array `in2[][]` by $n_x n_y n_z$ and then we should obtain the first input array `in[][]`.

With all of this, once the arrays `in[][]` and `in2[][]` are compared and verified its equality, we can now calculate the wave vectors in the reciprocal grid. After an extensive search in order to know the correct expression for the wave vectors in a discrete

grid in the same order of the output of the FFTW, we found that the FFTW order in the ouputs enforce the wave vector components to be calculated with the following relations, in which must be taken into account that since each grid point has coordinates (x, y, z), then, the wave vector components (k_x, k_y, k_z), are the positions of the reciprocal grid given by (see `http://pauli.uni-muenster.de/tp/fileadmin/lehre/NumMethoden/SoSe10/Skript/Ordening.pdf`):

$$k_j(i) = \begin{cases} \frac{2\pi}{L} i & \text{if } i = 0, ..., \frac{N}{2} \\ \frac{2\pi}{L}(-N + i) & \text{if } i = \frac{N}{2} + 1, ..., N - 1 \end{cases} \; ; \; j = x, y, z \tag{2.36}$$

Finally, the expression of Equation 2.34 will be used to calculate the gravitational potential and the time derivative of the potential, processes that we will describe in the following sections. Before those steps, we can obtain the maps of the density fluctuation from the input of the FFT. Here, we present some slices of thickness $10h^{-1}$ Mpc for the three different values of $N_g = 64, 128, 256$.

From Figure 2.6, Figure 2.7 and Figure 2.8, we can see that effectively the grid with $N_g = 256$ has the best resolution of all. Then, henceforth we will show and analyse the results coming from the grid with this last resolution. In those mentioned figures we can see some regions which can be interpreted as vacuum regions (regions in blue) which means that the matter density here is too low or even null. As we are measuring density contrast we can interpret those blue regions as regions in which the density of the Universe is below the mean density of the Universe. This mean density is given by the white regions on the figures, meanwhile the pink and red regions are those regions in which the density is above the mean density of the Universe, given place to structures of dark matter haloes in which baryonic density could merge and form galaxies and clusters. Those figures will be better understood when they will be compared with the gravitational potential maps in Figure 2.9 and the time derivative of the potential in Figure 2.10.

2.3.4 Solution to Poisson Equation for $\Phi(\mathbf{r})$ and $\Phi(\mathbf{k})$

To solve the Poisson equation (Equation 1.57) in the Fourier space, we need to write it in comoving coordinates:

$$\nabla_x^2 \delta\Phi(\mathrm{x}, t) = 4\pi G a^2(t) \delta\rho \tag{2.37}$$

Where ∇_x^2 denotes the laplacian operator in comoving coordinates. With $\delta\rho = \Delta(\mathrm{x}, t)\overline{\rho}(t)$, the last equation becomes:

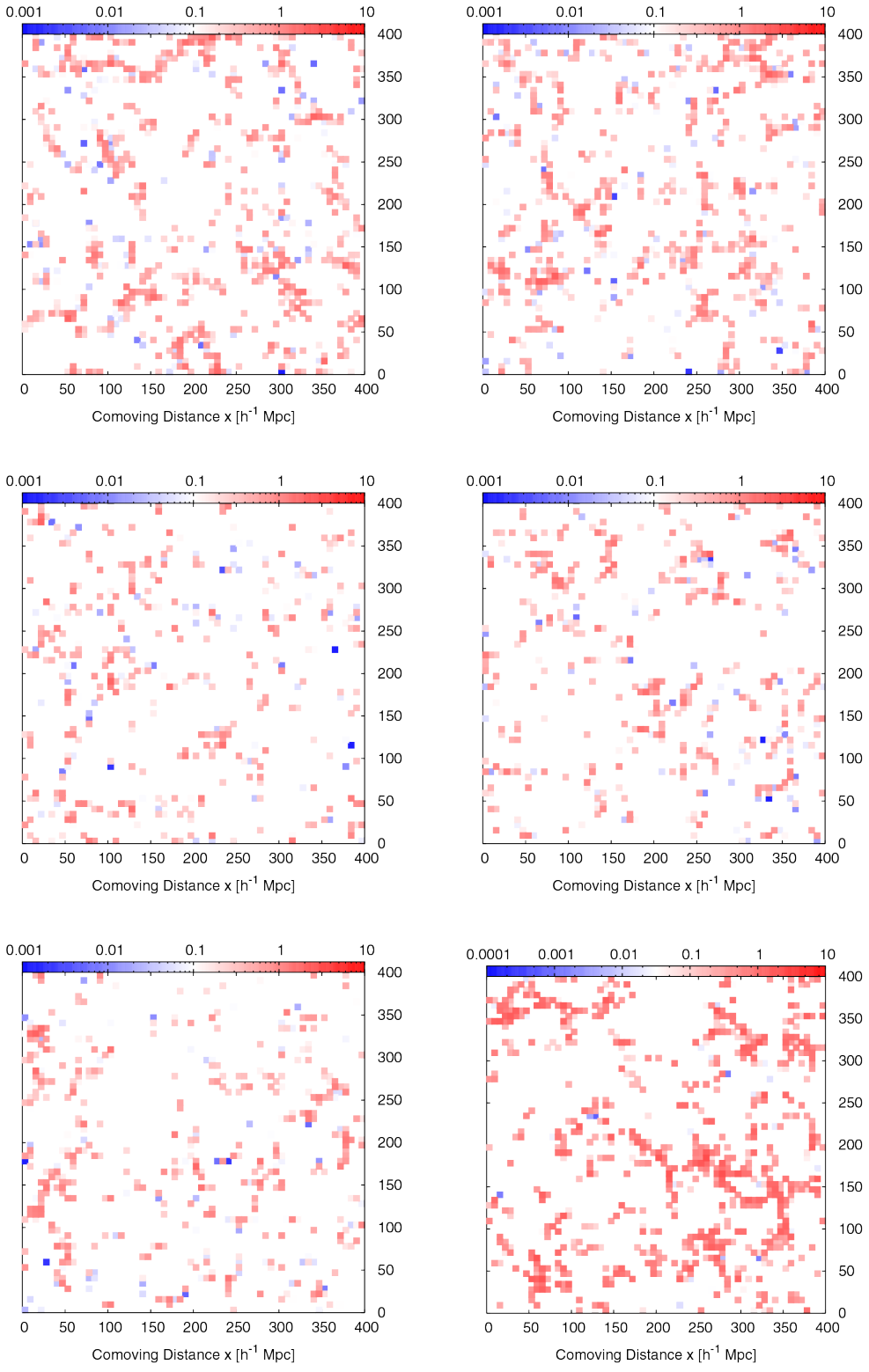

Figure 2.6: Density contrast $\Delta(\mathbf{r})$ for different slices of thickness $10h^{-1}$Mpc. This slices were calculated with $N_g = 64$ for redshift $z = 0.0$.

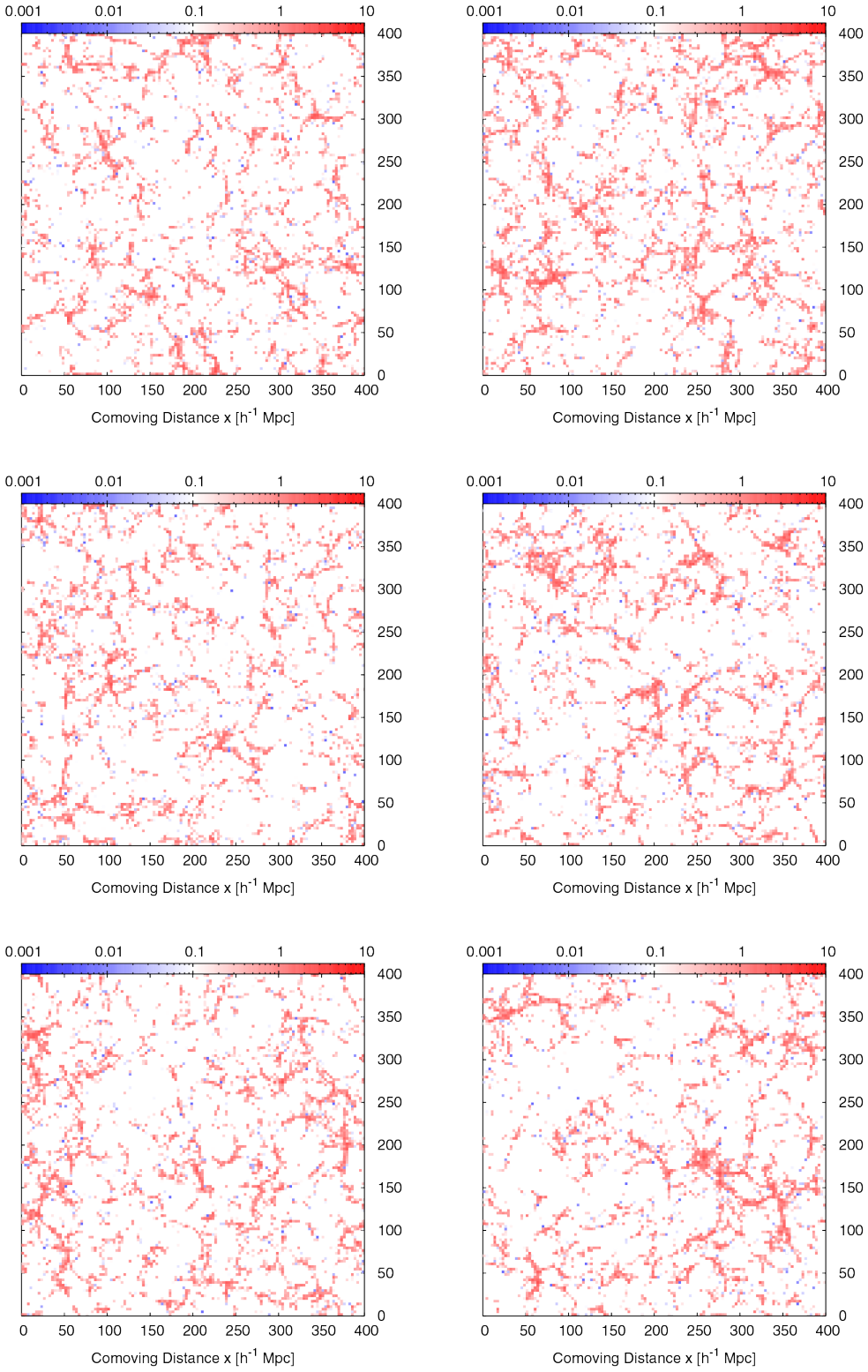

Figure 2.7: Density contrast $\Delta(\mathbf{r})$ for different slices of thickness $10h^{-1}$Mpc. This slices were calculated with $N_g = 128$ for redshift $z = 0.0$. These slices correpond to the same maps of Figure 2.6 with a better resolution.

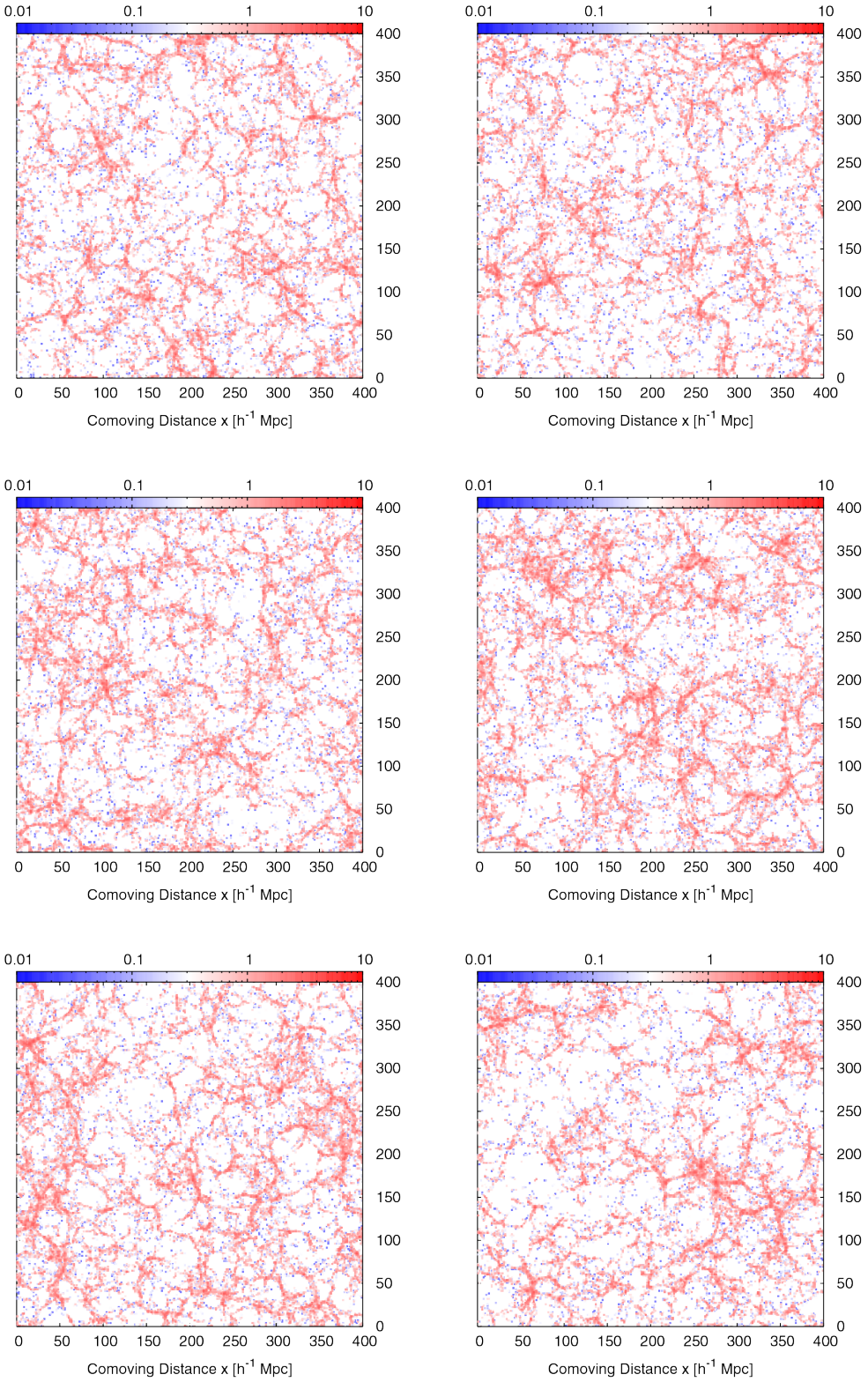

Figure 2.8: Density contrast $\Delta(\mathbf{r})$ for different slices of thickness $10h^{-1}$Mpc. This slices were calculated with $N_g = 256$ for redshift $z = 0.0$. These slices correpond to the same maps of Figure 2.6 with the best resolution.

$$\nabla_x^2 \delta\Phi(\mathrm{x}, t) = 4\pi G a^2(t)\overline{\rho}(t)\Delta(\mathrm{x}, t) \tag{2.38}$$

Making a Fourier transform with our sign convention, in order to solve this equation, we can simply change $\nabla_x \to \mathrm{i}k$, then $\nabla_x^2 = \nabla_x \cdot \nabla_x = -k^2$, and find that:

$$\begin{aligned} -k^2\delta\Phi(\mathrm{k}, t) &= 4\pi G a^2(t)\overline{\rho}(t)\Delta(\mathrm{k}, t) \\ \delta\Phi(\mathrm{k}, t) &= -4\pi G a^2(t)\overline{\rho}(t)\frac{\Delta(\mathrm{k}, t)}{k^2} \end{aligned} \tag{2.39}$$

Finally, the gravitational potential in the Fourier space is calculated computationally with the help of Equation 2.39, where in the expression for $\Delta(\mathrm{k}, t)$ was used $\Delta_d(\mathrm{k}, t)$ from Equation 2.34. This gravitational potential in the Fourier space will be used to find the time derivative of the potential. Before this step, we made an inverse FFT in order to compute the values of the gravitational potential in the position-space using the library FFTW, as explained in the preceding subsection 2.3.3. With the results from this inverse FFT, we plotted the respective potential maps in slices of thickness 10 Mpch^{-1} for the three different values of $N_g = 64, 128, 256$. We compare the density fluctuation maps with the potential maps to find a correspondence.

We can see the maps of the gravitational potential for different slices in Figure 2.9, were we have used $N_g = 256$ due to the improved resolution offered. In those maps, blue regions are related with a deeper potential, that means, more negative values of Φ In those blue regions we expect a correspondence with the respective density contrast map, i.e., a deeper potential will be related with a high value of the density contrast, which means that a great amount of matter will be accumulated in a deep potential. White regions in the gravitational potential maps are regions in which the potential is neither deep nor elevated and can be related with regions in which the density contrast has small values near to zero and the density is the same as the mean density of the Universe. Finally, red regions of the potential maps are related with positive values of Φ and can be thought not as a well but as a mountain. In those red regions the density contrast is very low or even negative, indicating that the density in these regions is below the value of the mean density of the Universe. Comparing these pictures with the respective ones on Figure 2.8 we can see that it is an evident correspondence and our conclusions are correct.

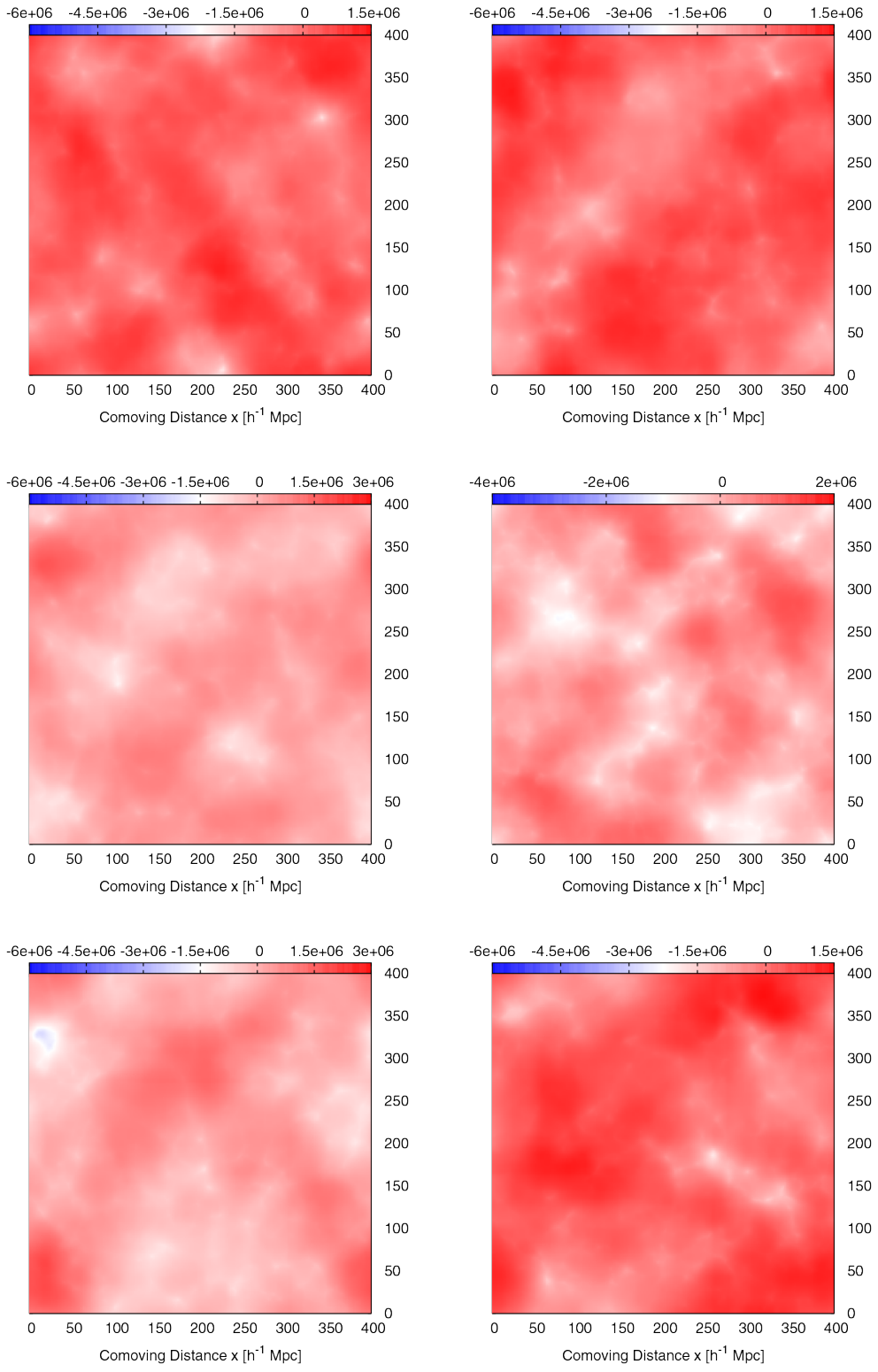

Figure 2.9: Gravitational potential $\Phi(\mathbf{r})$ for different slices of thickness $10h^{-1}$Mpc. This slices were calculated with $N_g = 256$ for redshift $z = 0.0$. From left to right and top to bottom, these maps are the respective potential maps for each of the density contrast maps shown in Figure 2.8, i.e., the upper left potential map corresponds to the upper left density map in Figure 2.8, the upper right potential map corresponds to the upper right density map, and so on. Φ is given in km^{2}s^{-2}.

2.3.5 Time Derivative of Potential $\dot{\Phi}(\mathbf{r})$ and $\dot{\Phi}(\mathbf{k})$

We are really interested in the instantaneous temporal rate of change of the potential. For this reason, we are going to differentiate Equation 2.39 respect to time. Before that, let's multiply and divide this equation by the scale factor $a(t)$, and taking into account that $\overline{\rho}(t)a^3(t)$ is a time independent quantity, we obtain:

$$\delta\dot{\Phi}(\mathbf{k},t) = -\frac{4\pi G}{k^2}\left[\overline{\rho}a^3(t)\right]\frac{\partial}{\partial t}\left[\frac{\Delta(\mathbf{k},t)}{a(t)}\right] \tag{2.40}$$

Taking into account that the Hubble's parameter is related with the scale factor by $H(t) = a^{-1}\dot{a}$, we can easily make the derivative in Equation 2.40 to obtain:

$$\delta\dot{\Phi}(\mathbf{k},t) = \frac{4\pi G}{k^2}\left[\overline{\rho}a^3(t)\right]\left[\frac{\Delta(\mathbf{k},t)}{a(t)}H(t) - \frac{\dot{\Delta}(\mathbf{k},t)}{a(t)}\right] \tag{2.41}$$

Remembering that $\rho_{\text{comoving}} = \overline{\rho}(t)a^3(t)$, $\Omega_{m,0} = \rho_{\text{comoving}}/\rho_{c,0} = \rho_{m,0}/\rho_{c,0}$, where $\rho_{c,0}$ is the critical density at the present time, and multiplying and dividing Equation 2.41 by $3H_0^2/2$, we have:

$$\delta\dot{\Phi}(\mathbf{k},t) = \frac{3}{2}\frac{H_0^2}{k^2}\Omega_{m,0}\left[\frac{H(t)}{a(t)}\Delta(\mathbf{k},t) - \frac{\dot{\Delta}(\mathbf{k},t)}{a(t)}\right] \tag{2.42}$$

Now, taking the continuity equation:

$$\frac{\partial\rho}{\partial t} + \nabla\cdot(\rho\mathbf{v}_p) = 0 \tag{2.43}$$

Where $\mathbf{v}_p$ is the peculiar velocity field. Writting Equation 2.43 in terms of the density contrast $\Delta = (\rho - \overline{\rho})/\overline{\rho} \Rightarrow \rho = \overline{\rho}\Delta + \overline{\rho}$, dividing the resulting equation by $\overline{\rho}$, and passing from physical r to comoving x coordinates we obtain:

$$-a(t)\dot{\Delta}(\mathbf{x},t) = \nabla_x\cdot[1+\Delta(\mathbf{x},t)]\mathbf{v}_p \tag{2.44}$$

We can define the pseudo-peculiar momentum field to be:

$$\mathbf{p}(\mathbf{x},t) = [1+\Delta(\mathbf{x},t)]\mathbf{v}_p \tag{2.45}$$

$$\Rightarrow -a(t)\dot{\Delta}(\mathbf{x},t) = \nabla_x\cdot\mathbf{p}(\mathbf{x},t) \tag{2.46}$$

To solve Equation 2.46, we make a Fourier transform. Remembering that our convention is a -1 sign in the exponential for a Fourier transform from the position space to the k-space and the inverse transform has sign +1, we obtain:

$$\mathbf{ik} \cdot \mathbf{p}(\mathbf{k}, t) = -a(t)\dot{\Delta}(\mathbf{k}, t) \tag{2.47}$$

It is very important to remark that depending on the sign convention in the Fourier transform, this equation can differ in a (-) sign, i.e., if the convention in the Fourier transform is +1 for position-space to k-space and -1 for k-space to position-space, the equation obtained will be the following:

$$\mathbf{ik} \cdot \mathbf{p}(\mathbf{k}, t) = a(t)\dot{\Delta}(\mathbf{k}, t) \tag{2.48}$$

With our convention, replacing Equation 2.47 into Equation 2.42, we have:

$$\delta\dot{\Phi}(\mathbf{k}, t) = \frac{3}{2}\frac{H_0^2}{k^2}\Omega_{m,0}\left[\frac{H(t)}{a(t)}\Delta(\mathbf{k}, t) + \frac{\mathbf{ik} \cdot \mathbf{p}(\mathbf{k}, t)}{a^2(t)}\right] \tag{2.49}$$

If the sign convention is the one used to find Equation 2.48, when replacing into Equation 2.42 we will have:

$$\delta\dot{\Phi}(\mathbf{k}, t) = \frac{3}{2}\frac{H_0^2}{k^2}\Omega_{m,0}\left[\frac{H(t)}{a(t)}\Delta(\mathbf{k}, t) - \frac{\mathbf{ik} \cdot \mathbf{p}(\mathbf{k}, t)}{a^2(t)}\right] \tag{2.50}$$

This last equation is used by [23]. Equation 2.49 is the same Equation 1.87 which will be used to find the temperature fluctuations, i.e., the anisotropy related with the Sachs-Wolfe effect.

We also have performed an inverse FFT of Equation 2.49 to find the maps of the time derivative of the gravitational potential. We plotted them in slices of thickness 10 Mpch^{-1} as in the aforementioned maps of density fluctuation and potential, for the three different values of $N_g = 64, 128, 256$. Here, we again compare the correspondence between the maps of density fluctuation and potential to find a successful correspondence.

We can see the maps of the time derivative of the gravitational potential for different slices with $N_g = 256$ in Figure 2.10. In this figure, we can see a similar structure to that of the gravitational potential. What we expect is that in the deepest regions of the gravitational potential, its time derivative will change more rapidly than in other regions. This change can be detected when seen the evolution of one of these slices.

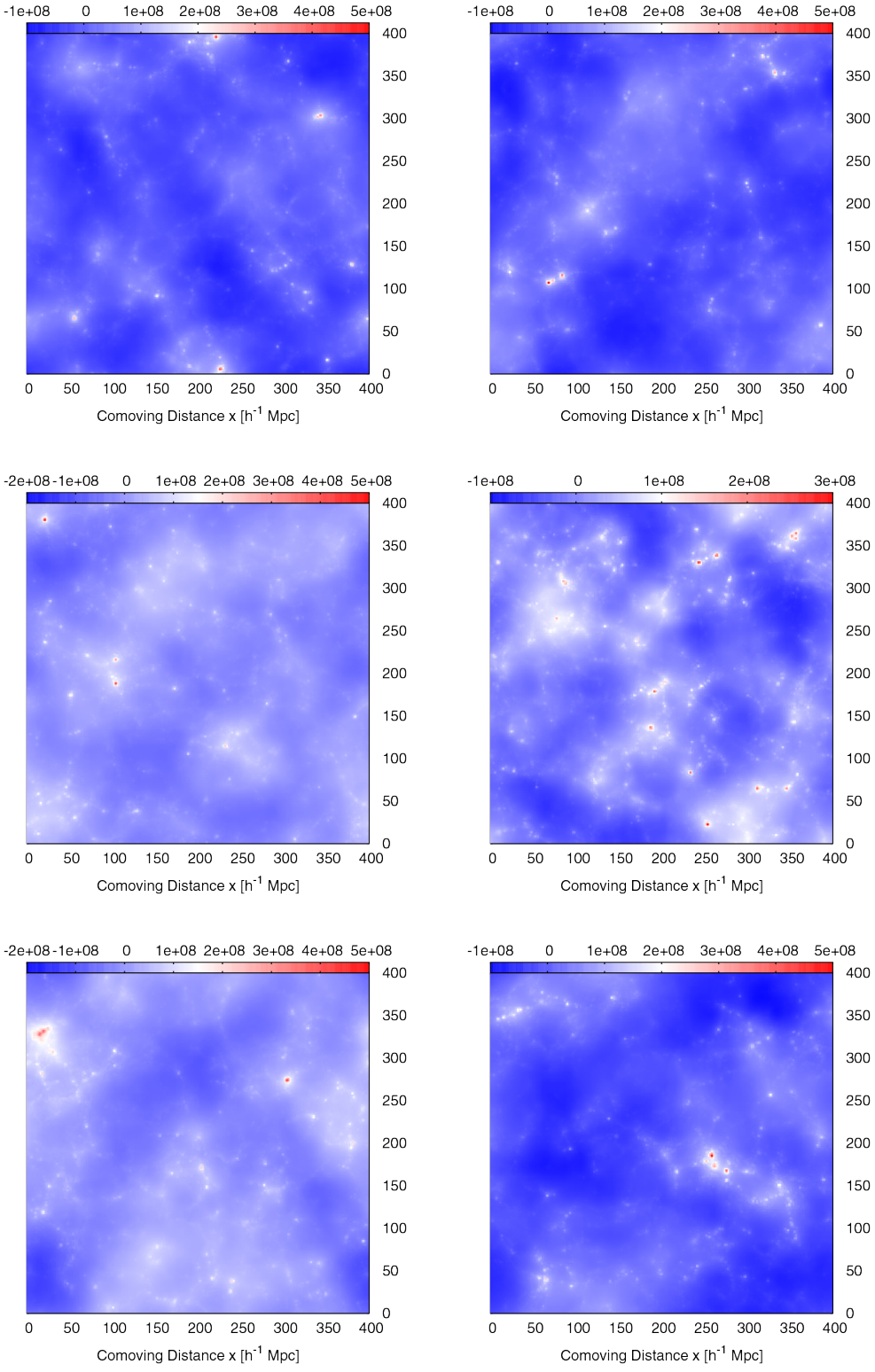

Figure 2.10: Time derivative of the gravitational potential $\dot{\Phi}(\mathbf{r})$ for different slices of thickness $10h^{-1}$Mpc. This slices were calculated with $N_g = 256$ for redshift $z = 0.0$. From left to right and top to bottom, these maps are the respective time derivative maps for each of the potential maps shown in Figure 2.9, i.e., the upper left map in this figure corresponds to the upper left potential map in Figure 2.9, the upper right map corresponds to the upper right potential map, and so on. $\dot{\Phi}$ is given in km^{2}s^{-3}.

2.4 Theoretical Model of Linear Fluctuations and Dimensionless Growth Rate

The linear approximation for the density fluctuations will be used in order to compare the results of the time derivative of the gravitational potential with a special function which becomes the relation for the time derivative in a linear expression. First, we are going to remember the general equation in the small perturbation regime for the density contrast given by Equation 1.58:

$$\frac{\mathrm{d}^2\Delta}{\mathrm{d}t^2} + 2\left(\frac{\dot{a}}{a}\right)\frac{\mathrm{d}\Delta}{\mathrm{d}t} - 4\pi G\rho_0\Delta = 0 \tag{2.51}$$

And the equation for the time derivative of the gravitational potential (Equation 2.42):

$$\dot{\Phi}(\mathbf{k},t) = \frac{3}{2}\frac{H_0^2}{k^2}\Omega_{m,0}\left[\frac{H(t)}{a(t)}\Delta((\mathbf{k},t)) - \frac{\dot{\Delta}(\mathbf{k},t)}{a(t)}\right] \tag{2.52}$$

We can use the fact that in the linear approximation the density contrast is a function of time only and write:

$$\frac{\mathrm{d}\Delta}{\mathrm{d}t} = \frac{\mathrm{d}a}{\mathrm{d}t}\frac{\mathrm{d}\Delta}{\mathrm{d}a} = \dot{a}\frac{\Delta}{a}\frac{\mathrm{d}\ln D}{\mathrm{d}\ln a} = H\Delta\frac{\mathrm{d}\ln D}{\mathrm{d}\ln a} \tag{2.53}$$

If we neglect the decaying mode, the time behaviour of the density contrast would be $\Delta(a) \sim D(a)$ as in Equation 1.75; then from the continuity equation (Equation 1.55) we have:

$$\begin{aligned} H\Delta\frac{\mathrm{d}\ln D}{\mathrm{d}\ln a} &= -\nabla\cdot\mathbf{u} \\ \Rightarrow \Delta &= -\frac{1}{Hf(a)} \end{aligned} \tag{2.54}$$

The function f is called the dimensionless growth rate. For the present epoch and in the case of $\Omega_\Lambda = 0$ a good approximation is:

$$f(\Omega_m, z=0) = \left.\frac{\mathrm{d}\ln D}{\mathrm{d}\ln a}\right|_{z=0} \approx \Omega_m^{0.6} \tag{2.55}$$

Finally, with this last result, we desire to compare the results for the time derivative of the gravitational potential obtained using Equation 2.49 with the corresponding results

from linear theory. In this regime, when performing the time derivative of the density contrast, one can obtain [4] $\dot{\Delta}(\mathbf{k}, z = 0) = \dot{D}\Delta(\mathbf{k}, z = 0)$. Substituting this expression in Equation 2.42, we have:

$$\dot{\Phi}_l(\mathbf{k}, t) = \frac{3}{2}\left(\frac{H_0}{k}\right)^2 \Omega_m \frac{\dot{a}}{a^2}\Delta(\mathbf{k}, t)[1 - f] \tag{2.56}$$

In order to calculate the dimensionless growth rate f, we use the first equality in Equation 2.55 together with Equation 1.76 for the linear growth factor. After taking the respective derivatives and a long algebraic procedure, we obtain the following results:

$$\frac{\mathrm{d}D(a)}{\mathrm{d}a} = \frac{5}{2}\beta(a)\left\{\Omega_m(a) + \eta(a)\left[\Omega_m(a)\beta(a)O(a) - 1\right]\right\} \tag{2.57}$$

Where the expressions $\beta(a)$, $\eta(a)$ and $O(a)$ are given by:

$$\begin{aligned}
\eta(a) &= \frac{3\Omega_{\Lambda,0}a^3}{(1 + y^3)} \\
\beta(a) &= \frac{1}{\Omega_m^{4/7}(a) - \frac{1}{140}\Omega_m^2(a) + \frac{209}{70}\Omega_m(a) + \frac{1}{70}} \\
O(a) &= \frac{4}{7}\Omega_m^{-3/7}(a) - \frac{1}{70}\Omega_m(a) + \frac{209}{70}
\end{aligned}$$

and y given by Equation 1.74. Whit those expressions, the dimensionless growth rate will become:

$$f(a) = \frac{\mathrm{d}\ln\left(D(a)\right)}{\mathrm{d}\ln\left(a\right)} = \beta(a)\xi(a)\zeta(a) \tag{2.58}$$

With:

$$\begin{aligned}
\xi(a) &= \Omega_m^{4/7}(a) - \Omega_\Lambda(a) + \left(1 + \frac{\Omega_m(a)}{2}\right)\left(1 + \frac{\Omega_\Lambda(a)}{70}\right) \\
\zeta(a) &= 1 + \eta(a)\left[\beta(a)O(a) - \frac{1}{\Omega_m(a)}\right]
\end{aligned} \tag{2.59}$$

And finally, $\Omega_m(a)$ and $\Omega_\Lambda(a)$ given by Equation 1.77 and Equation 1.78, respectively.

With the help of Equation 2.58 and Equation 2.56 and performing again a FFT in order to obtain the values of the time derivative of the gravitational potential in the linear

regime $\dot{\Phi}_l$, it has been obtained the maps of this values analogous to the maps found with the expression of Equation 2.49. The maps of $\dot{\Phi}_l$, shown in Figure 2.12 have a good correspondence with those shown in Figure 2.10. As said before, in the deepest regions of the gravitational potential maps it is expected to have a more rapid variation of the time derivative.

In order to verify the behavior and the range of the dimensionless growth rate given by Equation 2.58 in terms of the scale factor a or even in terms of the redshift z, the dimensionless growth rate was calculated for different values of a and z. Figure 2.11 shows the behavior of this function in terms of both quantities. In both cases Equation 2.58 should be lesser than 1 for all values of z or a, and it is verified in Figure 2.11.

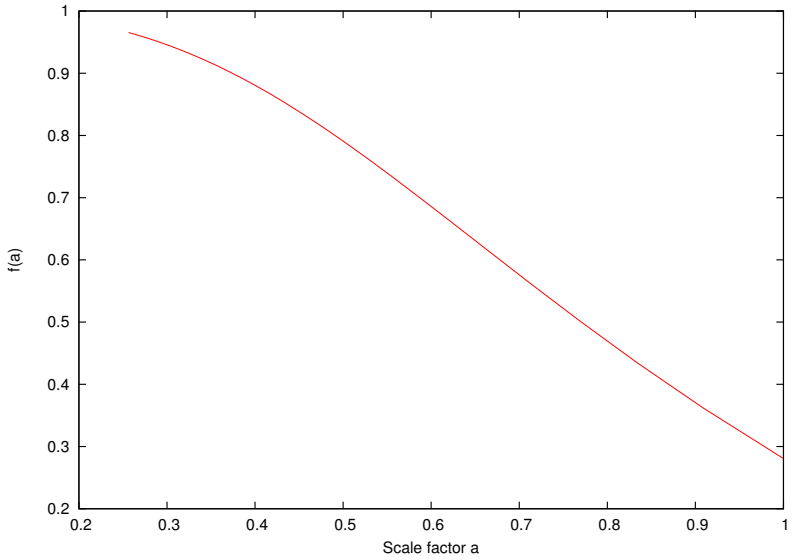

Figure 2.11: Dimensionless growth rate f in terms of the scale factor a. The dimensionless growth rate should be lesser than 1, in order to obtain a sign dependence on Equation 2.56 given only by the sign of the density contrast Δ.

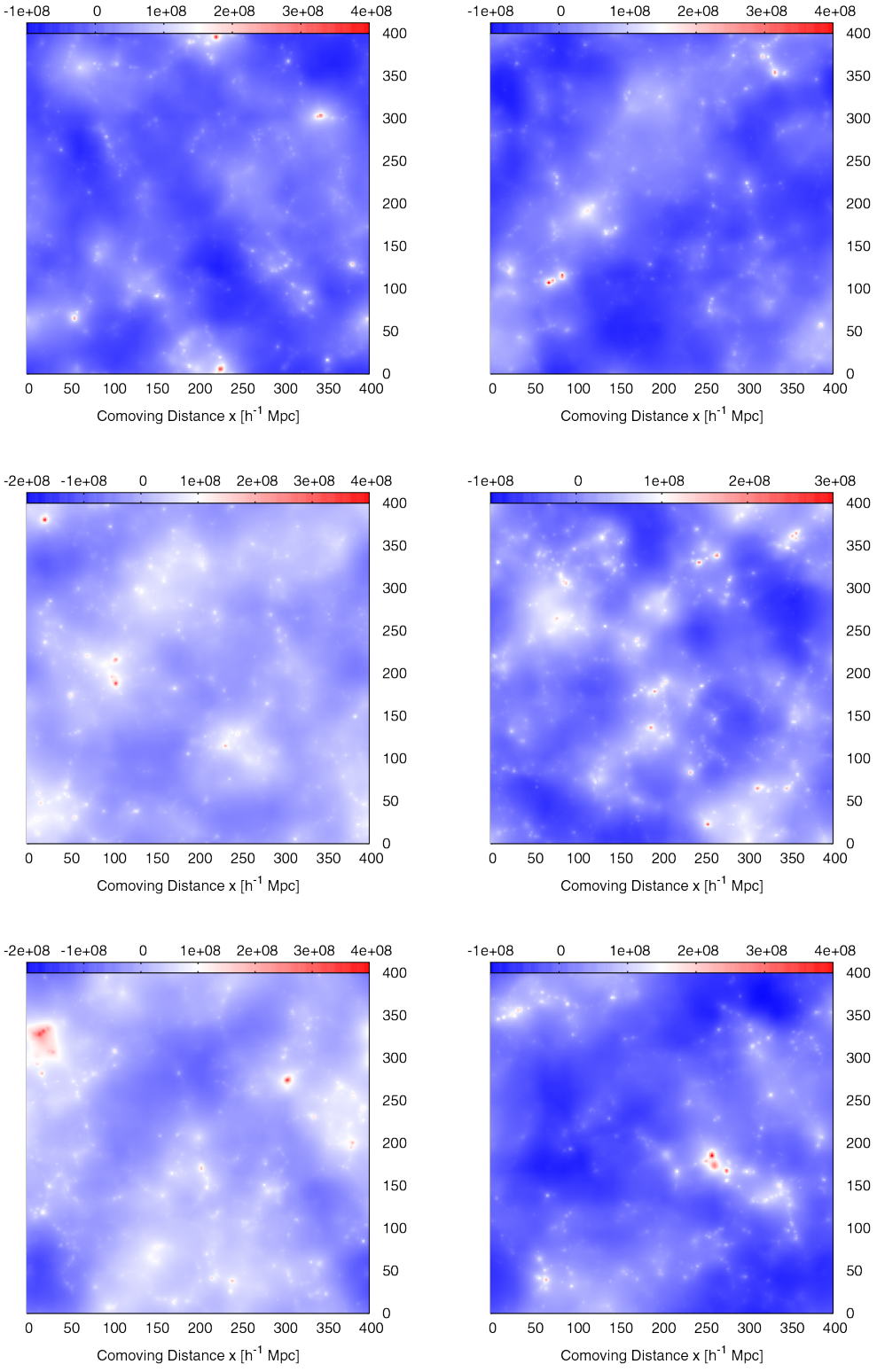

Figure 2.12: Time derivative of the gravitational potential in the linear regime $\dot{\Phi}_l(\mathbf{r})$ for different slices of thickness $10h^{-1}$Mpc. This slices were calculated with $N_g = 256$ for redshift $z = 0.0$. From left to right and top to bottom, these maps are the respective time derivative maps for each of the potential maps shown in Figure 2.9. It is also remarkable to say that those maps have a good correspondence with the maps obtained with the exact expression of the time derivative, in Figure 2.10. $\dot{\Phi}_l$ is given in km^{2}s^{-3}.

"The scientific man does not aim at an immediate result. He does not expect that his advanced ideas will be readily taken up. His work is like that of the planter - for the future. His duty is to lay the foundation for those who are to come, and point the way."

Nikola Tesla.

CHAPTER

3

Estimation of the Late Integrated Sachs-Wolfe Effect

In this chapter we are going to describe the method we used to estimate the late Integrated Sachs-Wolfe effect in the cosmological simulation. It should be remarked that in this work we are not computing a complete Integrated Sachs-Wolfe effect, due to the fact that this effect is underwent by the photons when they pass through all the structures in the Universe between the surface of Last Scattering and the Earth, while our work is constrained to the $400h^{-1}$ that compose the lenght of our simulation box.

In order to compute the Sachs-Wolfe integral from Equation 3.1, it is necessary to perform an interpolation of the function $\dot{\Phi}(x_z)$, being x_z the comoving position in the z-axis of the cubic box used. Once this interpolation is completed, the SW integral is calculated and the maps of the temperature variation in the CMB can be obtained. We will make a brief discussion remembering the physical implication of the SW effect before we show the results of the SW maps, and then make a discussion about the tests we perform to our results.

3.1 The Integrated Sachs-Wolfe Effect

As seen before in subsection 1.5.5, the Sachs-Wolfe effect studied in this work is the called Integrated Sachs-Wolfe Effect (ISW), which is produced between the surface

of last scattering and the Earth. The ISW effect is a fluctuation on the temperature of the Cosmic Microwave Background (CMB) induced by gravitational instabilities when photons pass through an evolving gravitational potential well. As the photons climb up gravitational hills or fall into gravitational wells, associated with regions of overdensities or underdensities through the density contrast Δ, the photons will change their energies. This change in the energy of the CMB photons is related to a change in the temperature of the CMB ΔT respect to the mean CMB temperature $\overline{T}_0$. The expression of ΔT can be obtained through integration of the time derivative of the gravitational potential well $\dot{\Phi}$ as a function of cosmic time t or as a function of the comoving coordinates $\mathbf{x}$.

In this work, it has been used the expression that relates the perturbation in the mean temperature ΔT with the temporal change of the gravitational potential through the integration over the comoving position (see subsection 1.5.5), as follows:

$$\Delta T(\hat{\mathbf{n}}) = \frac{2}{c^3}\overline{T}_0 \int_0^{x_{r,L}} \dot{\Phi}(x_r, \hat{\mathbf{n}})\, \mathrm{d}x_r \tag{3.1}$$

Which is Equation 1.85 seen before. The time derivative of the gravitational potential well $\dot{\Phi}$ has been obtained through the Poisson equation (Equation 1.57) with Fourier methods, and allows us to find its expression in the Fourier space, given by:

$$\dot{\Phi}(\mathbf{k}, t) = \frac{3}{2}\frac{H_0^2}{k^2}\Omega_{m,0}\left[\frac{H(t)}{a(t)}\Delta((\mathbf{k}, t)) + \frac{\mathbf{i}\mathbf{k}\cdot\mathbf{p}(\mathbf{k}, t)}{a^2(t)}\right] \tag{3.2}$$

When this expression is computed, we can find the numerical values of $\dot{\Phi}$ in the position-space, and perform the integration to obtain the perturbations in the temperature. The method used to calculate this temperature perturbations is going to be described in section 3.2. It has also been used a linear approximation in order to compare the results from Equation 3.2 with those from this linear regime. Furthermore, as the ISW effect is related with the linear growth of structures, a comparison between this linear regime in which the ISW effect dominates and the exact solution is a good way to estimate the accuracy of the results. Assuming a linear growth of the structures, related with the density contrast Δ, the expression in the linear approximation of $\dot{\Phi}(\mathbf{x})$ is given by (see section 2.4):

$$\dot{\Phi}_l(\mathbf{k},t) = \frac{3}{2}\left(\frac{H_0}{k}\right)^2 \Omega_m \frac{\dot{a}}{a^2}\Delta(\mathbf{k},t)[1-f] \tag{3.3}$$

Then, we use Equation 3.1, Equation 3.2 and Equation 3.3 to compute the Integrated Sachs-Wolfe effect using the exact values from the simulation as well as the approximation from the linear theory.

3.2 Temperature Perturbations and Sachs-Wolfe Anisotropy Maps

In order to compute the temperature perturbations it is necessary to know an expression for the time derivative of the gravitational potential $\dot{\Phi}(\mathbf{x})$. As we are working with the numerical values of $\dot{\Phi}(\mathbf{x})$ calculated by means of a Fast Fourier Transform (see subsection 2.3.5) it should be performed an interpolation of the numerical values of $\dot{\Phi}(\mathbf{x})$ of each cell point in order to obtain a function that can be adequately integrated. In this section we are going to describe the method we used to perform such interpolation and the corresponding integration to obtain the temperature perturbations.

3.2.1 Interpolation and Numerical Integration of the Function $\dot{\Phi}(x_z)$

At this point, it is necessary to clarify that as we need to calculate the Sachs-Wolfe integral (Equation 3.1), we have to choose some snapshots of the same cosmological simulation for different redshifts in order to create a mock catalogue, representing a part of the Universe with the different snapshots, one behind the other, beginnig with the snapshot for redshift $z = 0.0$ where the observer is going to be placed, and finishing with a snapshot of redshift approximately $z = 2.0$. This full work is going to be performed in a future step of this project, but in the present work the snapshot with redshift $z = 0.0$ has been chosen in order to calculate the Sachs-Wolfe integral and analyze its behavior in only one snapshot.

Once the gravitational potential $\Phi(\mathbf{x})$ and its time derivative $\dot{\Phi}(\mathbf{x})$ are computed in the cosmological simulation through the Fast Fourier Transforms described in chapter 2, we need to choose a direction along which we are going to perform the SW integral and a place to put the observer. The observer is placed in the plane with comoving position $x_z = 0$, where x_z represents the z-component of the comoving position vector $\mathbf{x}$. Then, along the z-axis we performed an interpolation of the values of $\dot{\Phi}(x_z)$. In order to compute

the interpolation function, we need to construct, again, a grid with the same number of grid points used in the Fast Fourier Transform. Remembering that we are going to analyze the results obtained from the grids with $N_g = 256^3$ cells, we built a grid with the same number of grid points per axis.

Coming back to the interpolation, after the grid construction, we assign again the respective values of position, density contrast, gravitational potential and time derivative of the potential to each of the grid points. For each value of fixed x_x and x_y (the x and y-component of the vector $\mathbf{x}$) we have 2 vectors of N_g-components, one corresponding to the values of x_z of each one of the grid points along the z-axis, and one corresponding to the values of the time derivative $\dot{\Phi}(x_z)$. We need to identify each vector for fixed x_x, x_y. This identification is made with the help of and ID similar to those used in the Fourier Transform. In this case, the ID of each vector, denoted by n is given by:

$$n = in_y + j \tag{3.4}$$

Where i and j are the loop indices related to the x and y-component of each cell, respectively. After the assignment of values of x_z and $\dot{\Phi}(x_z)$ for each column and the identification by means of the ID n, we performed the interpolation of the vector containing the values of x_z and the vector with the values of $\dot{\Phi}(x_z)$, finding an interpolated function $\dot{\Phi}_{\text{interp}}(x_z)$. We simply use a linear interpolation between the data points. As the data sets do not contain the extreme values of the box, i.e., $x_z = 0h^{-1}$Mpc and $x_z = 400h^{-1}$Mpc, we force that the values of the position of the first grid point to be precisely $x_z = 0h^{-1}$Mpc and the position of the last grid point to be $x_z = 400h^{-1}$Mpc.

With this function, $\dot{\Phi}_{\text{interp}}(x_z)$ we can perform the integral from Equation 3.1 in order to obtain a map of the behavior of this integral along one of the snapshots. Both, the interpolation and integration of the function $\dot{\Phi}_{\text{interp}}(x_z)$ were performed with the help of the GNU Scientific Library (GSL) [1]. GSL is a better documentated library than the FFTW library, then it is not necessary to show how those interpolations were performed.

In Figure 3.1 we show the curves of one of the interpolated functions for the vector with ID $n_{128} = 0$ for the grid $N_g = 128^3$ and the comparison with the four corresponding vectors of the grid $N_g = 256^3$ that can be inside the vector $n_{128} = 0$ of the grid $N_g = 128^3$, i.e., the vectors with IDs $n_{256} = 0, 1, 256, 257$. Also, a curve for the vector with ID $n_{64} = 0$ for the grid $N_g = 64^3$ is depicted, although obviously it is not so accurately fitted with the other five curves, the shape and the order of magnitude of the

[1] http://www.gnu.org/software/gsl/

six curves is very similar. We can also see that the value of the interpolated function $\dot{\Phi}_{\text{interp}}(x_z)$ does not change so much if different resolutions are used. In particular, the yellow-circled curve of Figure 3.1 corresponds to the interpolation for $N_g = 64$, the aquamarine-squared curve corresponds to the interpolation for $N_g = 128$, while the other curves correspond to the cells of the grid $N_g = 256$. So we conclude that our results are numerically convergent and discretization is not mucha an issue.

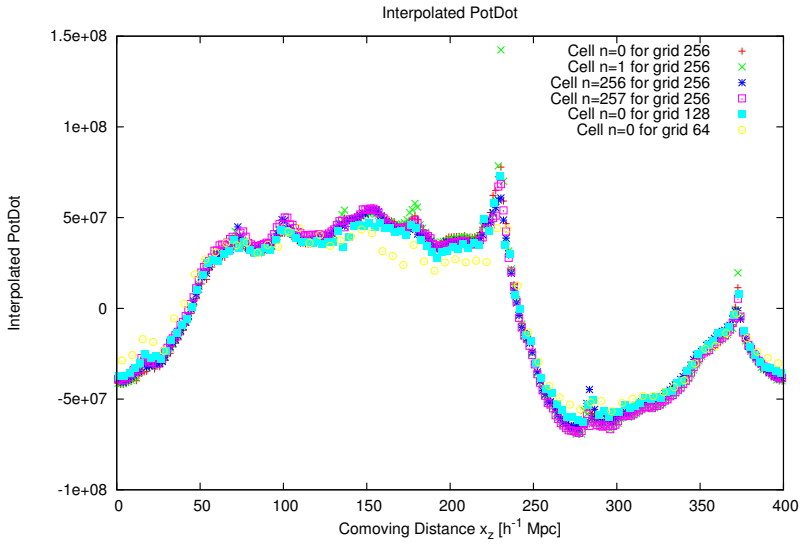

Figure 3.1: Interpolated function $\dot{\Phi}_{\text{interp}}(x_z)$. This figure shows six different curves, four of each correspond to the interpolated function for the vectors with ID $n_{256} = 0, 1, 256, 257$ of the grid $N_g = 256$, while the aquamarine-squared curve correspond to the interpolated function for the vector $n_{128} = 0$ of the grid $N_g = 128$ and the yellow-circled curve correspond to the interpolated function for the vector $n_{64} = 0$ of the grid $N_g = 64$. The curves show the interpolation performed from $x_z = 0h^{-1}$Mpc to $x_z = 400h^{-1}$Mpc with a step of $\Delta x_z = 1h^{-1}$Mpc. These curves show that both, the order of magnitude and the shape of the interpolated function do not depend on the resolution.

Once an interpolated function for the time derivative of the gravitational $\dot{\Phi}_{\text{interp}}(x_z)$ potential is calculated for certain fixed values of x_x and x_y, a numerical integration of Equation 3.1 was performed. A Simpson-integration method was implemented manually. With this routine we obtain the N_g^2 values of the integral for the N_g^2 cell points at $x_z = 0$ and after multiplying them with the corresponding factors preceding the integral in Equation 3.1, we can obtain the late Integrated Sachs-Wolfe maps for one snapshot. The integration with the Simpson method was performed with two different integration steps, in order to test the numerical convergence of the integration. For the SW map shown

in Figure 3.2, they have been used 10000 steps for the integration, but a first integration with only 1000 steps were performed before. The comparison between both results wil be discussed in section 3.3.

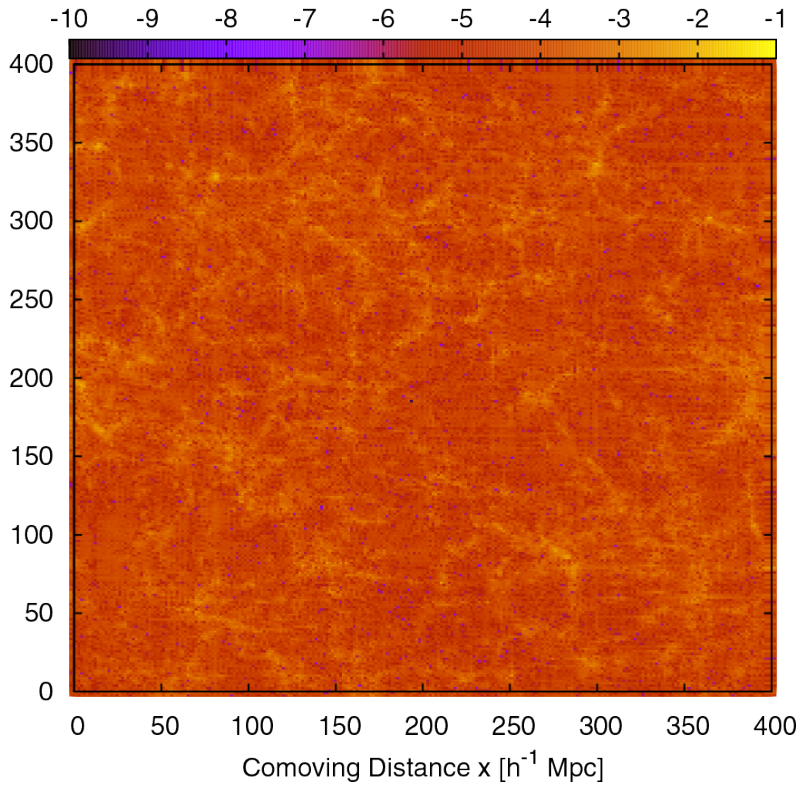

Figure 3.2: Map of the late Integrated Sachs-Wolfe anisotropy obtained from the integration of the interpolation function $\dot{\Phi}_{\text{interp}}(x_z)$ with the values obtained from Equation 3.2. This map was made with 10000 integration steps. The temperatures are in logarithmic scale, i.e., $\log_{10}(\Delta T)$, with with $[\Delta T] = \mu$K.

The same method was used for the values obtained with the linear approximation for the time derivative of the gravitational potential with the help of Equation 3.3 and another interpolated function $\dot{\Phi}_{\text{int,linear}}(x_z) = \dot{\Phi}_{\text{i,l}}(x_z)$ was found and integrated. The same comparison between the interpolated functions for each grid, as in Figure 3.1, was performed for the function $\dot{\Phi}_{\text{i,l}}(x_z)$, and it is shown in Figure 3.3. It is possible to see that both, the shape and order of magnitude of the curves in Figure 3.3 is very similar to those of Figure 3.1. The corresponding SW map with 10000 integration steps is shown in Figure 3.4. Its comparison with the map obtained with 1000 integration steps will be made in section 3.3.

In order to make some verifications on the implemented method and on the obtained results, an statistical analysis was performed with the help of the GSL library, and for

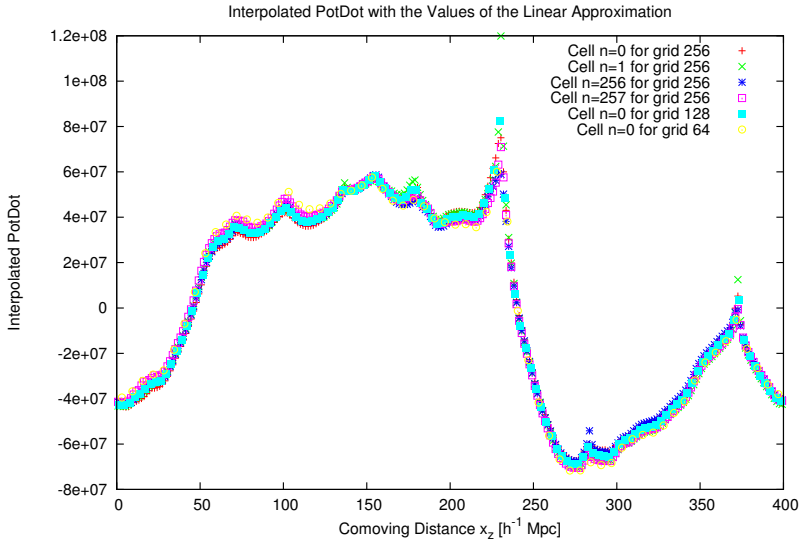

Figure 3.3: Interpolated function with the values of the linear approximation $\dot{\Phi}_{\mathrm{i,l}}(x_z)$. This figure shows six different curves, four of each correspond to the interpolated function for the vectors with ID $n_{256} = 0, 1, 256, 257$ of the grid $N_g = 256$, while the aquamarine-squared curve correspond to the interpolated function for the cell $n_{128} = 0$ of the grid $N_g = 128$ and the yellow-circled curve correspond to the interpolated function for the vector $n_{64} = 0$ of the grid $N_g = 64$. The curves show the interpolation performed from $x_z = 0h^{-1}$Mpc to $x_z = 400h^{-1}$Mpc with a step of $\Delta x_z = 1h^{-1}$Mpc. These curves show that both, the order of magnitude and the shape of the interpolated function do not depend on the resolution.

that reason, the conventions of GSL for the calculus of the higher moments (skewness and kurtosis) are assumed here. The results of the temperature fluctuations ΔT obtained for two different snapshots were compared. The snapshot of the cosmological simulation used until now, which has the positions and velocities of all particles at redshift $z = 0.0$, which means that such particles are at present time, was compared with a snapshot with redshift $z = 2.16874 \approx 2.17$, which means, it contains the positions and velocities of the same particles but in a past time. It was expected that the temperature fluctuations ΔT were more uniform respect to the mean temperature of the CMB, i.e., such perturbations were near to be $\Delta T = T - \overline{T}_0 = 0$. Figure 3.5 shows the Sachs-Wolfe map obtained for the snapshot with redshift $z = 2.17$ in the exact regime, while Figure 3.6 shows the same map in the linear regime, both maps obtained with 10000 integration steps. Figure 3.7 shows the histograms with the distributions of temperatures for both snapshots and in both regimes: the linear regime, according to Equation 3.3 and the exact regime from Equation 3.2.

According to the theory seen in subsection 1.5.5, the cold points in the maps shown

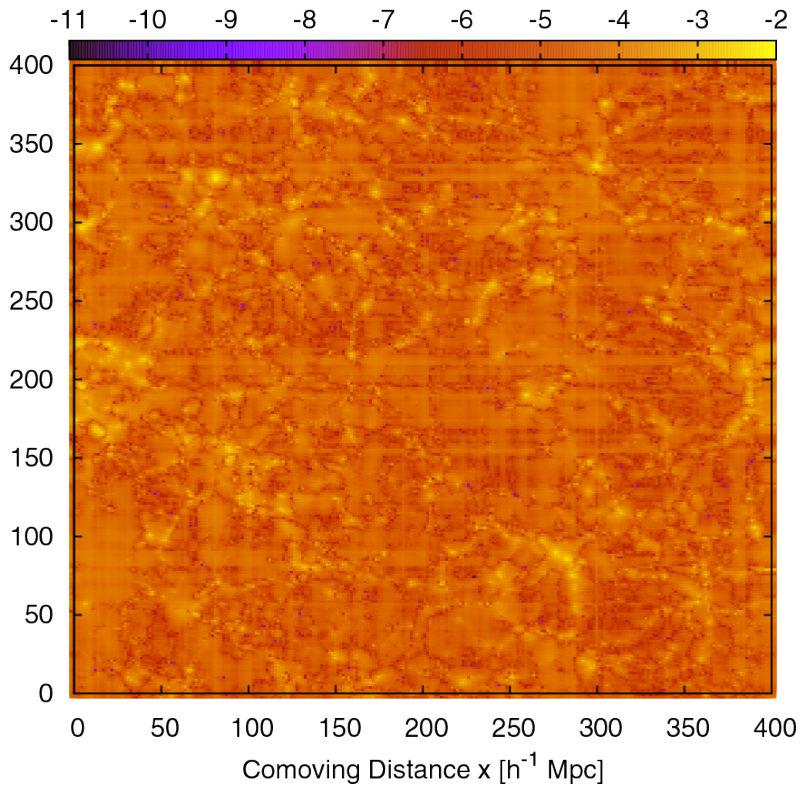

Figure 3.4: Map of the late Integrated Sachs-Wolfe anisotropy obtained from the integration of the interpolation function $\dot{\Phi}_{\text{interp}}(x_z)$ with the values obtained in the linear regime from Equation 3.3. This map was made with 10000 integration steps. The temperatures are in logarithmic scale, i.e., $\log_{10}(\Delta T)$, with $[\Delta T] = \mu$K.

in Figure 3.2, Figure 3.4, Figure 3.5 and Figure 3.6 correspond to underdense regions, that means, regions where the density is very near or even lower than the mean matter density $\overline{\rho}$ and in these regions, the gravitational potential could be interpreted as a mount, not as a well. In underdense regions, at high redshift the photons climb the hill losing energy, and with the expansion of the Universe, the "height" of the mount becomes lower and when the photons are going to fall off from the mount, photons will win energy, but in a less amount than the energy they lost previously. On the other hand, hot points in the Sachs-Wolfe maps correspond to regions where the gravitational potential is a well, hosting matter structures, i.e., in those regions the density is higher than the mean matter density of the Universe. Then, the photons will begin to descend the potential well, gaining energy, and after some time, they will climb the other side of the potential well, losing a quantity of energy that is less than the quantity they gained before, due to the lost of depth of the potential well as the Universe accelerates its expansion. According to these interpretations, on the maps shown on the mentioned figures the regions where

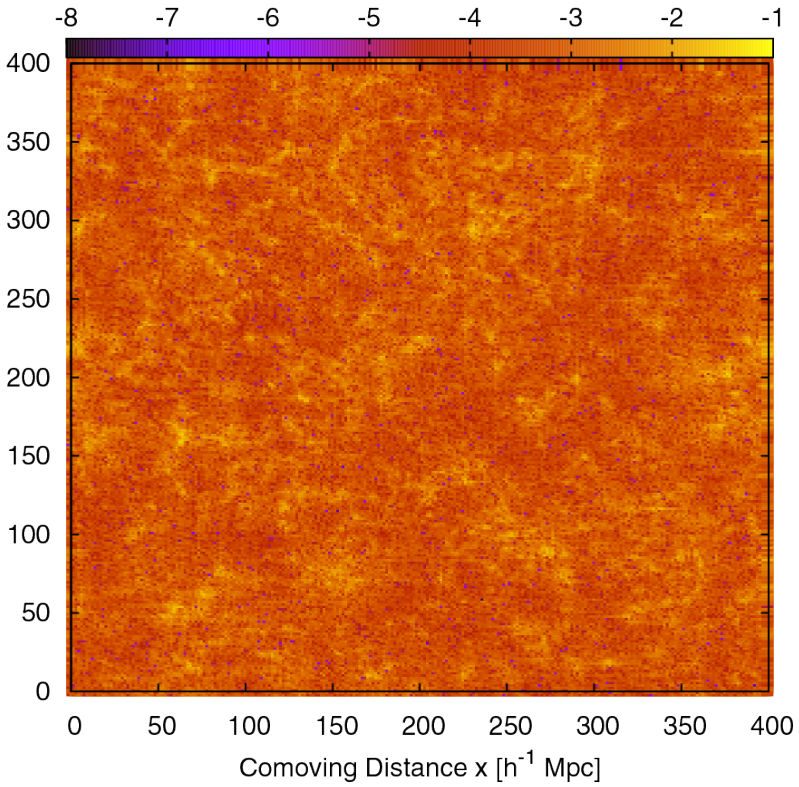

Figure 3.5: Map of the late Integrated Sachs-Wolfe anisotropy corresponding to the snapshot with redshift $z = 2.17$ obtained with the exact solution from Equation 3.2. This map was made with 10000 integration steps. The temperatures are in logarithmic scale, i.e., $\log_{10}(\Delta T)$, with $[\Delta T] = \mu$K.

the ΔT values are higher, can be related with some structures like clusters of particles or even with filaments containing a matter density that is over $\overline{\rho}$ and that are thick along the integration axis. Conversely the colder regions are related to underdensities (not only void regions, but they can be also included in this interpretation) along the integration axis.

Concerning to the histograms in Figure 3.7, one can see that in the four curves shown, the mean $\overline{\Delta T}$ is zero, and the median of the data ΔT_{median} is very near to zero, allowing us to conclude that for most of the data, the differences between the temperature at each grid cell point relative to the mean temperature of the CMB, $\Delta T = T - \overline{T}_0$, is zero, or that the temperature at most of the points of the maps are exactly or very near to the mean temperature of the CMB $\overline{T}_0$. Taking into account that some of the higher order moments of a distribution (skewness or third moment, b_1 and kurtosis or fourth moment, g_2) can give us information about the shape and symmetry of the distribution as:

- When the skewness is positive ($b_1 > 0$) we have an asymmetric distribution with a

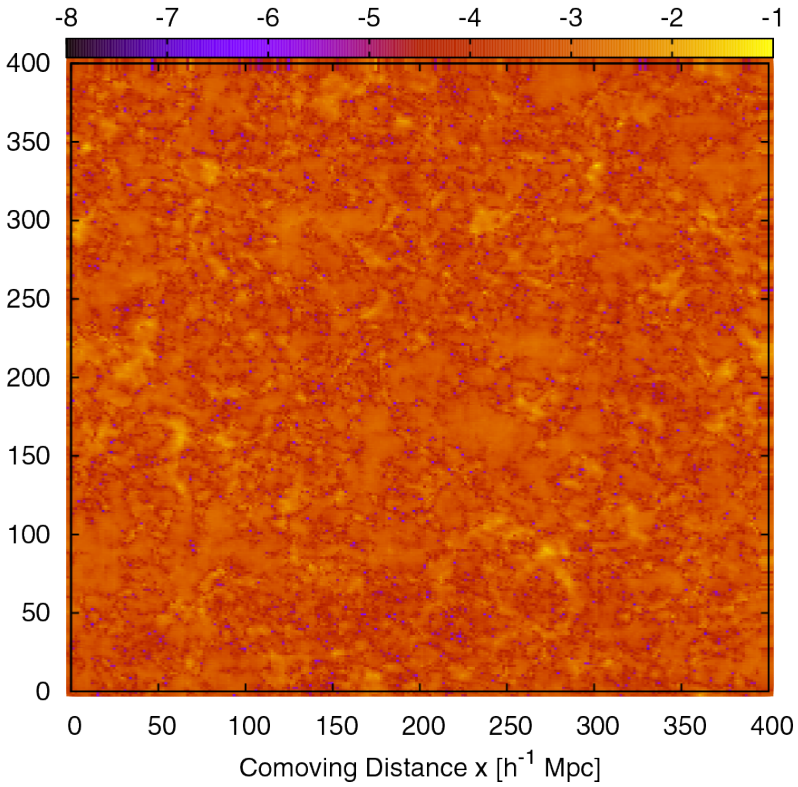

Figure 3.6: Map of the late Integrated Sachs-Wolfe anisotropy corresponding to the snapshot with redshift $z = 2.17$ obtained with the values from the linear regime of Equation 3.3. This map was made with 10000 integration steps. The temperatures are in logarithmic scale, i.e., $\log_{10}(\Delta T)$, with $[\Delta T] = \mu$K.

tail extending to the positive values.

- If $b_1 < 0$, the distribution has a tail extending towards the negative values.
- When the kurtosis is positive ($g_2 > 0$) the distribution is called leptokurtic, which means that it has a more acute peak with flatter tails.
- If $g_2 < 0$, the distribution is platykurtic, with a lower and wider peak and thinner tails.

With those concepts in mind, it is possible to see that all the four distributions of Figure 3.7 are leptokurtic. The skewness of the curves for the snapshot with redshift $z = 0.0$, indicates us that they have an asymmetric tail toward the negative values of ΔT, which also means that for this redshift, there are slightly more cold regions in the Sachs-Wolfe maps than the hotter ones. The tail towards the negative values of ΔT is more evident in the linear approximation, and can be seen in the values of the Table 3.1 and in

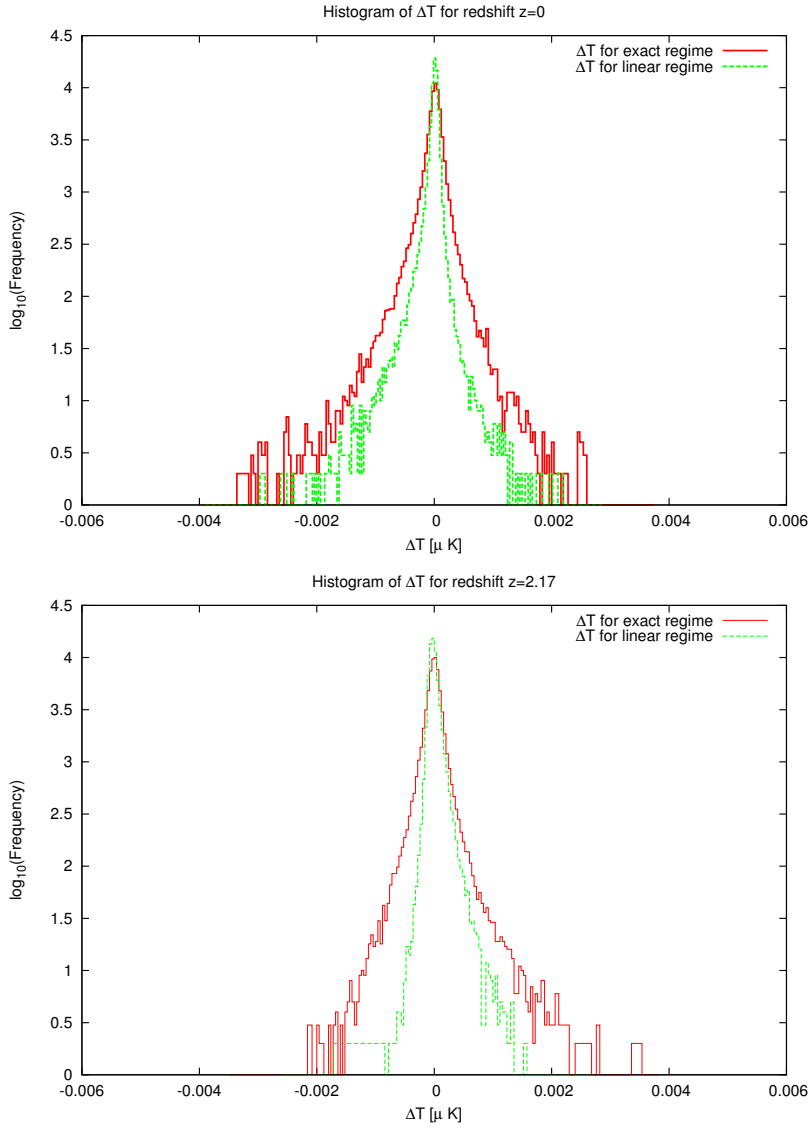

Figure 3.7: Histograms of the temperature fluctuations ΔT for the snapshot with redshift $z = 0.0$ (top figure) and for the snapshot with redshift $z = 2.17$ (bottom figure). For the highest redshift it is necessary to multiply the obtained temperature fluctuation ΔT by the squared scale factor a^2, in agreement with Equation 1.18, in order to obtain the temperature fluctuation at present time. For redshift $z = 0.0$ it is not necessary to perform such scale operation because the scale factor has the value $a = 1$. The temperature fluctuations are in [μ K]. Some statistical properties for the four histograms are given in Table 3.1.

Statistical property	Redshift			
	$z = 0.0$		$z = 2.17$	
	Regime			
	Exact	Linear	Exact	Linear
$\overline{\Delta T}$	0.0	0.0	0.0	0.0
ΔT_{median}	1.562×10^{-5}	1.1118×10^{-5}	-5.7×10^{-7}	-1.689×10^{-5}
σ^2	7×10^{-8}	2×10^{-8}	5×10^{-8}	1.0×10^{-8}
σ	2.673×10^{-4}	1.5136×10^{-4}	2.1670×10^{-4}	1.1127×10^{-4}
b_1	-3.96614	-8.2077	1.303624	4.112498
g_2	190.07742	356.84236	28.2038	92.22308

Table 3.1: Statistical properties for the histograms of the temperature fluctuation for the Sachs-Wolfe maps in Figure 3.7. $\overline{\Delta T}$ is the mean, ΔT_{median} is the median, σ^2 is the variance, σ is the standard deviation, b_1 is the skewness and g_2 is the kurtosis.

the top figure of Figure 3.7. In the case of the snapshot with redshift $z = 2.17$, although their behavior is also of a leptokurtic distribution as those for $z = 0.0$, their skewness show us that the asymmetry is in the opposite way, i.e., as $b_1 > 0$ in each distribution, each one has a tail which extends towards the positive values of ΔT, meaning that the corresponding SW maps has slightly more hotter regions than colder ones.

In order to relate those asymmetries and shapes of the histograms of ΔT with other physical quantities, the histograms for the density contrast $\Delta(x)$ and the time derivative of the gravitational potential $\dot{\Phi}(x)$ where calculated for both snapshots. The histograms of the density contrast are shown in Figure 3.8, and the corresponding statistical properties are shown in Table 3.2.

Statistical property	Linear scale		Log_{10} scale	
	Redshift			
	$z = 0.0$	$z = 2.17$	$z = 0.0$	$z = 2.17$
$\overline{\Delta}$	-5.5×10^{-7}	-5.5×10^{-7}	-0.926703	-0.188314
Δ_{median}	-0.75	-0.375	-0.602043	-0.20412
σ^2	37.686872	2.150968	2.394453	0.246356
σ	6.138963	1.466618	1.547402	0.496342
b_1	54.674557	14.404696	-1.969069	-7.033603
g_2	6100.466752	756.215874	2.753099	111.645074

Table 3.2: Statistical properties for the histograms of the density contrast in Figure 3.8. $\overline{\Delta}$ is the mean, Δ_{median} is the median, σ^2 is the variance, σ is the standard deviation, b_1 is the skewness and g_2 is the kurtosis.

The histograms for the density contrast $\Delta(\mathbf{x})$ shows that for redshift $z = 0.0$ there are many fluctuations with higher values of Δ, which is an opposite behavior as for $z = 2.17$. This behavior for $z = 0.0$ indicates that there exist many cells of the grid that can be interpreted as regions where the density contained inside is higher than the mean density of the simulation $\overline{\rho}$. Those overdense regions compose the structures as clusters or filaments where there is a great amount of particles.

Conversely, the histogram of the density contrast for $z = 2.17$ indicates a higher frequency for the fluctuations with lower values of $\Delta(\mathbf{x})$, which means that there exist a greatest amount of regions where the density contained inside the cells is very near or even lower than $\overline{\rho}$, composing the underdense regions or voids.

The behavior described above is expected, because at higher redshifts not all the particles have been atracted to each other and the simulations (and the Universe) whould present a lightly uniform distribution near the lower values of $\Delta(\mathbf{x})$.

The asymetric behavior in the density contrast should affect the shape of the distribution of $\dot{\Phi}(\mathbf{x})$, and then, the distribution of temperature fluctuations ΔT of the late ISW maps should show it, as we are going to describe. For the time derivative of the potential, the histograms are shown in, Figure 3.9 Figure 3.10 and Figure 3.11. The statistical analysis of those histograms is shown in Table 3.3 for $z = 0.0$ and Table 3.4 for $z = 2.17$, respectively.

Redshift $z = 0.0$				
Statistical property	Linear scale		Log_{10} scale	
	Regime			
	Exact	Linear	Exact	Linear
$\overline{\dot{\Phi}}$	0.0	0.0	8.07166	8.087991
$\dot{\Phi}_{\text{median}}$	-9.76867×10^5	-1.172015×10^6	8.08471	8.1
σ^2	1.031169×10^{15}	1.087435×10^{15}	0.015715	0.015194
σ	3.21118×10^7	3.297628×10^7	0.125362	0.123267
b_1	0.592107	0.545591	13.98739	13.759251
g_2	0.20693	0.231962	-1.220344	-1.171878

Table 3.3: Statistical properties for the histograms of the time derivative of gravitational potential in Figure 3.9 for redshift $z = 0.0$. $\overline{\dot{\Phi}}$ is the mean, $\dot{\Phi}_{\text{median}}$ is the median, σ^2 is the variance, σ is the standard deviation, b_1 is the skewness and g_2 is the kurtosis.

In order to analyze the histograms of , it is necessary to make a previous analysis of the maps constructed in chapter 2. It is possible to see a very good correlation between

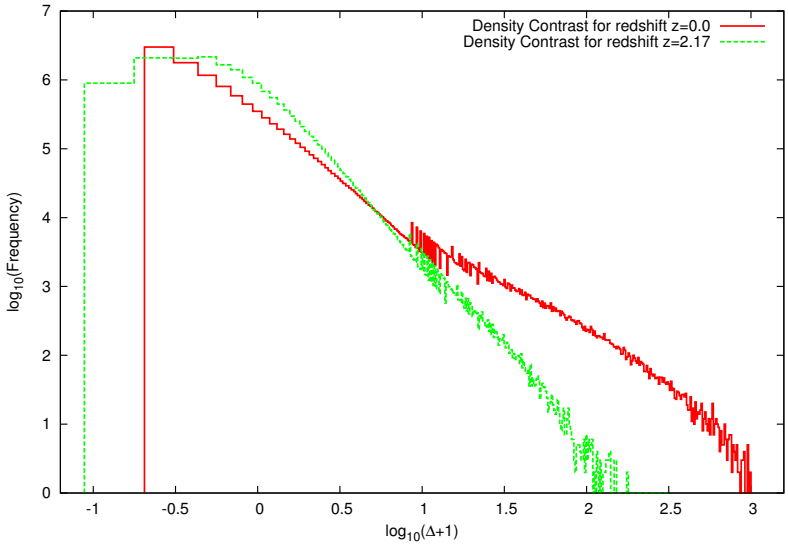

Figure 3.8: Histograms of the density contrast $\Delta(x)$. The figure shows two curves, one for the snapshot with redshift $z = 0.0$ and for the snapshot with redshift $z = 2.17$, where the density contrast data are in logarithmic scale: $\log_{10}(\Delta + 1)$. Some statistical properties of the histograms are given in Table 3.2.

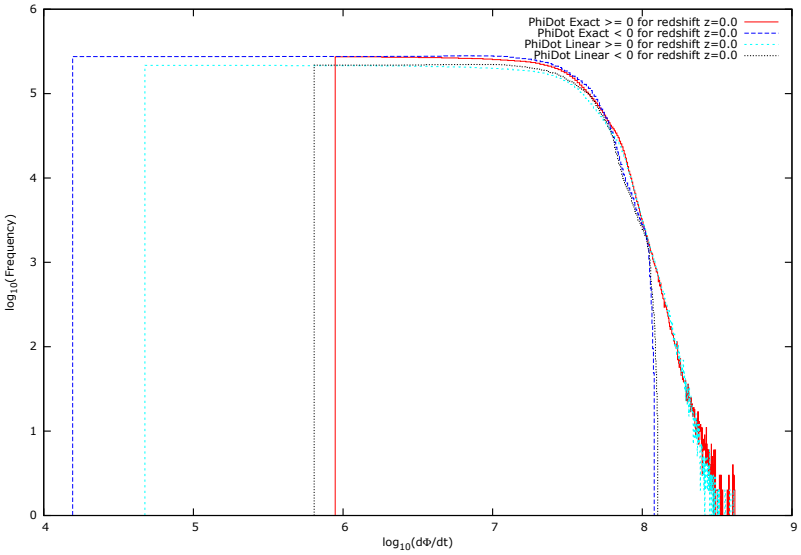

Figure 3.9: Histogram of the time derivative of the gravitational potential $\dot{\Phi}$ for redshift $z = 0.0$. The curves shown give a comparison between the distribution of the linear regime data (Equation 3.3) and the data obtained with the exact solution (Equation 3.2) The data shown in both histograms are given in logarithmic-scale. For each regime, one of the curves gives the values of $\dot{\Phi} > 0$, while the other curve gives the absolute value of the data when $\dot{\Phi} < 0$. The statistical analysis of the histograms is shown in Table 3.3.

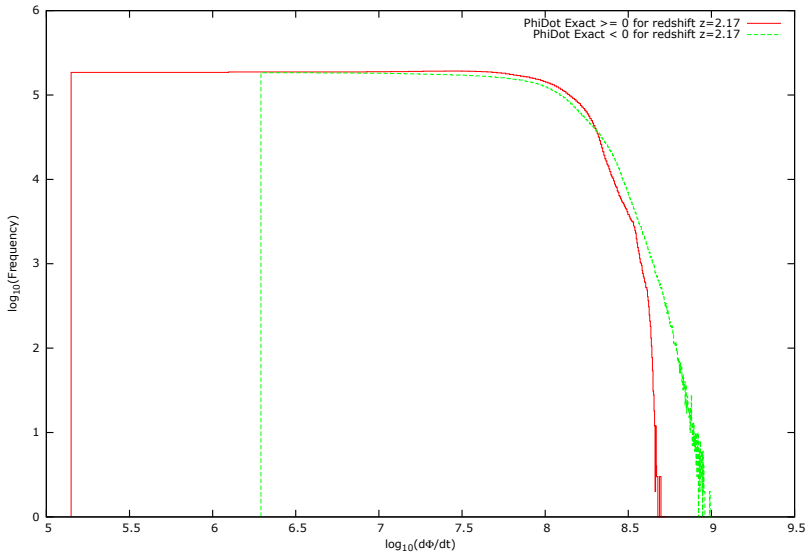

Figure 3.10: Histogram of the time derivative of the gravitational potential $\dot{\Phi}$ for redshift $z = 2.17$. The curves shown give a comparison between the distribution of the data obtained with the exact solution (Equation 3.2) for positive and negative values. The data shown are given in logarithmic-scale. For each regime, one of the curves gives the values of $\dot{\Phi} > 0$, while the other curve gives the absolute value of the data when $\dot{\Phi} < 0$. The statistical analysis of the histograms is shown in Table 3.4.

Statistical	Redshift $z = 2.17$	
property	Linear scale	Log_{10} scale
$\overline{\dot{\Phi}}$	0.0	9.031761
$\dot{\Phi}_{\text{median}}$	5.817817×10^{6}	9.0368
σ^2	1.392317×10^{16}	2.438×10^{-3}
σ	1.179964×10^{8}	0.0493776
b_1	0.62495	517.536793
g_2	-0.323848	-2.5411

Table 3.4: Statistical properties for the histograms of the time derivative of gravitational potential in Figure 3.10 for redshift $z = 0.0$. $\overline{\dot{\Phi}}$ is the mean, $\dot{\Phi}_{\text{median}}$ is the median, σ^2 is the variance, σ is the standard deviation, b_1 is the skewness and g_2 is the kurtosis.

the maps of the density contrast $\Delta(\mathbf{x})$ (Figure 2.8), with the maps of the gravitational potential (Figure 2.9). From those maps, it is possible to see that high values of the density contrast are related with lower and negative values of the gravitational potential, that means, with regions where $\Phi(\mathbf{x})$ has a well shape. Conversely, underdense regions are related with higher and positive values of $\Phi(\mathbf{x})$, where the potential has the shape of a "mountain".

When comparing the potential maps with its temporal gradient (Figure 2.10 and Figure 2.12), it is possible to see that the lowest values of $\Phi(\mathbf{x})$ are correlated with the highest values of $\dot{\Phi}(\mathbf{x})$, and vice versa. The higher values of $\dot{\Phi}(\mathbf{x})$ are related with a faster evolution in time of the gravitational potential. As we are comparing maps with redshift $z = 0.0$, this behavior is expected, because by the accelerated rate in the expansion of the universe at lower redshift, the gravitational potential should evolve quickly. Those regions where $\Phi(\mathbf{x}) < 0$, are deep potentials which will evolve in order to lose some depth and became more "flat". Regions where $\Phi(\mathbf{x}) > 0$, as they're more like a "mountain", with the expansion of the universe, will became less higher.

Now, we can make a connection between regions where the temporal gradient of the gravitational potential has positive values and those regions where the density contrast has higher values. On the other hand, the lower values of $\dot{\Phi}(\mathbf{x})$, as implies a slower evolution of the gravitational potential, are related with underdense regions.

The distribution of $\dot{\Phi}(\mathbf{x})$ for redshift $z = 0.0$ is shown in Figure 3.9, given in logarithmic scale. In order to avoid singularities in the logarithm, negative values are present in absolute value. The histogram shows a little asymmetry towards higher values of $\dot{\Phi}(\mathbf{x})$, while the negative values present an abrupt fall. Then, the relation between positive values of $\dot{\Phi}(\mathbf{x})$ and positive values of the density contrast $\Delta(\mathbf{x})$ becomes clearer. The asymmetry towards positive values of $\Delta(\mathbf{x})$ is related with the asymmetry towards positive values of $\dot{\Phi}(\mathbf{x})$ by the fact that overdense regions with deeper gravitational potentials will underwent this faster evolution of the potential well. As distribution of $\Delta(\mathbf{x})$ has a very abrupt fall for the lowest values, it implies the fall in the negative values of $\dot{\Phi}(\mathbf{x})$, which is associated with those regions with a potential that evolves slowly.

In the case of the distribution of $\dot{\Phi}(\mathbf{x})$ for redshift $z = 2.17$, the behavior is opposed to the discribed for $z = 0.0$. The fall in the distribution of $\dot{\Phi}(\mathbf{x})$ in the higher values is related with the fact that the distribution of the density contrast has no much high values, while the asymmetry towards negative values of $\dot{\Phi}(\mathbf{x})$ is related with the lower values of the density contrast, due to the uniform distribution of matter at higher redshifts,

as explained before. That means, for high redshift, the evolution of the gravitational potential wells is slower than for low redshifts.

From this analysis, we can conclude that for low redshifts, as the evolution in time of the gravitational potential wells is faster than for high redshift, the range of fluctuations of temperatures increases, due to this evolution, which is expected because in an underdense region, with a mountain-like potential a photon climbs it, and when it is going to descend, the potential well has evolved quickly and its height is very lower. The cooling of the photon (or the losing of energy) will be more notable than in the case that the potential well evolves with a slower rate. Similarly, if the photon is going to pass through a deep gravitational potential, when it descends, the photon will gain a large amount of energy, and then increasing its temperature, but if the potential has evolve quickly and is less deeper, the energy that the photon will lose will be smaller than the energy it has gained, and the net change in the temperature will be reflected in an increase. If the potential well evolves slowly, the net change in the energy will be lower and the increase in the temperature will not be too large. Those effects on the evolution of the gravitational potential wells are due to the fact of the accelerated expansion of the Universe at lower redshifts, which make them evolve in a faster way than at a higher redshift.

Finally, despite for $z = 0.0$ the distribution of $\dot{\Phi}(\mathbf{x})$ has an extended tail towards positive and higher values, the amount of values fullfilling $\dot{\Phi}(\mathbf{x}) < 0$ (related with underdense regions) is greater than the amount of values for which $\dot{\Phi}\mathbf{x} > 0$. Although the maximum values of $\dot{\Phi}(\mathbf{x}) > 0$ could be as large as four times the maximum value of $\dot{\Phi}(\mathbf{x}) < 0$ (in absolute value, i.e., actually it is the minimun value of the distribution), the great amount of regions with $\dot{\Phi}(\mathbf{x}) < 0$ compensates this behavior and the distribution of values of integral from Equation 3.1 present a large asymmetry towards the negative values of ΔT (as can be seen in Figure 3.9 and Table 3.3), related with cold regions in the Sachs-Wolfe maps. This idea can be understood as if there is a gravitational potential well with positive derivative, evolving quickly and becoming less deeper due to the expansion of the Universe with a very high value of $\dot{\Phi}(\mathbf{x})$, but as there are many more underdense regions with negative values of $\dot{\Phi}(\mathbf{x})$, which means that these "mountains" are decreasing in height, the great amount of underdense regions will compensate the big overdensity with deep potential and even they will surpass the value of the overdensity, leaving a net effect of the dominance of underdensities, related with such cold regions in the distribution of temperature fluctuations ΔT.

For $z = 2.17$, regions with $\dot{\Phi}(\mathbf{x}) > 0$ present the abrupt fall at early values than the underdense regions $\dot{\Phi}(\mathbf{x}) < 0$, but the regions with positive values of $\dot{\Phi}(\mathbf{x})$ are present in a greater amount than the negative values of $\dot{\Phi}(\mathbf{x})$. Then, for a similar reason as the previous case with $z = 0.0$, although an underdense region could have a very high value (in absolute value) of $\dot{\Phi}(\mathbf{x})$, there will be many overdense regions with positive values of $\dot{\Phi}(\mathbf{x})$ which will compensate the fluctuation distribution and finally will leave a net effect of a little domain of the overdense regions, which are those related with higher values in the temperature fluctuations. This is the behavior that can be seen in the histogram Figure 3.10 for $z = 2.17$.

3.3 Testing the Results

In order to test the accuracy of our results we performed three different test. The first one has been discussed along with the development of the work and refers to the linear regime, with which we can compare the exact results obtained from Equation 3.2. A second test is about the temperature perturbations along the integration axis, i.e., the z-axis, which are also compared with the linear regime. A final test is about numerical convergence of the numerical integration method.

3.3.1 Comparison with Linear Regime

As the Integrated Sachs-Wolfe effect is related with the growth of the structures, and then with the evolution of the gravitational potential wells, it is a good test to compare the exact results obtained from Equation 3.2 with those obtained from the linear approximation of the growth of structures shown in Equation 3.3. A first comparison can be made between the maps of $\dot{\Phi}(\mathbf{x})$ from Figure 2.10, which were obtained from the exact equation (Equation 3.2), and the maps of the Figure 2.12, obtained in the linear regime. From both figures one can see that the order of magnitude of both groups of maps is the same (10^8 km^{2}s^{-3}), but the maps of the linear regime have a slightly small range.

Furthermore, the shape and structure of both maps is very similar, being the range in the values of $\dot{\Phi}_l(\mathbf{x})$ of the linear approximation lower than in the exact solution, which is expected from a linear approximation when compared with a non-linear solution for the growth of structures. Then, we have a good correspondence between both groups of maps and our results looks to be reliable.

On the other hand, a comparison was performed between the interpolated function $\dot{\Phi}_{\text{interp}}(x_z)$ from the exact solution and the interpolated function from the values obtained with the linear regime $\dot{\Phi}_{\text{i,l}}(x_z)$. The comparison is shown in Figure 3.12.

Figure 3.12 shows the comparison between the interpolated functions $\dot{\Phi}_{\text{interp}}(x_z)$ obtained with the values from the exact solution and $\dot{\Phi}_{\text{i,l}}(x_z)$ obtained with the values of the linear regime. Both interpolated functions were performed for the grid of $N_g = 256$ and the figure shows both functions for three different vectors with IDs $n = 0, 365, 500$. The comparison of both interpolated functions for each cell shows that both functions $\dot{\Phi}_{\text{interp}}(x_z)$ and $\dot{\Phi}_{\text{i,l}}(x_z)$ have a very similar shape and share the same order of magnitude, allowing us to conclude that both regimes, the linear one and the exact solution, have only very small differences which will not disturb our results and will allow us to make a good comparison between the maps of the temperature fluctuations obtained with both regimes.

3.3.2 Temperature Perturbations along the z-axis

An analysis of the temperature perturbations along the integration axis (the z-axis) was performed, in order to compare our results with those obtained by [4]. To obtain such temperature perturbations, it is necessary to know the derivative of the temperature respect to the comoving position x_z along the z-axis. To compute $\mathrm{d}T/\mathrm{d}x_z$ we performed a numerical integration of the integral from Equation 3.2 from back to front in each of the cells along the z-axis. That means, we took a certain vector with ID n, given by Equation 3.4, which has fixed values of i and j, i.e., fixed values of comoving position x_x and x_y. Along the z-axis of this fixed vector, we began to integrate from the inner border of the last cell, with position $x_{z,in} = (400 - \text{Cell Size})h^{-1}$Mpc until the outer border of the cell with position $x_{z,out} = 400h^{-1}$Mpc. The expression for Cell Size is given by Equation 2.30, and in the particular case for $N_g = 256$, $x_{z,in}$ has the value $x_{z,in} = 398.4375h^{-1}$Mpc. Once the integration between both limits gives the value of $\Delta T_{n,1}$ for this cell, we divide this value of $\Delta T_{n,1}$ by the size of the cell given by Equation 2.30, and we finally obtain the value of $\mathrm{d}T_{n,1}/\mathrm{d}x_z$ for the last cell related with the vector with ID n. The next step is to take the integral from the inner border of the next to last cell, with position $x_{z,in} = (400 - 2\,\text{Cell Size})h^{-1}$Mpc until the outer border of the box, i.e., until $x_{z,out} = 400h^{-1}$Mpc, obtaining a value of $\Delta T_{n,2}$. Then, we substract the values $\Delta T_{n,2} - \Delta T_{n,1}$ to obtain the actual value of ΔT related to the penultimate cell. Finally, dividing this value of ΔT by the size of the cell, we obtain $\mathrm{d}T_{n,2}/\mathrm{d}x_z$. This process is performed along all the z-axis, finishing with the estimation of $\mathrm{d}T/\mathrm{d}x_z$ related to the vector with ID n.

Those integrals were performed with 10000 integration steps. The analysis and comparison with the results obtained with 1000 integration steps will be seen in subsection 3.3.3.

In Figure 3.13 we can see a comparison between the temperature fluctuations $\mathrm{d}T/\mathrm{d}x_z$ along the z-axis analogous to the comparison shown in Figure 3.1, where we can see that even for different resolutions, the curves hold their shapes and its order of magnitude.

On the other hand, a comparison between the temperature fluctuations obtained with the values from the exact solution to $\dot{\Phi}(\mathbf{x})$ and those from the linear regime is shown in Figure 3.14. In this figure we can see, again, that both the shape and the order of magnitude of the curves representing the temperature perturbations for both kind of solutions are very similar, and the methods used until now and the corresponding results still look reliable. The curves of Figure 3.14 were calculated for the grid of $N_g = 256$ cells per axis.

As said before, the idea to calculate the temperature perturbations along the integration axis is to compare our results with those of [4] to see if our methods allow us to obtain reliable results and to be able to compare them with other works, due to the big differences in the detectability of the Sachs-Wolfe effect between different authors, as presented by [3] and [10].

When comparing our results of $\mathrm{d}T/\mathrm{d}x_z$ with those of [4], we found that the range of temperatures are slightly lower than [4], but the order of magnitude is similar. Conversely, the Sachs-Wolfe maps are a factor of 10^2 times lower in temperature. This behavior can be explained because the simulation box used in our work has only $400h^{-1}$Mpc in each axis, and this defines our integration range, while the simulation box used by authors like [4] is bigger compared with ours, being of $1h^{-1}$Gpc and it is periodically repeated in order to create a mock catalogue of even more than $6h^{-1}$Gpc. Then, the accumulated values of the integral from Equation 3.2 are 10^2 times greater than our results.

3.3.3 Numerical Convergence

A final test related to numerical convergence was made, in order to verify if the numerical methods were well implemented and determine whether the results are consistent and converge to a well-behaved function. To test this hypothesis, we performed the numerical integrations with the Simpson method with two differente integration steps: the first was made with 1000 integration steps, while the second one was performed with 10000 steps. Those different integration steps were implemented in the integration to obtain the temperature perturbations along the z-axis, i.e., $\mathrm{d}T/\mathrm{d}x_z$, and the whole integration to obtain

the the temperature fluctuation respect to the mean temperature of the CMB, i.e., ΔT in order to determine the Sachs-Wolfe maps shown in section 3.2.

First, we are going to analyze the behavior for the temperature perturbations along the z-axis, for both, the values from the exact solution of Equation 3.2, and for those from the linear approximation in Equation 3.3. In Figure 3.15, we can see the comparison between the functions obtained with both integrations steps, for the exact solution values and for linear approximation. The first plot at the top shown in Figure 3.15 is the same depicted in Figure 3.14, and correspond to the comparison between the temperature perturbations $\mathrm{d}T/\mathrm{d}x_z$ obtained with the exact values and those obtained in the linear approximation with 10000 integration steps. The second plot, at the bottom, correspond to the same comparison but made with 1000 integration steps. We do see a good behavior in both plots, with a very similar shape and sharing the same order of magnitude, from which we can conclude that the functions obtained from the interpolation, $\dot{\Phi}_{\text{interp}}(x_z)$ and $\dot{\Phi}_{\text{i,l}}(x_z)$ are well-behaved and its integration converges to a well-behaved function.

The comparison between the results obtained with the two different integration steps is depicted in Figure 3.16, separately for the exact solution values and for the linear regime. The figure at the top correspond to the comparison of the temperature perturbations with both integration steps for the exact solution, while the bottom picture correspond to the comparison in the linear regime. Here we can see again that the overall structure of the curves is maintained in both pictures.

Furthermore, Figure 3.17 and Figure 3.18 depict how even for the different grids, the temperature perturbations maintain its structure and order of magnitude if the integration is performed with 1000 or with 10000 integration steps, for the exact values or for the linear regime, respectively. The plot at the top of Figure 3.17 shows the comparison of the temperature fluctuation for the grids performed with 10000 integration steps with the exact values, while the bottom plot is for the integration performed with 1000 integration steps. It is analogous for the top and bottom figures of Figure 3.18, but in the linear regime.

Finally, a comparison between the Sachs-Wolfe maps with the two different integration steps are shown in Figure 3.19 and Figure 3.20 for both regimes: the exact solution and the linear regime, respectively. We continue seeing a good numerical convergence, because in both regimes the overal structure of the Sachs-Wolfe maps looks to be the same, and the differences between both integration steps are very slight.

From those results, it is possible to see that effectively, we have obtained a late ISW contribution. It is remarkable to say that it is a late effect because our integration range

comprehend only $400h^{-1}$Mpc, while in works as in [4], they have used an integration range of $6h^{-1}$Gpc. Then, the range of redshifts used in this works is very near to $z = 0.0$, while [4] has a wider range in redshift. Then, although it is possible to see in the plots of $\mathrm{d}T/\mathrm{d}x_z$ (Figure 3.13) that the range of temperatures is very similar to the obtained in [4], our late ISW maps have a range of temperatures a factor 10^2 times lower, due to the small range of integration used by us. We can see that our results are consistent with the work of [4], and it is due to the small range of integration that our results show a lower temperature ranges. It is expected that, in the future step, when the mock catalogue will be constructed, that our results show much more consistency with the works of the other authors.

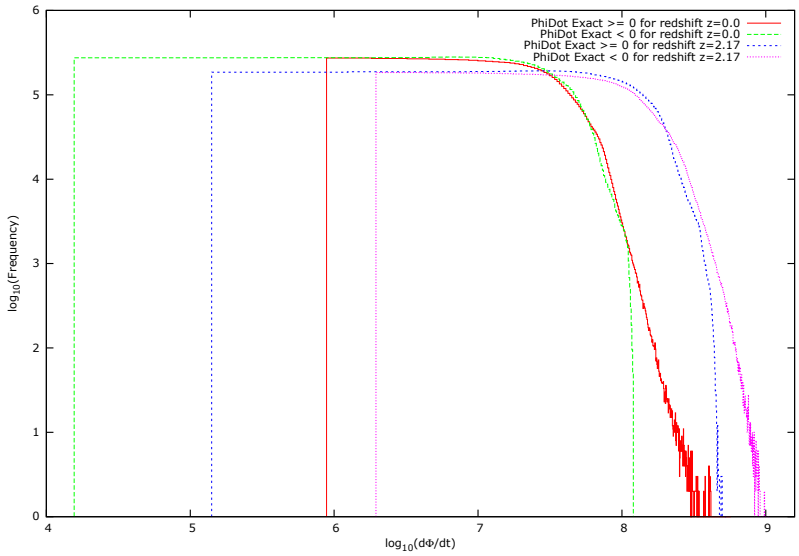

Figure 3.11: Histogram of the time derivative of the gravitational potential $\dot{\Phi}$. The figure shows four curves, tow for the snapshot with redshift $z = 0.0$ and two for the snapshot with redshift $z = 2.17$. For each snapshot, one of the curves gives the values of $\dot{\Phi} > 0$, while the other curve gives the absolute value of the data when $\dot{\Phi} < 0$. The data used in these histograms are from the exact regime, given by Equation 3.2.

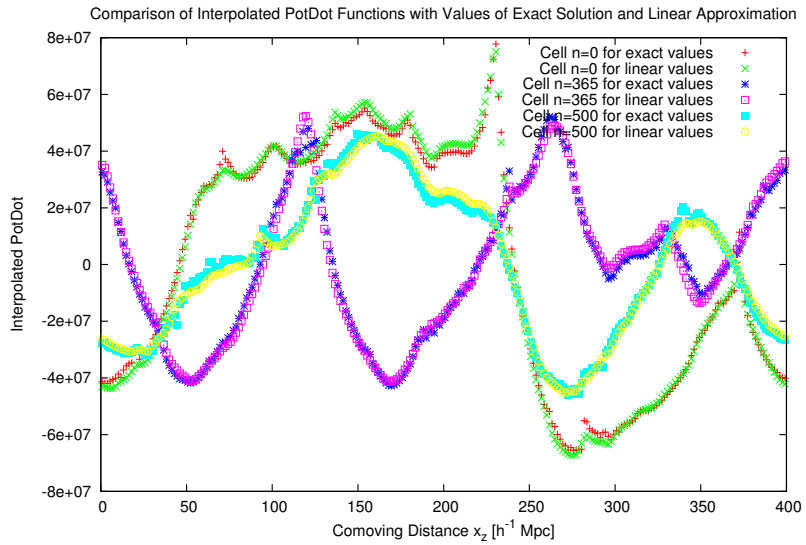

Figure 3.12: Comparison of the interpolated functions $\dot{\Phi}_{\text{interp}}(x_z)$ and $\dot{\Phi}_{\text{i,l}}(x_z)$, obtained from the values of the exact solution and the values from the linear regime, respectively. Both interpolated functions were performed for the grid of $N_g = 256$. This figure shows the comparison of both interpolated functions for the vectors with ID $n = 0, 365, 500$. We can see that for each vector, both functions have a similar shape and the order of magnitude range is almost the same, then having a similar behavior.

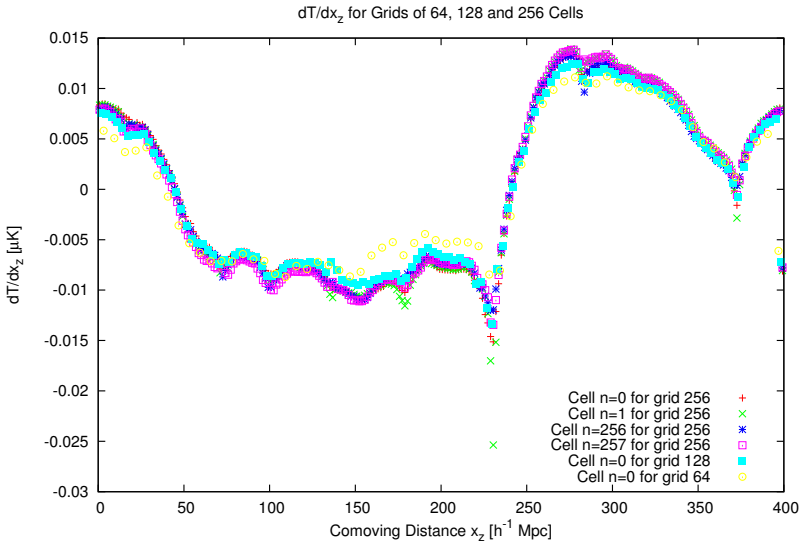

Figure 3.13: Temperature perturbations $\mathrm{d}T/\mathrm{d}x_z$ (in units of $h\mu$ KMpc^{-1}) along the z-axis. This figure shows six different curves, four of each correspond to the temperature fluctuations for the vectors with ID $n_{256} = 0, 1, 256, 257$ of the grid $N_g = 256$, while the aquamarine-squared curve correspond to the temperature fluctuations for the vector $n_{128} = 0$ of the grid $N_g = 128$ and the yellow-circled curve for the vector $n_{64} = 0$ of the grid $N_g = 64$. The integration were performed with 10000 integration steps to find the temperature perturbation for each cell. These curves show that both, the order of magnitude and the shape of the curves do not depend on the resolution, and only underwent slightly fluctuations.

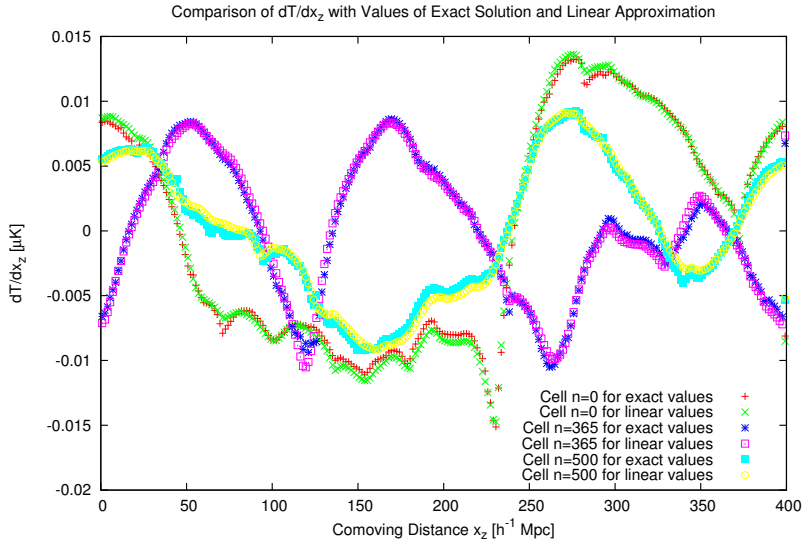

Figure 3.14: Comparison of the temperature perturbations for the values from the exact solution and those from the linear approximation. Those temperature fluctuations were calculated for the grid of $N_g = 256$. This figure shows the comparison of the temperature fluctuations for the vectors with ID $n = 0, 365, 500$. We can see that for each cell, both curves, that from the exact solutions and that from the linear regime, have a similar shape order of magnitude, having both regimes a similar behavior.

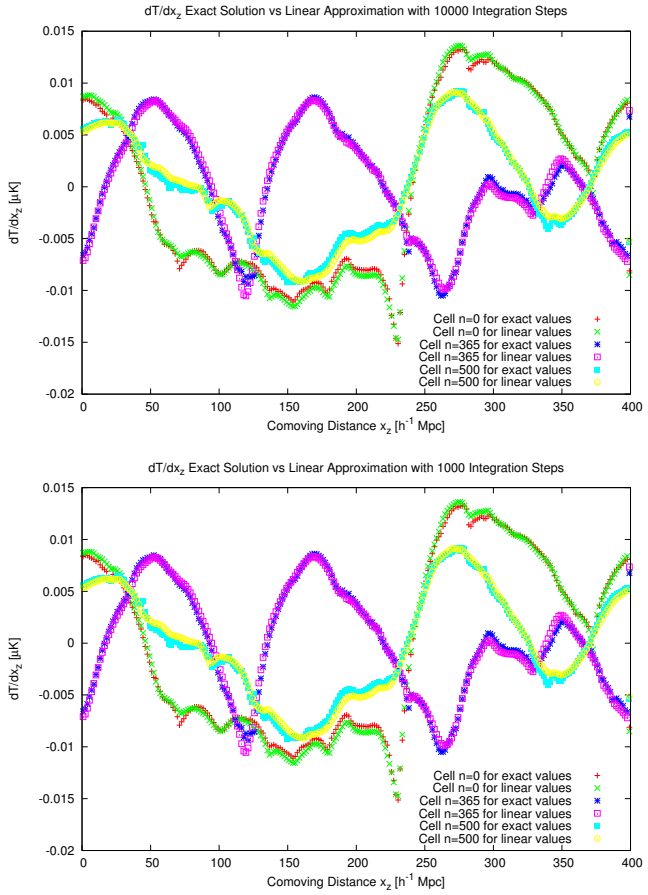

Figure 3.15: Temperature perturbations along the integration axis, the z-axis, obtained with the two integration steps used to test the numerical convergence. The first picture in the top shows the temperature perturbations obtained with 10000 integration steps, and it is the same figure depicted in Figure 3.14. The second picture in the bottom shows the temperature perturbation for the 1000 integration steps. Both figures share a similar shape and order of magnitude, meaning that our interpolated functions $\dot{\Phi}_{\text{interp}}(x_z)$ and $\dot{\Phi}_{\text{i,l}}(x_z)$ are well-behaved.

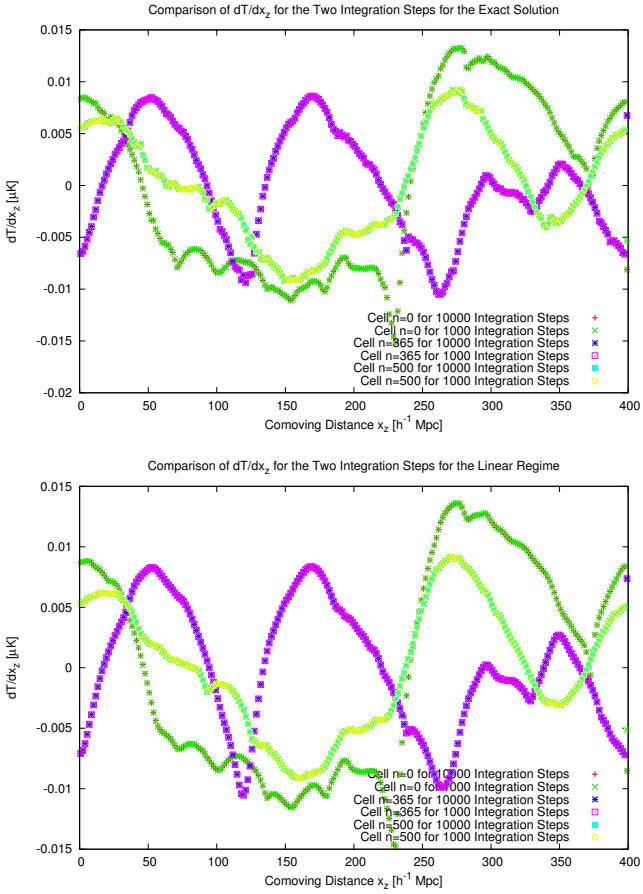

Figure 3.16: Temperature perturbations along the integration axis, the z-axis, obtained with the two integration steps used to test the numerical convergence. The first picture in the top shows the comparison of the temperature perturbations obtained with the integration steps used in the case of the exact solution. The second picture in the bottom shows the same comparison but in the case of the linear regime values.

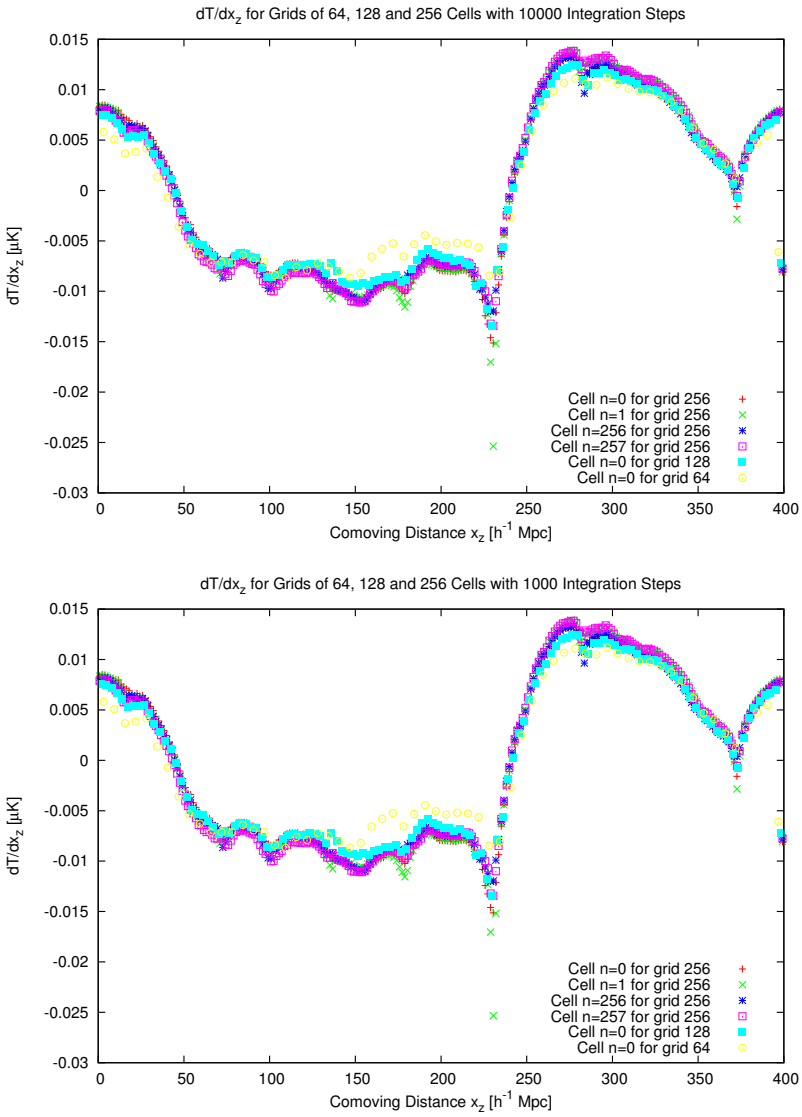

Figure 3.17: Temperature perturbations along the integration axis, the z-axis, obtained with the two integration steps used to test the numerical convergence. The first picture in the top shows the comparison in the grids of the temperature perturbations obtained with 10000 integration steps used in the case of the exact solution. The second picture in the bottom shows the same comparison but with 1000 integration steps. In both figures the order of magnitude and the overall structure of the curves maintain, showing us a good numerical convergence.

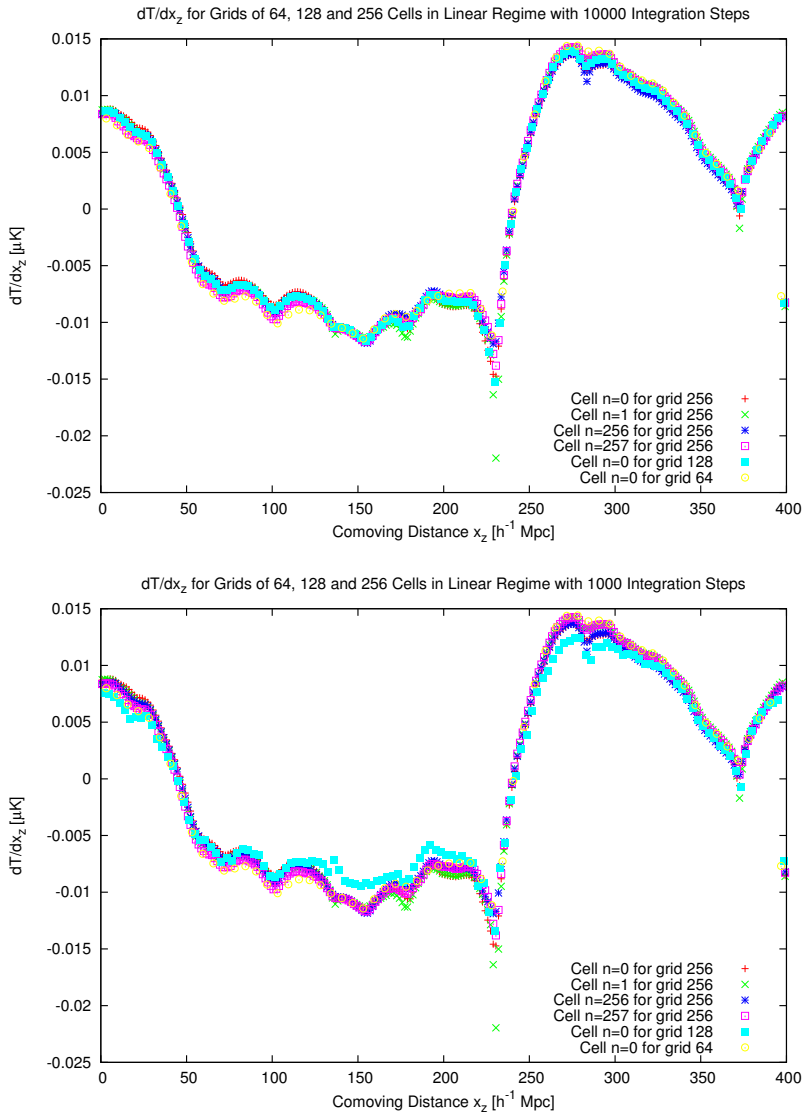

Figure 3.18: Temperature perturbations along the integration axis, the z-axis, obtained with the two integration steps used to test the numerical convergence. The first picture in the top shows the comparison in the grids of the temperature perturbations obtained with 10000 integration steps used in the linear regime. The second picture in the bottom shows the same comparison but with 1000 integration steps. In both figures the order of magnitude and the overall structure of the curves maintain, showing us a good numerical convergence and consistent results when compared with the temperature fluctuations obtained with the exact solution shown in Figure 3.17.

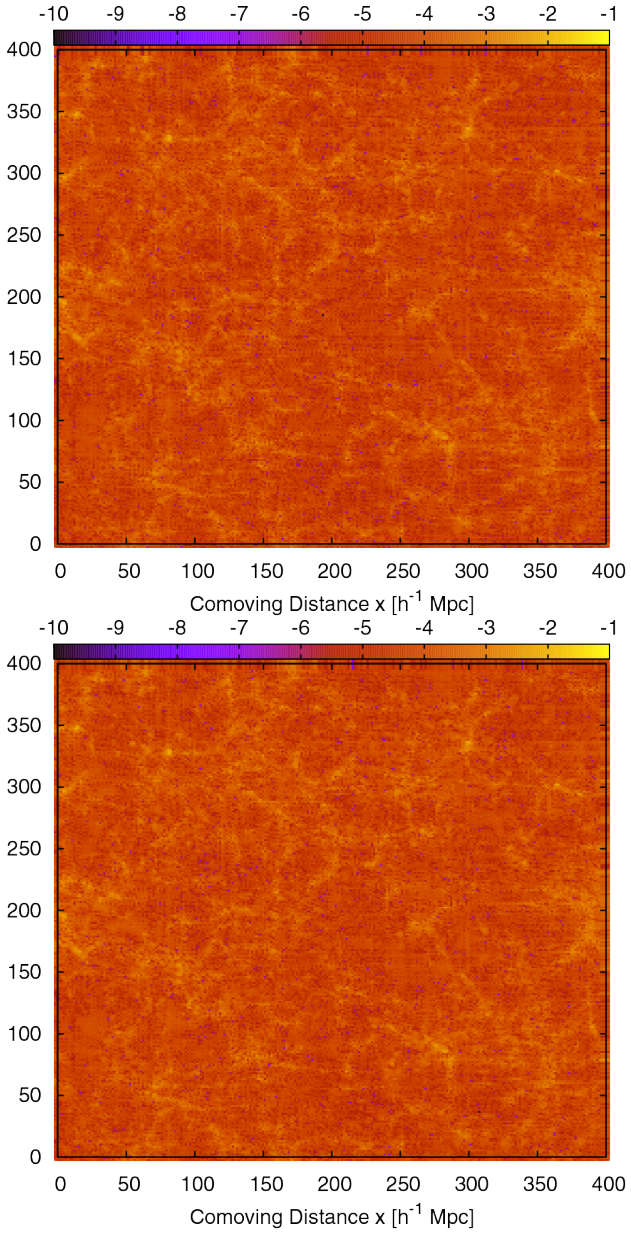

Figure 3.19: Sachs-Wolfe anisotropy maps in the regime of the exact solution. The top figure shows the map obtained with 10000 integration steps with the Simpson method, while the bottom figure depicts the map obtained with 1000 integration steps. Both maps share the same range of temperatures and the overal structure is very similar, allowing us to conclude that our numerical methods were well implemented, in agreement with a good numerical convergence. The map is in logarithmic scale, i.e., it is show $\log_{10}(\Delta T)$, with T in [μ K].

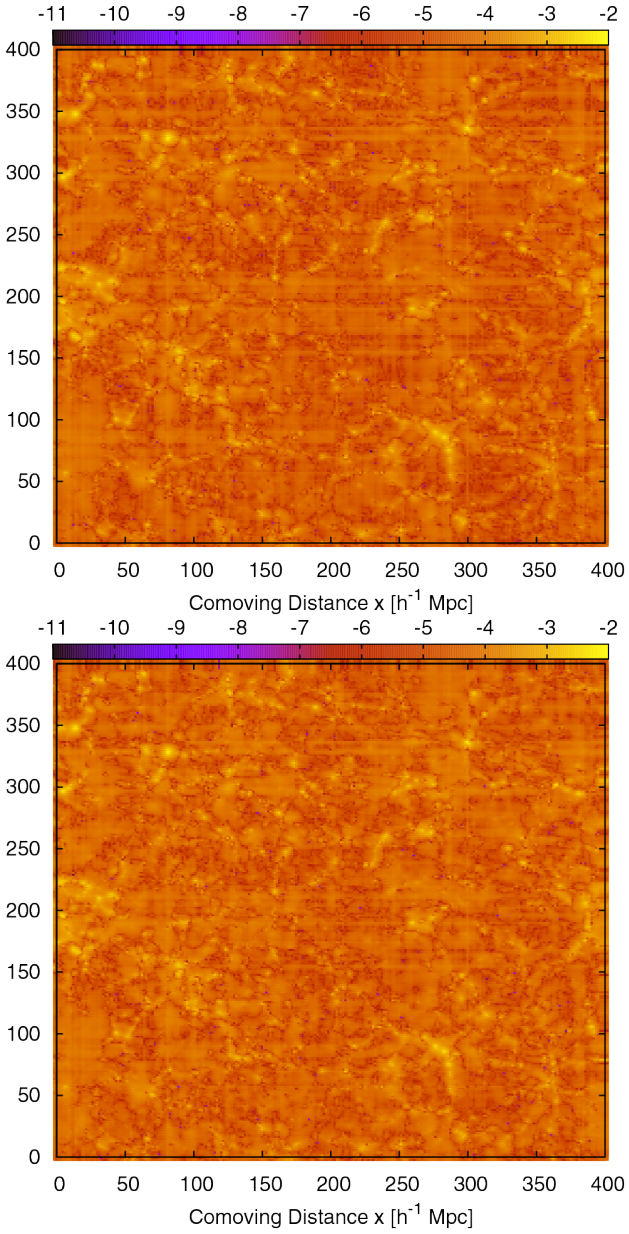

Figure 3.20: Sachs-Wolfe anisotropy maps in the regime of the linear approximation. The top figure shows the map obtained with 10000 integration steps with the Simpson method, while the bottom figure depicts the map obtained with 1000 integration steps. Both maps share the same range of temperatures and the overal structure is very similar, allowing us to conclude that our numerical methods were well implemented, in agreement with a good numerical convergence. Even when compared with the exact maps from Figure 3.19, the structure of both regime maps is very similar, although the range of temperatures is slightly lower in the linear case. The map is in logarithmic scale, i.e., it is show $\log_{10}(\Delta T)$, with T in [μ K].

"The fact that the colors in the flower evolved in order to attract insects to pollinate it is interesting; it means that insects can see the color. It adds a question: does this aesthetic sense also exist in the lower forms? [...] All kinds of interesting questions which the science knowledge only adds to the excitement, the mystery and the awe of a flower."

Richard P. Feynman (about beauty)

CHAPTER

4

Conclusions

This chapter is dedicated to discuss and compile the results obtained throghout this work. This final analysis is discussed in the order in which the results where obtained, beginning with the maps of density fluctuations, gravitational potential and its time derivative. Later, the Sachs-Wolfe maps will be discussed and finally the histograms of the distribution of temperature fluctuations, density contrast and time derivative of the gravitational potential.

4.1 Construction of Maps

As discussed in chapter 2, the maps of density contrast were obtained after an analysis of the positions of the particles in a cosmological simulation through the Nearest Grid-Point (NGP) scheme, in which a cubic grid with the same amount of cells per axis was used to study the distribution of particles in a cubic box with $400h^{-1}$ Mpc of side in order to obtain the density enclosed in each cell. From the three resolutions used ($N_g = 64, 128, 256$), the highest resolution was used to compute all the other physical quantities. Once the density of each cell was found, it is compared to the mean matter density of the simulation $\overline{\rho}$ in order to obtain the density contrast Δ and then, construct the corresponding maps of the distribution of matter in the simulation. This last quantity allow us to find both, the gravitational potential Φ and its time derivative $\dot{\Phi}$. The gravitational potential is computed through the Poisson's equation (Equation 2.38) and with the help of a Fourier method

this equation is transformed from the position-space to the Fourier space, giving the expression of Equation 2.39. Using the FFTW library to perform a Fast Fourier Transform (FFT), this equation is solved numerically and transformed again to the position-space, obtaining the corresponding values of the gravitational potential in the position-space. The confirmation of the gravitational potential is not really necessary to know the value of its time derivative $\dot{\Phi}$, but it has been calculated in this work in order to compare and verify the behavior of $\dot{\Phi}$ respect to Φ. Finally, with the help of Equation 2.49, and being careful with the sign convention used to perform the Fourier Transforms, it is possible to obtain the numerical values of $\dot{\Phi}$ in the position-space and construct the corresponding maps.

Figure 2.9 and Figure 2.10 shows a good correspondence between the structure of Φ and $\dot{\Phi}$, and when comparing those results with Figure 2.8 the correspondence between regions with high density and lowest values of gravitational potential or underdense (and some void) regions with high values of the potential is more evident. Finally, a linear approximation to the growth of structures was used in order to compute an approximation to the time derivative of the potential well, namely, $\dot{\Phi}_l$ (Equation 2.56) to compare the results obtained for $\dot{\Phi}$. When constructing the maps of $\dot{\Phi}_l$ (Figure 2.12), the correspondence continues to look very well in the case of the analyzed snapshot with redshift $z = 0.0$. Even, when comparing the distribution of the data of $\dot{\Phi}$ and $\dot{\Phi}_l$ in the histogram of Figure 3.9, both distributions have a very similar shape and approximated statistical moments. The comparison of $\dot{\Phi}$ and $\dot{\Phi}_l$ for redshift $z = 0.0$ gives good results and allows to think in a good implementation of the methods used until this point.

A brief analysis about the behavior of the density contrast $\Delta(\mathbf{x})$, the gravitational potential $\Phi(\mathbf{x})$ and the time derivative of the gravitational potential $\dot{\Phi}(\mathbf{x})$ allowed to understand the relations between those three physical quantities. From the maps of gravitational potential it is easy to relate lower values of the potential with higher values of the density contrast and vice versa. In the case of $\dot{\Phi}(\mathbf{x})$, it is easy to see how for lower and negative values of $\Phi(\mathbf{x})$, the time derivative $\dot{\Phi}(\mathbf{x})$ takes higher and positive values, allowing us to conclude that, based on the accelerated expansion of the Universe at lower redshifts, the potential wells evolve quickly, passing from a deeper well to a less deeper well in the case of the overdense regions, and passing from a "high mountain" to a less higher "mountain" in the case of the underdense regions. This allows to relate the regions with high and positive values of $\dot{\Phi}(\mathbf{x})$ with the overdense regions, and the lowest and negative values or $\dot{\Phi}(\mathbf{x})$ with underdense regions.

4.2 Estimation of the Late Integrated Sachs-Wolfe Effect

Once the time derivative of the gravitational potential was computed, an integration axis was chosen (in particular, the z-axis) in order to perform an interpolation of the function $\dot{\Phi}(\mathbf{x})$ in terms of the comoving position x_z along the z-axis, i.e., in order to obtain the function $\dot{\Phi}_{\text{interp}}(x_z)$. This interpolation was performed also in the linear regime, giving as result the function $\dot{\Phi}_{\text{i,l}}(x_z)$. Both interpolated functions were integrated with a Simpson method, with the late Integrated Sachs-Wolfe maps as outcome in both regimes. It should be mentioned that the Sachs-Wolfe maps were obtained for two different redshifts, $z = 0.0$ and $z = 2.17$ in order to compare the evolution of the Sachs-Wolfe maps and the distribution of the temperature fluctuations ΔT for the same system at two different times. The Sachs-Wolfe maps and the histograms of the distribution of temperature fluctuations can be seen in section 3.2.

From the analysis of the histograms of the temperature fluctuations ΔT is it possible to prove how with the expansion of the Universe, which implies a faster evolution of the gravitational potentials, the temperature's range for the distribution at redshift $z = 0.0$ is wider than the range of temperatures for the distribution at $z = 2.17$. It was also possible to relate the asymmetries in the distribution of the values of the density contrast and the time derivative of the gravitational potential with the asymmetries in the distribution of the temperature fluctuations. In the case of the lowest redshift, $z = 0.0$, although the distribution of $\dot{\Phi}$ showed an extended tail towards high and positive values (related with overdense regions) and the negative values (related with underdense regions) have an abrupt fall at an early value (in absolute value), the amount of underdense regions is higher than the amount of overdense regions. For this reason, the integration over underdense regions compensate the integration over the higher values of the overdense regions, and even surpass them, giving as net effect a little great contribution of the underdense regions over the overdense ones. This contribution of the underdense regions gives as result, an asymmetry in the distribution of the temperature fluctuations towards the negative values of ΔT, in other words, to the colder regions of the Sachs-Wolfe maps.

Conversely, in the case of the redshift $z = 2.17$, the distribution in the values of $\dot{\Phi}$ has an opposed behavior than for $z = 0.0$, i.e., although the distribution has an extended tail towards the negative and lower values of $\dot{\Phi}$ (underdense regions), the amount of overdense regions is large, and when the integration is performed, the net effect is a little large contribution of those overdense regions over the underdense regions. This contribution of the overdense regions, gives as result an asymmetry in the distribution of ΔT towards the positive values, which is related with the hotter regions in the maps of

Sachs-Wolfe.

After the construction of the Sachs-Wolfe maps, some tests were performed in order to conclude if the implemented methods go in a correct way. The first test was a comparison of the exact values of $\dot{\Phi}$, given by Equation 2.49 and the values from the linear regime, given by Equation 2.56. The comparison between the interpolated functions of $\dot{\Phi}$ in both regimes showed a good convergence, maintaining a similar shape and order of magnitude. A second test related with the temperature fluctuations along the integration axis (z-axis), was performed, in which it was compared the temperature fluctuations $\mathrm{d}T/\mathrm{d}x_z$ in both regimes. Again, the shape and order of magnitude in both regimes showed a good correspondence, and even for different resolutions, the shape and order of magnitude showed a good convergence. Although the temperature fluctuations were computed in order to compare with the results of [4] and the order of magnitude is similar to that obtained by them, we cannot see an damping in the behavior of $\mathrm{d}T/\mathrm{d}x_z$, because the integration range used by us is very small compared with the used by [4]. We expect that in a future, as will be seen in section 4.3, with the construction of a mock catalogue we could obtain results that we can compare more efficiently. Despite this, we have obtained the late ISW maps for our simulation, which by the small integration range compared with the work of [4], we have a small range in temperature fluctuations of the late ISW map, although they are consistent results.

The final test was related with the numerical convergence of the integration method. In this test, two different values for the number of integration steps were used: a first integration was performed with 1000 integration steps, and the second one with 10000 integration steps. For both values of the integration steps, both the Sachs-Wolfe maps and the temperature fluctuation along the z-axis ($\mathrm{d}T/\mathrm{d}x_z$) showed a very good numerical convergence, in which the shape, structure and order of magnitude of those physical quantities was maintained in the two regimes we used. With those three test, we can conclude that the numerical methods used in this work were well implemented and showed coherent results, which are expected if we based our assumptions in the described theoretical framework.

Finally, it is very worthy to stand out that the effect studied in this work it is not really the Integrated Sachs-Wolfe, because as mentioned in the theoretical framework in subsection 1.5.5, this Integrated Sachs-Wolfe effect is observed through the visual line that joins the the surface of last scattering with the position of the observer in the Earth. That means, the path that the photons travel is a very long way, much greater than the

$400h^{-1}$Mpc that compose our integration dominion. Despite this reason, this work gives a very good preliminars in the study of the Sachs-Wolfe effect, which will be used to compare the results from the integration through a mock catalogue constructed with the boxes of the simulation used, and the values obtained when the same proccess is applied to observational data.

4.3 Outlook

Along the work it was mentioned that it has been studied a late Integrated Sachs-Wolfe effect, due to the long time and lack of computational resourses to make the study more extensive and detailed. The outlook is to make use of the methods shown here in order to calculate a complete Integrated Sachs-Wolfe effect through a mock catalogue constructed with the simulation boxes at different redshifts one after another. After those results with the mock catalogue, the aim is to perform the same processing to a real catalogue of galaxies taken from one of the data releases of the Sloan Digital Sky Survey and determine the detectability of the Integrated Sachs-Wolfe effect with real data and determine if this can be used as evidence of the dark energy which is the cause of the accelerated rate of expansion of the Universe.

Bibliography

[1] George B. Arfken and Hans J. Weber. *Mathematical Methods for Physicists*. Elsevier Academic, USA, sixth edition, 2005. ISBN 0-12-059876-0. 49

[2] Teached by: Juan Carlos Muñoz-Cuartas. *Galaxies and Cosmology course notes*. University of Antioquia, Semester 2013-2. 2, 4, 6, 17, 19

[3] A. Cabré et al. Cross-correlation of wmap 3rd year data and the sdss dr4 galaxy survey: new evidence for dark energy. *Monthly Notices of the Royal Astronomical Society*, 372:5, 2006. 104

[4] Yan-Chuan Cai, S. Cole, et al. Full-sky map of the isw and rees-sciama effect from gpc simulations. *Monthly Notices of the Royal Astronomical Society*, 407:201–224, 2010. 31, 32, 60, 82, 103, 104, 106, 120

[5] Bradley W. Carrol and Ostlie Dale A. *An Introduction to Modern Astrophysics*. Pearson International, San Francisco, second edition, 2007. ISBN 0-321-44284-9. 2, 3, 6, 12, 16, 17, 18, 30

[6] K. Dolag et al. Simulation techniques for cosmological simulations. *Space Science Review*, 134:229–268, 2008. 37, 45

[7] Jordi-Lluis Figueras. *A short tutorial on the basic usage of the package FFTW3*. 2010. 57

[8] Matteo Friggo and Steven G. Johnson. *FFTW for version 3.3.3 manual*. 2012. 57, 58, 70

[9] E. Gawiser and J. Slik. The cosmic microwave background radiation. *Physics Reports*, 333:245–267, 2000. 27

[10] B. R. Granett, M. C. Nyrinck, and I. Szapudi. An imprint of super-structures on the microwave background du the tue integrated sachs-wolfe effect. *Astrophysical Journal*, 683:L99–L102, 2008. 104

[11] Peter Hoyng. *Relativistic Astrophysics and Cosmology*. Springer, New York, first edition, 2006. ISBN 978-1-4020-4521-9. ix, 36

[12] A. Klypin. Numerical simulation in cosmology i: Methods. *Annalen der Physik*, 2000. 37

[13] A.A. Klypin, S. Trujillo-Gomez, and J. Primack. Dark matter halos in the standard cosmological model: Results from the bolshoi simulation. *Astrophysical Journal*, 740:102, 2011. 24

[14] Malcolm S. Longair. *Galaxy Formation*. Springer, New York, second edition, 2008. ISBN 978-3-540-73477-2. 24

[15] Vincent J. Martínez and Enn Saar. *Statistics of the Galaxy Distribution*. CHAPMAN & HALL/CRC, USA, first edition, 2002. ISBN 1-58488-084-8. 23

[16] J. C. Muñoz-Cuartas and V. Müller. Galaxy groups and haloes in the seventh data release of the sloan digital sky survey. *Monthly Notices of the Royal Astronomical Society*, 423:1583–1595, 2012. 21

[17] Juan C. Muñoz Cuartas. *Master Thesis: Studying Star Formation in Evolving Galaxies through Simulations of Formation of Large Scale Structure in the Universe*. University of Antioquia, 2008. 20, 21

[18] M. Plionis. The quest for the cosmological parameters. *Lecture Notes in Physics*, 592:147–207, 2002. 18

[19] William H. Press, Saul A. Teukolsky, et al. *Numerical Recipies in C. The Art of Scientific Computing*. Cambridge University, New York, second edition, 1992. ISBN 0-521-43108-5. 47, 48, 49, 54

[20] N. Puchades, M. J. Fullana, et al. On the rees-sciama effect: maps and statistics. *Monthly Notices of the Royal Astronomical Society*, 370:1849–1858, 2006. 60

[21] R. K. Sachs and A. M. Wolfe. Perturbations of a cosmological model and angular variations of the microwave background. *Astrophysical Journal*, 147:73, 1967. 31

[22] Alonso Sepulveda. *Física Matemática*. Universidad de Antioquia, Colombia, 21th edition, 2009. ISBN 978-958-714-307-2. 49

[23] R. E. Smith, C. Hérnandez-Monteagudo, and U. Seljak. Impact of scale dependent bias and nonlinear structure growth on the integrated sachs-wolfe effect: Angular power spectra. *Physical Review D*, 80, 2009. 79